

**Ultralow refractive index metamaterials and band  
gap structures at optical wavelengths**

by

**Brian T Schwartz**

B.A., Swarthmore College, 1997

M.S., University of Colorado, Boulder, 2001

A thesis submitted to the  
Faculty of the Graduate School of the  
University of Colorado in partial fulfillment  
of the requirements for the degree of  
Doctor of Philosophy  
Department of Electrical and Computer Engineering  
2005

This thesis entitled:  
Ultralow refractive index metamaterials and band gap structures at optical  
wavelengths  
written by Brian T Schwartz  
has been approved for the Department of Electrical and Computer Engineering

---

Rafael Piestun

---

Prof. Wounjhang Park

Date \_\_\_\_\_

The final copy of this thesis has been examined by the signatories, and we find that both the content and the form meet acceptable presentation standards of scholarly work in the above mentioned discipline.

Schwartz, Brian T (Ph.D., Electrical Engineering)

Ultralow refractive index metamaterials and band gap structures at optical wavelengths

Thesis directed by Prof. Rafael Piestun

The ratio of the component refractive indices or dielectric constants is critical to the performance of many photonic structures composed of two or more dielectrics. This work concerns two methods of increasing this index contrast to either enhance or qualitatively change the performance of conventional optical components and nanostructures by employing metallic features in photonic crystals. Metal-dielectric metamaterials and photonic band gap structures are types of photonic crystals with potential applications in integrated photonics and new lighting technologies.

The first method involves photonic crystals consisting of two-dimensional wire arrays engineered such that the real part of their effective refractive index is less than one at visible wavelengths. These photonic crystals act as ultralow index metamaterials (ULIMs) at wavelengths just slightly longer than twice the unit cell length. Their reflection, refraction, and transmission properties mimic those of their equivalent homogeneous optical components, that is, those with the same refractive index and macroscopic shape. Examples include refraction, reflection, and transmission at a planar interface, a slab waveguide, and a lens.

Recent studies have assigned ultralow and negative effective refractive index values to dielectric photonic crystals based on their dispersion curves. Here I show that this definition is insufficient to properly define an effective index. Because these photonic crystals support strongly modulated Bloch modes, their reflection and transmission properties differ from those of their equivalent homogeneous slab.

The second application of metals in photonic crystals presented here is the deposition of thin metal coatings on artificial opal structures to create photonic band gap

materials. Precise control of coating thickness is critical for optimum band gap properties. Our recent experiments show that to the extent that these coatings are thin compared to the sphere radius, the deposition rate is similar to that on a planar substrate. Here I specify the valid range of this approximation and validate the accuracy of laboratory methods of controlling coating thickness.

Tungsten's high melting point, dielectric constant values, and established use in atomic layer deposition suggests its suitability in efficient band-gap based lighting applications. I use numerical simulations to validate experimental reflectance spectra showing band gap effects in tungsten-coated silica opals.

## Acknowledgements

This dissertation would not have been possible without the contributions of several individuals. By participating in the Optical Science and Engineering Program (OSEP), directed by Prof. Dana Z. Anderson, I discovered my preferred research style and work environment. As I was completing my Master's Degree, Prof. Garret Moddel sparked my interest in the field, and shortly after I found Andrew Reynolds's photonic crystal software. It has been an indispensable part of my research, as has Mr. Reynolds's enthusiastic support over the years. Sébastien Rondineau, Michael Buck, Matt Lessem, Michael Varney, and the technical support team at COMSOL, Inc. have also provided valuable computer-related assistance. Adam Sadoff and Billy Woods of the Electrical Engineering Staff have been of great support. I have valued my work with the Nanoscale Interdisciplinary Research Team (NIRT), and especially Zachary Sechrist, for providing the experimental component and perspective of my research.

Several professors have consistently welcomed my questions, at any hour of day or night. They include Dejan Filipovic, Alan Mickelson, Wounjhang Park, Kelvin Wagner, and of course, Rafael Piestun, my advisor. Prof. Piestun gave me the freedom to pursue my interests while keeping me focused on results, seeing solutions, opportunities, and progress where I saw problems, suggesting what I might be overlooking, and for being patient while I overcame one obstacle after another that I thought I would never resolve.

Fellow graduate students Ben Braker, Friso Schlottau, and Marie Tripp have been supportive coworkers and friends. I would also like to acknowledge the CU Campus Libertarians and the Boulder Staff Council Softball committee for complementing the academic aspect of my graduate school experience. Lastly, am grateful to parents for always being there for me and supporting my choices.

Two National Science Foundation grants were major funding sources. An Interdisciplinary Graduate Research Training (IGERT) grant 9870665 (through OSEP) funded my Masters Degree and foundational parts of this work. Grant 0304650 for the NSF NIRT project funded my work with opal photonic crystals. Other sources include Prof. Piestun's startup funds, his Council on Research and Creative Work (CRCW, U. Colorado) award, an International Society of Optical Engineering (SPIE) scholarship, and a Beverly Sears Graduate Student Grant from the University of Colorado Graduate School. Computer time for some simulations was provided by an Intel and Hewlett-Packard sponsored Itanium-2 system (rx5670), granted to the DRACO Research Group at the University of Colorado, under the direction of Prof. Dan Connors.

## Contents

<b>Chapter</b>	
<b>1</b> Introduction	1
1.1 The effective refractive index of photonic crystals . . . . .	2
1.2 Metamaterial waveguides . . . . .	4
1.3 Coated-opal photonic crystals . . . . .	6
<b>2</b> Dynamic properties of photonic crystals and their effective refractive index	8
2.1 Summary . . . . .	8
2.2 Introduction . . . . .	8
2.3 Defining effective index . . . . .	10
2.3.1 Classical theory and the long-wavelength limit . . . . .	10
2.3.2 Equifrequency surfaces of periodic structures . . . . .	12
2.3.3 Finite structures: reflection and refraction . . . . .	13
2.3.4 Phase and group indices . . . . .	14
2.4 Case Study: Photonic crystals with band index less than one . . . . .	14
2.4.1 Silver-air thin wire metamaterial . . . . .	14
2.4.2 Hexagonal photonic crystals . . . . .	16
2.4.3 Square photonic crystals . . . . .	20
2.5 Discussion . . . . .	22
2.6 Conclusions . . . . .	25

<b>3</b>	Imaging properties of negative-effective-index photonic crystal slabs and index-equivalent homogeneous slabs	26
3.1	Summary . . . . .	26
3.2	Introduction and Methods . . . . .	26
3.3	Results . . . . .	27
3.4	Conclusion . . . . .	31
<b>4</b>	Ultralow Index Metamaterials	33
4.1	Summary . . . . .	33
4.2	Introduction . . . . .	33
4.3	Background research and its relation to ULIM . . . . .	34
4.4	Theory . . . . .	35
4.5	Dispersion diagram . . . . .	38
4.6	Refraction at a planar interface and calculation of the effective index . .	39
4.7	Reflection at a planar interface . . . . .	41
4.8	Discussion . . . . .	43
4.9	Conclusions . . . . .	44
<b>5</b>	Waveguiding in air by total external reflection from ultra-low index metamaterials	45
5.1	Summary . . . . .	45
5.2	Introduction . . . . .	45
5.3	Methods . . . . .	46
5.4	Results . . . . .	47
5.5	Discussion . . . . .	48
5.6	Conclusion . . . . .	51
<b>6</b>	Near-IR Total External Reflection Metamaterial Waveguides and Scaling limita-	

tions in optical metamaterials	52
6.1 Summary . . . . .	52
6.2 Ultra-low index optical metamaterials . . . . .	52
6.3 Waveguide with ultralow index metamaterial cladding . . . . .	53
6.4 One-Dimensional Stack . . . . .	56
6.5 Conclusion . . . . .	58
<b>7</b> Modifying silica opal photonic crystal spectra with thin conformal alumina coat- ings	59
7.1 Summary . . . . .	59
7.2 Introduction . . . . .	59
7.3 Methods . . . . .	61
7.4 Numerical Simulation . . . . .	62
7.5 Results . . . . .	63
7.6 Conclusions . . . . .	65
<b>8</b> Photonic band gap in the near-IR with tungsten-coated artificial opals	66
8.1 Summary . . . . .	66
8.2 Introduction . . . . .	66
8.3 Methods . . . . .	69
8.4 Results . . . . .	70
8.5 Conclusions . . . . .	73
<b>9</b> Conclusions and future work	75
9.1 Effective refractive index . . . . .	75
9.2 Ultralow index metamaterials . . . . .	76
9.3 Coated-opal photonic crystals . . . . .	77

**Bibliography**

78

**Appendix**

<b>A</b> Convergence of numerical predictions of first-order opal Bragg maxima	89
<b>B</b> Convergence of transfer-matrix method predictions of metal-coated opal cutoff frequencies	93

Tables

Table

7.1 First-order diffraction maxima  $\lambda_{\max}$ , silica opal, experimental and numerical. . . . . 63

8.1 Tungsten-coated opal, geometric parameters, experimental and numerical 69

8.2 Tungsten-coated opal photonic crystals, cutoff wavelengths  $\lambda_c$ ,  $\langle 111 \rangle$  orientation, experimental and numerical predictions . . . . . 73

## Figures

### Figure

2.1	Silver wire metamaterial, effective refractive index $n_{\text{eff}}$ . . . . .	15
2.2	Silver wire metamaterial, dispersion curve . . . . .	16
2.3	Silver wire metamaterial, $\mathcal{R}(\theta)$ . . . . .	17
2.4	Dielectric photonic crystal, pillars in air, hexagonal lattice, dispersion curve and band index $n_{\text{eff}}^{\text{d}}$ . . . . .	17
2.5	Dielectric photonic crystal, pillars in air, hexagonal lattice, $\mathcal{R}(\theta)$ . . . .	18
2.6	Dielectric photonic crystal, pillars in hexagonal lattice, $\mathcal{T}(\omega)$ , $\Gamma$ - $M$ . . . .	19
2.7	Dielectric photonic crystal, pillars in hexagonal lattice, $\mathcal{T}(\omega)$ , $\Gamma$ - $K$ . . . .	19
2.8	Dielectric photonic crystal, hexagonal lattice of holes, dispersion curve, band index $n_{\text{eff}}^{\text{d}}$ . . . . .	20
2.9	Dielectric photonic crystal, air holes in dielectric, hexagonal lattice, $\mathcal{R}(\theta)$	20
2.10	Dielectric photonic crystal, hexagonal lattice of holes, $\mathcal{T}(\omega)$ , $\Gamma$ - $M$ . . . .	21
2.11	Dielectric photonic crystal, hexagonal lattice of holes, $\mathcal{T}(\omega)$ , $\Gamma$ - $K$ . . . .	21
2.12	Dielectric photonic crystal, pillars in air, square lattice, dispersion curve and band index $n_{\text{eff}}^{\text{d}}$ . . . . .	22
2.13	Dielectric photonic crystal, pillars in air, square array, $\mathcal{R}(\theta)$ . . . . .	23
2.14	Dielectric photonic crystal, pillars in air, square array, $\mathcal{T}(\omega)$ . . . . .	23
3.1	Dielectric photonic crystal, air holes, hexagonal lattice, $n_{\text{eff}}^{\text{d}} = -1.0$ , $\mathcal{R}(\theta)$	28

3.2	Imaging, air holes, hexagonal lattice, $n_{\text{eff}}^{\text{d}} = -1.0$ . . . . .	28
3.3	Imaging, vary object distance, air holes, hexagonal lattice, $n_{\text{eff}}^{\text{d}} = -1.0$ .	29
3.4	Imaging, electric field plot, $n_{\text{eff}} < 1$ metamaterial lens . . . . .	30
3.5	One-axis power, $n_{\text{eff}} < 1$ metamaterial lens and equiv. homogeneous lens	30
3.6	Imaging properties, $n_{\text{eff}} < 1$ metamaterial lens . . . . .	31
4.1	Diagram: refraction & reflection from ultralow index metamaterial . . .	36
4.2	Refractive index of silver at visible and near-IR wavelengths . . . . .	37
4.3	Silver-air metamaterial, effective refractive index, analytical prediction. .	38
4.4	Wire-air metamaterial, band diagram, perfectly conducting wires . . . .	39
4.5	Silver-air metamaterial, electric field inside slab, $\lambda_0 = 1.0 \mu\text{m}$ . . . . .	39
4.6	Silver-air metamaterial, effective refractive index, numerical predictions	40
4.7	Silver-air metamaterial, $\mathcal{R}(\theta)$ , total external reflection, $\lambda_0 = 0.5 \mu\text{m}$ . . .	42
4.8	Silver-air metamaterial, $\mathcal{T}(\theta)$ , $\lambda_0 = 0.5 \mu\text{m}$ . . . . .	43
5.1	Silver-wire metamaterial, $n_{\text{eff}}$ as a function of wire width $b$ , $\lambda_0 = 0.5 \mu\text{m}$	47
5.2	Metamaterial slab waveguide, loss vs. wire width, $\lambda_0 = 0.5 \mu\text{m}$ . . . . .	47
5.3	Silver-wire metamaterial waveguide, mode profiles, visible . . . . .	49
6.1	Diagram: refraction and reflection from ultralow index metamaterial . .	53
6.2	Silver-wire metamaterial, $n_{\text{eff}}$ as a function of wire width $b$ , $\lambda_0 = 1.55 \mu\text{m}$	53
6.3	Metamaterial slab waveguide, attenuation vs. wire width, $\lambda_0 = 1.55 \mu\text{m}$ .	54
6.4	Silver-wire metamaterial waveguide, mode profiles, near-IR . . . . .	54
6.5	Silver films, $n$ vs. film thickness . . . . .	55
6.6	Metamaterial waveguide, effect of ultra-thin wire on loss . . . . .	55
6.7	Ag-MgF <sub>2</sub> stack, conv. of numerically calculated $n_{\text{eff}}$ to analytical value .	58
6.8	Ag-MgF <sub>2</sub> stack, $n_{\text{eff}}$ computer analytically and numerically . . . . .	58
7.1	Alumina-coated silica opal: $\lambda_{\text{max}}$ shift vs. coating thickness . . . . .	64

7.2	Alumina-coated silica opal: range of deposition rates based on $\lambda_{\max}$ shift	64
8.1	Thin film reflectivity, tungsten and silver . . . . .	70
8.2	Tungsten-coated opal, $2r=700$ nm, $\mathcal{R}(\lambda_0)$ , experimental and numerical .	71
8.3	Tungsten-coated opal, $2r=1000$ nm, $\mathcal{R}(\lambda_0)$ , experimental and numerical	72
8.4	Tungsten-coated opal, $2r=1600$ nm, $\mathcal{R}(\lambda_0)$ , experimental and numerical	72
8.5	Silver-coated opals, $2r=700, 1000, 1600$ nm, $\mathcal{R}(\lambda_0), \langle 100 \rangle$ . . . . .	74
A.1	Convergence, silica opal spectra, $d_{111}=216$ nm, 32 periods, 96 sphere planes	91
A.2	Convergence, silica opal spectra, 5-nm alumina coating . . . . .	91
A.3	Convergence, silica opal spectra, 16-nm alumina coating . . . . .	92
A.4	Convergence, silica opal spectra, 33-nm alumina coating . . . . .	92
B.1	Metal-coated opals, numerical simulation, $\lambda_c$ convergence with mesh density	93

## Chapter 1

### Introduction

In its broadest sense, optical engineering concerns controlling how light propagates, that is, its behavior at interfaces, direction of propagation, its polarization, and its angular and optical frequency content. Doing so involves the design and fabrication of optical components and devices such as lenses, prisms, mirrors, and waveguides, all of which determine light propagation based on their geometry and refractive index. While Maxwell's equations provide a general description of light propagation, the concept of refractive index is central to its application in macroscopic problems such as refraction and reflection, which lead to Snell's law and the Fresnel formulae.

In many photonic structures composed of two or more dielectrics, such as waveguides and photonic band gap structures, the ratio of the component refractive indices or dielectric constants is critical to their performance. Therefore, finding ways to increase this contrast would be extremely useful. This dissertation concerns techniques of increasing the index contrast through the use of metallic features in photonic crystals to modify the performance of conventional optical components and materials.

The first involves photonic crystals engineered to have the real part of their effective refractive index less than one at visible and near-IR wavelengths. In designing such structures, I developed two methods of defining the effective refractive index of finite photonic crystals, compared their predictions to a commonly-used method involving the photonic crystal's band structure, and determined the conditions for which these three

definitions of the effective index are consistent.

The second method of increasing index contrast involves coating synthetic opal photonic crystals with a thin metal coating. Such a structure can be engineered to have a complete photonic band gap at visible and near-IR wavelengths. Opals with tungsten coatings have potential applications in efficient lighting and thermophotovoltaic devices. The band gaps in such photonic crystals are highly sensitive to the tungsten film thickness.<sup>vFJSD<sup>+</sup>04</sup> In this dissertation, I develop a method of determining the film thickness deposited on opals, and validate experimental results showing band gap effects in tungsten-coated silica opals.

## 1.1 The effective refractive index of photonic crystals

Just as a crystal is a periodic array of atoms or molecules whose geometry and atomic or molecular properties determine the dispersion relation of an electron inside of it, a photonic crystal is a subwavelength periodic array of different materials where the geometry and material properties determine the dispersion relation of electromagnetic radiation propagating in it. Because of their intriguing optical properties, photonic crystals are being studied for an increasing number of applications including the creation of more efficient light sources, low threshold lasers, and integrated photonics.<sup>JMW95</sup>

For specific wavelength ranges, some photonic crystals are classified as *metamaterials*, where an effective refractive index describes their optical properties. In other situations, photonic crystals are classified as photonic band gap structures, which forbid propagation of light of certain wavelengths in one or more directions. The photonic crystals studied here include both metal-dielectric metamaterials and photonic band gap structures.

Metamaterials are an extension of the concept of artificial dielectrics, which have been considered for microwave frequencies.<sup>Bro60</sup> They derive their properties from the sub-wavelength structure of their component materials in a similar way that homoge-

neous dielectrics derive their optical properties from the nanometer-scale structure of their atoms. When the wavelength of the field interacting with the structure is much longer than the unit cell  $a$ , the metamaterial can be treated as a homogeneous dielectric with macroscopic parameters such as effective refractive index  $n_{\text{eff}}$ . Proper choice of component materials and geometries can yield metamaterials with novel optical properties to control light in unconventional ways.<sup>Pen03</sup>

While traditional methods of deriving an effective refractive index apply in the long wavelength limit,<sup>Lak96</sup> photonic crystals have recently been assigned an effective refractive index,  $n_{\text{eff}}^d$ , based on their dispersion curve at wavelengths only slightly larger than the unit cells. Widely-cited studies have shown photonic crystals to have both negative and positive refractive index values not found in homogeneous materials, and have postulated device applications based on them. This dissertation explores the necessary conditions for the validity defining an effective refractive index by this method. In doing so, I develop two other methods of computing  $n_{\text{eff}}$  based on the photonic crystal's refraction and reflection properties that in some cases yield the same results as the one predicted by the dispersion curve.

Chapters 2 and 3 show that  $n_{\text{eff}}^d$  is misleading for frequencies corresponding to strongly-modulated Bloch eigenmodes of the photonic crystal. The refractive index defined in this manner does not necessarily predict the reflection and transmission properties when used in the Fresnel formulae, which limits the value of assigning such structures an effective refractive index. However, as addressed in Chapter 4, metamaterials consisting of thin wires can behave, upon both refraction and reflection like a low-loss dielectric with refractive index less than one. Such ultralow index metamaterials (ULIMs) operate at wavelengths much larger than the wire thickness, but only slightly larger than twice the unit cell.<sup>SP03</sup>

A subwavelength structure with an effective refractive index should refract light like a homogeneous structure with the corresponding refractive index. If the struc-

ture's features are small enough compared to the unit cell and wavelength, an incident plane wave should be refracted as a plane wave, and the wavelength inside the material should be  $\lambda = \frac{\lambda_0}{n_{\text{eff}}}$ , where  $\lambda_0$  is the free-space wavelength. This leads to one of the available methods to calculate the effective index. By computing the wavelength inside the metamaterial, we can define the effective refractive index by the ratio of the free-space wavelength to the refracted wavelength. For example, a metamaterial consisting of silver wires of diameter  $d=30$  nm in a 200-nm square array has an effective refractive index  $n_{\text{eff}} = 0.62+0.024i$  at  $\lambda_0= 1 \mu\text{m}$ . This structure is the subject of Chapter 4.

Likewise, a sub-wavelength structure with an effective refractive index should also have the same reflective properties as a homogeneous structure with the same refractive index. While normal-incidence reflection and transmission coefficients have been used to define the complex refractive index of heterogeneous structures,<sup>SSMS02</sup> we have used the Fresnel formulae to find the complex refractive index of a homogeneous dielectric slab whose angle-dependent reflectivity  $\mathcal{R}(\theta)$  best matches that of the metamaterial. Compared to the single-angle method, this multiple-angle method is more robust, as reflectivity values must match well for all angles, and hence it has little tolerance for the metamaterial's anisotropy. The effective refractive index computed with this method agrees with that derived from normal-incidence refraction.<sup>SP03</sup>

## 1.2 Metamaterial waveguides

ULIMs exhibit a new optical property at visible wavelengths: total external reflection (TER). TER occurs when light propagating in vacuum is incident on a medium with a refractive index less than unity at an angle exceeding the critical angle defined by Snell's law. For angles exceeding the critical angle, as defined for the lossless case, the refracted waves are evanescent, and the reflectivity is very close to unity.

Conventional waveguides operate by total internal reflection, where the index of the core material is greater than that of the cladding. ULIMs open up the possibility

of hollow waveguides based on TER. Chapter 5 shows that slab waveguides with hollow core and metamaterial cladding are feasible for visible and near-IR wavelengths. The guiding is produced by TER because the cladding's refractive index (real part) is smaller than the core refractive index. Numerical simulations have shown that ULIM waveguides can propagate visible  $\lambda_0 = 500\text{-nm}$  light more than 60 wavelengths, which compares favorably with current plasmonic waveguides for applications in photonic integrated devices.<sup>SP04a</sup> The limitation is the inherent loss of metamaterials with ultralow index. Both the mode profile and the attenuation agree with analytical predictions based on the effective index.

Unlike photonic crystal waveguides, which require a photonic band gap to confine light, metamaterial cladding waveguides guide light by TER and do not require a band gap. Similarly to photonic crystal waveguides, ULIM waveguides have the potential to guide light along sharp turns with low losses, although this remains to be demonstrated. Moreover, insertion losses should be lower in ULIM waveguides because the modes decay into the cladding as they do in conventional dielectric waveguides, which reduces the mode-matching problem.

Metamaterials can be designed to have a wide range of effective refractive index values opening up new opportunities for device applications. Since they behave very similarly to their equivalent homogeneous materials, designers can optimize device performance with analytical and numerical models based on homogeneous materials. These require less computation and modeling time than a full numerical simulation of the sub-wavelength features, which can be reserved for final design stages.

Silver is the best metal candidate at visible wavelengths because both the real and imaginary parts of its refractive index are small. Yet, the refractive index of silver clusters smaller than approximately 15 nm has been shown to diverge from their bulk values, which could make them unsuitable for certain ULIM designs.<sup>SP04b</sup> This is discussed in Chapter 6.

### 1.3 Coated-opal photonic crystals

For a photonic crystal to exhibit a photonic band gap, the ratio of the dielectric constants (or electric permittivity)  $\epsilon$ , of the constituent materials must exceed a threshold value. Since dielectrics do not satisfy this condition at visible and near-IR wavelengths, metals are often employed because the real part of their dielectric constant is large and negative. Metals achieve the required contrast in dielectric constant, but because the plasma wavelengths of metals are close to the visible and near-IR wavelengths, these structures attenuate modes significantly. Hence, their applications tend to involve reflection, as discussed above for metamaterials, and emission, which will be discussed below.

Compared to other structures with three-dimensional periodicity, an inverted opal structure can be fabricated affordably and reliably. The opal structure is created by a self-assembly of dielectric nanospheres,<sup>NAM<sup>+</sup>97</sup> typically made of silica, which is then coated using one of a variety of techniques. One of them is atomic layer deposition (ALD) which yields uniform and conformal coatings with a predictable thickness on planar and opal substrates.

While self-assembly of silica spheres results in synthetic opals with relatively few defects, not all metals can adhere to them in the ALD process. Hence, materials that can both coat the silica opals conformally and allow for uniform and conformal deposition of metal over them are used as adhesion layers between the silica and metal.

Compared to a flat substrate, opals present a dramatically different deposition environment to the ALD precursor molecules that form the coating, and direct measurement of the coating thickness is difficult. Since coating thickness significantly affects the spectrum and band gap properties of a photonic crystal, the ability to predict this is critical for designing photonic band gap structures. In Chapter 7 I discuss to what extent deposition rates for flat substrates apply to opals.

At visible and near-IR wavelengths most dielectrics do not have electric permittivity  $\epsilon$  values sufficient to achieve a photonic band gap. Since for metals,  $\text{Re}(\epsilon)$  is large and negative in this wavelength range, they are candidates for photonic crystals with band gaps in the visible or near-IR. When heated, a metal emits the most radiation at the peak of its blackbody radiation spectrum. Yet, if this metal is a component of a photonic crystal with a photonic band gap at wavelength corresponding to this radiation peak, the crystal will not emit light at these wavelengths when heated. Instead, they will emit radiation at wavelengths corresponding to high density of states.

A photonic crystal engineered to have forbidden modes at near-IR wavelengths and allowed modes (and hence a high density of states) at visible wavelengths has potential applications for efficient lighting and thermophotovoltaic cells. Since tungsten has a relatively high melting point, it can be heated ( $T \approx 2000$  K) such that its peak emission is at near-IR wavelengths and allows for efficient visible light generation. Engineering this band gap is the subject of Chapter 8, where I validate the experimental evidence of a near-IR band gap in tungsten-coated silica opals.

## Chapter 2

### Dynamic properties of photonic crystals and their effective refractive index\*

#### 2.1 Summary

The reflection and refraction properties of light at an interface between two media are usually classified into kinematic and dynamic. Both are determined by the refractive indices of the media. The kinematic properties refer to the direction of light propagation, while the dynamic properties refer to the polarization, magnitude and phase changes of the reflected and refracted waves.

Metamaterials and photonic crystals are often assigned an effective refractive index defined by their dispersion curves. This chapter shows that while the kinematic properties are consistent with this index definition, in some cases the dynamic properties are not. This observation has important implications for photonic crystal understanding and design because it shows that their rich physical phenomena cannot always be simplified to a description in terms of an effective refractive index.

#### 2.2 Introduction

The refractive index is a macroscopic material property that determines how light reflects and refracts at the interface between two media. Jackson<sup>Jac75</sup> classifies the phenomena of reflection and refraction into two classes: kinematic and dynamic. The

---

\* A version of this chapter was originally published as Ref. SP05c.

kinematic properties describe how light propagation changes direction at an interface and are a direct consequence of the conservation of linear momentum. The dynamic properties describe the intensities, phase changes, and polarization of reflected and refracted waves through the Fresnel formulae and are a consequence of the continuity of the electromagnetic field (tangential components of the electric and magnetic fields).

As discussed in Chapter 1, metamaterials are a class of photonic crystals that have the optical properties of a homogeneous dielectric, and hence can be assigned an effective refractive index. Traditional methods of deriving an effective refractive index apply in the long-wavelength limit. However, metamaterials consisting of thin wires can have optical properties of a low-loss dielectric at wavelengths much larger than the wire thickness, but only slightly longer than twice the unit cell.<sup>SP03,SP04a</sup> Recently, photonic crystals have also been assigned an effective refractive index based on their band structure at wavelengths only slightly longer than the unit cell.<sup>DB94,LHWJ96,Not00,GET00,BMS<sup>+</sup>04</sup>

The purpose of this chapter is to analyze the limits of applicability of the different definitions of effective refractive index. I compare three methods for defining and computing the effective refractive index of photonic crystals when the long-wavelength limit does not apply, that is, when the free-space wavelength  $\lambda_0$  is not much greater than the unit cell ( $\lambda_0 \gtrsim a$ ). The first method uses the angle-dependent reflectivity  $\mathcal{R}(\theta)$  at the interface of a finite structure, leading to  $n_{\text{eff}}^{\text{R}}$ . The second considers the normal-incidence refraction into a finite structure, leading to  $n_{\text{eff}}^{\text{r}}$ . Finally, the third method derives the index from the dispersion curve of an infinite periodic structure, leading to  $n_{\text{eff}}^{\text{d}} = \frac{c_0 k}{\omega}$ . In some instances, the index  $n_{\text{eff}}^{\text{d}}$  is constant regardless of the propagation direction so it defines a circular equifrequency surface (EFS) in  $\mathbf{k}$ -space for 2D photonic crystals.<sup>Not00</sup>

The new results presented here are that in some cases, such as in silver nanowire arrays at visible wavelengths,  $n_{\text{eff}}^{\text{d}}$  predicts both its kinematic and dynamic properties:  $n_{\text{eff}}^{\text{d}} = n_{\text{eff}}^{\text{R}} = n_{\text{eff}}^{\text{r}}$ , however, for certain dielectric photonic crystals operating near the band edge,  $n_{\text{eff}}^{\text{d}}$  predicts only their kinematic properties. Specifically, as a case study, I con-

sider several photonic crystals for which  $n_{\text{eff}}^{\text{d}} < 1$ , as they exhibit several interesting properties.<sup>SP03</sup>

This chapter is organized as follows. In Section 2.3 I review methods of defining  $n_{\text{eff}}$  both in the long-wavelength limit and close to resonance, when  $\lambda_0 \gtrsim a$ . In Section 2.4 I use the three methods mentioned above to find the effective refractive index of several photonic crystal structures for which  $n_{\text{eff}} < 1$ . Finally, in Section 2.5 I discuss the limitations of the different definitions and their physical explanation. Section 2.6 presents the conclusions of this analysis.

## 2.3 Defining effective index

### 2.3.1 Classical theory and the long-wavelength limit

To begin a discussion of how to determine the effective refractive index of a periodic structure with sub-wavelength feature sizes, it is appropriate to review the standard derivation of the refractive index of a homogeneous isotropic dielectric, which results in the Clausius-Mossotti equation. Also known as the Lorentz-Lorenz relation, it expresses the dielectric constant  $\epsilon$  of a homogeneous material as a function of the molecular density  $N$  and polarizability  $\alpha$ :  $\frac{\epsilon-1}{\epsilon+2} = \frac{4\pi}{3} N\alpha$ . This formula works best for dilute gases, and is a good approximation for isotropic dielectrics with low dielectric constants.<sup>Jac75,RMC93</sup>

Now consider a sub-wavelength periodic structure with  $a \ll \lambda_0$  consisting of  $N$  materials, denoted by subscript  $i$ , with dielectric constant  $\epsilon_i$ , density  $N_i$ , polarizability  $\alpha_i$ , and volume fraction  $f_i$  where  $\sum_{i=1}^N f_i = 1$ . Finding the effective dielectric constant involves simply replacing  $N\alpha$  in the Clausius-Mossotti equation with  $\sum_{i=1}^N N_i\alpha_i$ , and then expressing this in terms of the component dielectric constants and fill-factors. This results in the Lorentz-Lorenz effective medium approximation, which was generalized

by Maxwell-Garnett and then Bruggeman. The most general expression is:<sup>Asp82, CVG<sup>+</sup>91</sup>

$$\frac{\epsilon_{\text{eff}} - \epsilon_0}{\epsilon_{\text{eff}} + 2\epsilon_0} = \sum_{i=1}^N f_i \frac{\epsilon_i - \epsilon_0}{\epsilon_i + 2\epsilon_0}.$$

The above derivation does not account for the specific geometry of the structure. Given the dielectric constants and fill-factors of the component materials, their orientation with respect to the electric field is the next important factor determining the structure's effective dielectric constant. Components of the electric field normal to surfaces induce a polarization charge density on them, which then screens the surface's effect on the field from other parts of the medium and reduces the influence of that feature on the effective dielectric constant.<sup>Asp82</sup>

In one limiting case, the structure is a multi-layer stack where all interfaces are parallel or perpendicular to the applied field. To first order, this effective medium approach yields the same effective dielectric constants as those derived using the field continuity for structures exhibiting form birefringence:  $\epsilon_{\parallel} = f_a \epsilon_a + f_b \epsilon_b$ ,  $\epsilon_{\perp} = (\frac{f_a}{\epsilon_a} + \frac{f_b}{\epsilon_b})^{-1}$ .<sup>BW80, Ryt56</sup> These expressions, known as the Wiener bounds, define the range of effective dielectric constant values for a two-component sub-wavelength structure of any geometry. Given the fill factors, the range of effective index values narrows to what is known as the Hashin-Shtrickman bounds. Other geometrical characteristics further narrow the range of accessible  $\epsilon_{\text{eff}}$  values.<sup>Asp82, HS62, Sih02</sup>

Artificial dielectrics have been typically composed of arrays of inclusions such as conducting wires, strips, spheres, discs, or plates designed for light-weight microwave lenses. The above classical methods have been used to derive the effective properties of such structures, but transmission-line analysis became popular because its applicability and familiar mathematical form gave additional insight into the physics of the problem.<sup>Bro60, Bra54</sup> Typically, the operating wavelength for artificial dielectrics is much larger than both the unit cell  $a$  and the inclusion width.<sup>Bro53</sup>

Several other methods for the analysis of artificial dielectrics have since become

popular. These include analytical methods known as homogenization techniques and effective medium theory. They have been developed to find the effective optical properties of layered media,<sup>Ryt56</sup> sub-wavelength gratings,<sup>LH98,LH03</sup> and dielectric photonic crystals.<sup>HKA99,KHA02</sup> Homogenization of metal photonic crystals with thin wires<sup>FB97,Fel02</sup> have resulted in analytical expressions of the dielectric constant resembling those derived with transmission-line techniques.<sup>Bro53</sup> Numerical methods of computing effective optical properties include Fourier expansion methods.<sup>BDM82,LLL96</sup>

The above methods of defining effective refractive index apply either in the long wavelength limit, where  $a \ll \lambda_0$ , or when the largest inclusion (with dimension  $b$ ) in a host medium is much smaller than the unit cell ( $b \ll a$ ). The latter condition allows the wavelength to be just slightly larger than the unit cell. Yet, several recent studies have reported photonic crystals<sup>SP03,LHWJ96,Not00,GET00,BMS<sup>+</sup>04,FES03,QTSJ03,PLVS03</sup> that exhibit properties of homogeneous dielectrics but do not satisfy any of these conditions. This is discussed in the following sections.

### 2.3.2 Equifrequency surfaces of periodic structures

Another method of defining an effective refractive index is by analyzing equifrequency mode surfaces (EFS), the wavevector-surface defined by modes of a single frequency.<sup>LHWJ96,Not00,GET00,BMS<sup>+</sup>04</sup>

For light propagating in the  $x$ - $y$  plane, a homogeneous dielectric material has a wavevector surface that satisfies the relation  $k_x^2 + k_y^2 = nk_0^2$  where  $k_0 = \frac{\omega}{c_0}$ . If the wavevector surface of a two-dimensional photonic crystal has a circular EFS satisfying  $k_x^2 + k_y^2 = n_{\text{eff}}^d k_0^2$ , then it has an effective refractive index  $n_{\text{eff}}^d$  at frequency  $\omega = c_0 k_0$ . This is a phase refractive index and the material is considered isotropic at that frequency.

To define an effective index for light propagating along the symmetry axis of a periodic structure,<sup>DB94</sup> one needs only to consider the photonic band structure, which is simply a subset of the  $\omega(\mathbf{k})$  values used to generate equifrequency surfaces such that the

wave-vector  $\mathbf{k}$  is on a symmetry axis. In this chapter I will distinguish between  $n_{\text{eff}}^{\text{EFS}}$ , which derives from a circular equipfrequency surface, which holds for all directions, and the band index,  $n_{\text{eff}}^{\text{d}}$ , which applies to a single propagation direction.

### 2.3.3 Finite structures: reflection and refraction

So far, I have discussed methods of defining effective refractive index of an infinite sub-wavelength periodic structure. Yet, for real applications, the refractive index of a material also manifests itself at its boundary with another medium, that is, it determines reflection, transmission, and refraction of light at an interface. Therefore, there are two other methods to define the effective refractive index, according to reflection and refraction.

A definition of effective index consistent with the dynamic properties at interfaces between homogeneous materials and photonic crystals should provide the proper reflection and transmission coefficients as predicted by Fresnel formulae.

A single-angle method defines the complex refractive index of a photonic crystal as a function of its normal-incidence reflection and transmission coefficients in such a way that it provides the same properties as a homogeneous structure with the corresponding effective refractive index.<sup>SSMS02</sup>

Alternatively, in the case of isotropic photonic crystals, the Fresnel formulae can be used to find the complex refractive index of a homogeneous dielectric whose angle-dependent reflectivity  $\mathcal{R}(\theta)$  best matches that of the photonic crystal.<sup>SP03</sup> Compared to the single-angle method, this multiple-angle method is more robust because the computed  $n_{\text{eff}}$  is calculated from the reflectivity at various angles.

Moreover, a photonic crystal with an effective refractive index should also refract light like a homogeneous structure with the corresponding refractive index. If the structure's features are small enough compared to the unit cell and wavelength, an incident plane wave will be refracted as a mode that is very similar to a plane wave,

and the effective index will be  $n_{\text{eff}}^r \doteq \frac{\lambda_0}{\lambda}$ , where  $\lambda$  is the wavelength inside the photonic crystal.<sup>SP03</sup> To the extent that the propagating Bloch wave in the photonic crystal resembles a plane wave, calculating the wavelength inside the photonic crystal provides an additional method for estimating the effective index.

### 2.3.4 Phase and group indices

Until now I have discussed the effective phase refractive index of photonic crystals, and not the group refractive index. The group refractive index is defined as  $n_{\text{eff}}^g = \frac{v_g}{c_0}$ , where the group velocity is  $v_g = \frac{\partial \omega}{\partial \mathbf{k}}$ . Therefore, one method of finding  $n_{\text{eff}}^g$  is by computing the slope of the dispersion curve, which provides the group velocity.

Another method to calculate the group effective index is by calculating the transmission through a Fabry-Perot resonator composed of the photonic crystal under study. The peak transmission frequency spacing of a Fabry-Perot resonator is related to its group refractive index,<sup>Vau89</sup>  $n_{\text{eff}}^g$ . Previous research has shown that the group index calculated by this method agrees with the group index calculated from the band diagram.<sup>Sak97, JYZ02</sup>

## 2.4 Case Study: Photonic crystals with band index less than one

### 2.4.1 Silver-air thin wire metamaterial

I start by applying the various definitions of phase effective index to a metamaterial composed of silver wires embedded in air. Because of the losses of silver at optical frequencies, these metamaterials are inherently lossy and present a complex refractive index. Reference SP03 showed that metal-dielectric metamaterials can be tailored to present the real part of the effective index below unity with the imaginary part significantly lower than the bulk metal.

Here I analyze a two-dimensional metamaterial with a square array of cylindrical

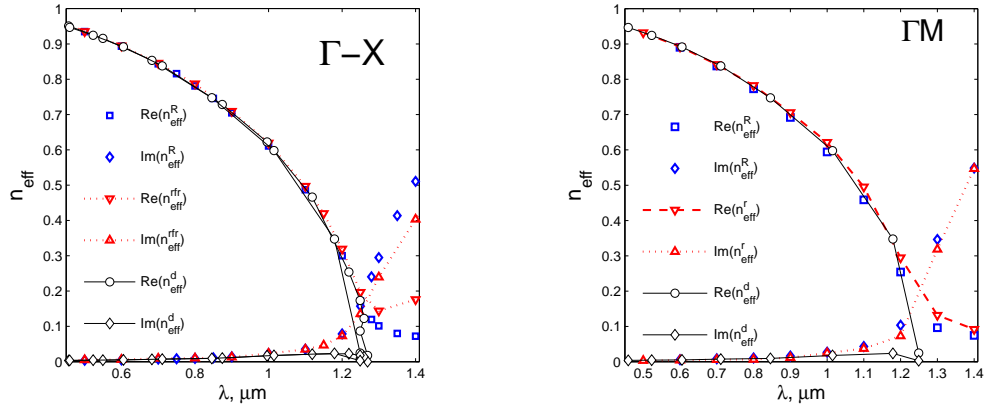


Figure 2.1: Refractive index (real and imaginary parts) of the silver-air metamaterial as a function of free-space wavelength as predicted by its dispersion curve ( $n_{\text{eff}}^d$ ) normal incidence refraction ( $n_{\text{eff}}^R$ ) and angle dependent reflectivity ( $n_{\text{eff}}^r$ ). Wire radius:  $r = 15$  nm, unit cell size:  $a = 200$  nm.

silver wires embedded in an air host medium. The unit cell is  $a = 200$  nm and the wire radius is  $r = 15$  nm. Therefore, this metamaterial does not fall in the long wavelength regime at optical frequencies. However, it behaves on refraction, reflection, and transmission as a low-loss dielectric with  $0 < \text{Re}(n_{\text{eff}}) < 1$  for wavelengths between  $0.45 \mu\text{m}$  and  $1.2 \mu\text{m}$  for light polarized parallel to the wires, as shown in Fig. 2.1.

I calculated the effective refractive index in three ways. First by using the band diagram ( $n_{\text{eff}}^d$ ), second by using reflection data matched at all angles of incidence ( $n_{\text{eff}}^R$ ), and third calculating the wavelength inside the metamaterial ( $n_{\text{eff}}^r$ ). The computations of  $n_{\text{eff}}^d$  and  $n_{\text{eff}}^r$  were performed using a finite element method,<sup>Com04</sup> while  $n_{\text{eff}}^R$  was calculated using a transfer-matrix method.<sup>Rey00b</sup>

As shown in Fig. 2.1, the three independent calculations provide consistent results for both the real and imaginary parts of the index in a wide frequency range for the two main directions  $\Gamma$ - $X$  and  $\Gamma$ - $M$ . The band diagram (Fig. 2.2) shows the real part of the eigenfrequencies corresponding to  $0 < \text{Re}(n_{\text{eff}}) < 1$ . Each eigenfrequency was computed<sup>Com04</sup> iteratively considering the frequency-dependent refractive index of silver,  $n(\omega)$ .<sup>LH91</sup>

Figure 2.2 shows that for frequencies corresponding to free-space wavelengths  $\lambda_0 \geq 2a$  ( $a \leq \frac{\lambda_0}{2}$ ), the mode is above the light line, which suggests that the wire array

has an effective refractive index  $n_{\text{eff}}^{\text{d}} = \frac{ck}{\omega}$  less than unity. This effective refractive index agrees with those predicted for reflection and refraction of finite structures, as shown in Fig. 2.1. Unlike lossless periodic media, where the imaginary part of the index, obtained from eigenfrequency calculations, is related to back reflection,<sup>YY84</sup> here it is also related to attenuation.

Figure 2.3 shows the angle-dependent reflectivity of a slab of metamaterial and compares it with that of a hypothetical homogeneous material with the same index of refraction. The apparent agreement justifies the use of the angle dependent method for the definition of an effective index  $n_{\text{eff}}^{\text{R}}$ .

### 2.4.2 Hexagonal photonic crystals

I now focus on dielectric photonic crystals which can also be designed to present a phase effective index below unit based on the equifrequency diagram. In this section I use two designs proposed by Notomi in Ref. Not00. These designs have unit cells comparable to the wavelength and therefore the long-wavelength approximations do not apply. The band diagrams and effective refractive index values derived from them were calculated with a freely available software package.<sup>JJ01</sup> While that there is a slight disagreement with the band-diagrams reported in Ref. Not00, it is irrelevant to our purposes.

The first photonic crystal is an hexagonal array of cylinders ( $n_{\text{cyl}} = 3.6$ ) with

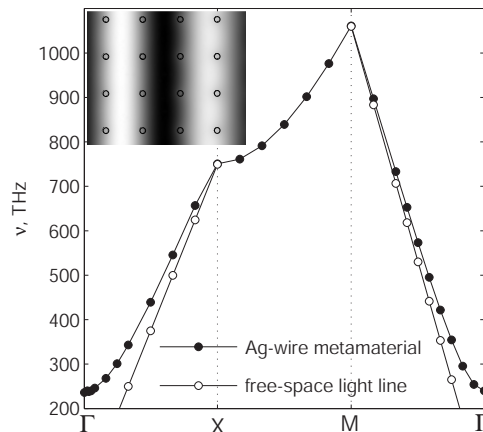


Figure 2.2: Dispersion diagram of a two-dimensional square array of silver wires. The two straight lines are the dispersion curves of light in free-space. Wire radius:  $r = 15$  nm, unit cell size:  $a = 200$  nm.

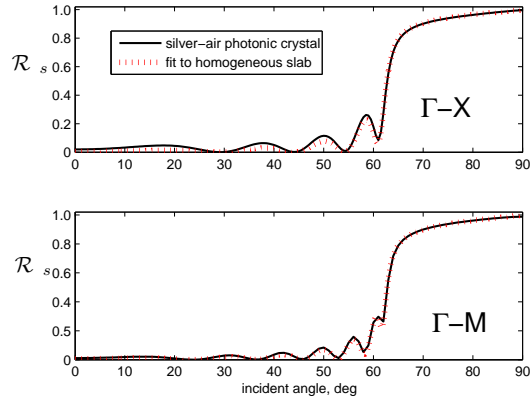


Figure 2.3: Angle-dependent reflectivity at  $\lambda_0 = 600$  nm as a function of incident angle from silver wire metamaterial slab 8 periods thick. The electric field is parallel to the wires and normal to the plane of incidence ( $s$ -polarization). Solid curve: transfer-matrix method predictions. Dotted curve: analytical calculations based on Fresnel formulae for homogeneous slabs ( $n = 0.89 + 0.005i$ ) of the same thickness as the metamaterial. Wire radius:  $r = 15$  nm, unit cell size:  $a = 200$  nm. Top: Normal incidence corresponds to  $\Gamma$ - $X$  direction. Bottom: Normal incidence corresponds to  $\Gamma$ - $M$  direction.

diameter  $2r = 0.7a$ , where  $a$  is the unit cell length. For TE modes (electric field normal to the cylinders), this structure has a circular equifrequency surface for  $\frac{a}{\lambda_0}$  between 0.59 and 0.62. These frequencies correspond to band I and band II in Fig. 2.4a. For band I,  $0 < n_{\text{eff}}^{\text{EFS}} < 0.5$ ; for band II,  $-0.8 < n_{\text{eff}}^{\text{EFS}} < 0$ , as shown in Fig. 2.4b.

Reference Not00 indicates that the effective index defined by a circular equifrequency surface is consistent with Snell's law. Here, I investigate whether this index is consistent with the dynamic properties, i.e. the Fresnel formulae. For this purpose I calculated the reflectivity from air at  $\frac{a}{\lambda_0} = 0.62$  as a function of the angle of incidence on a

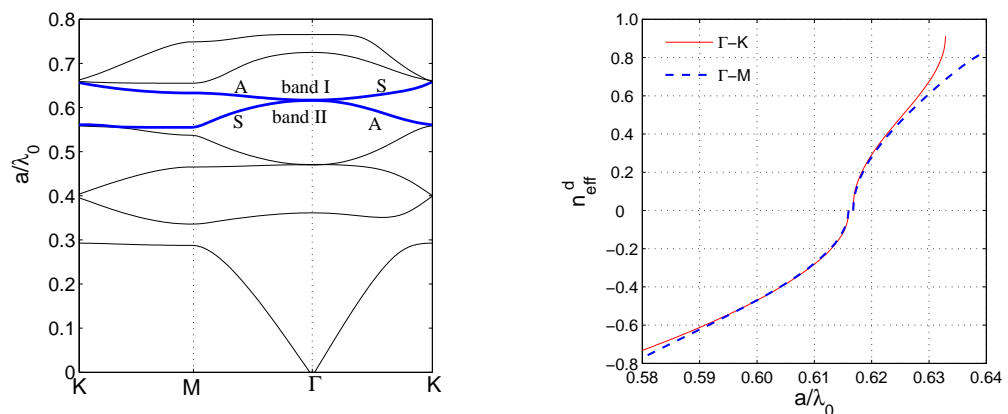


Figure 2.4: (a) Dispersion diagram of a two-dimensional hexagonal photonic crystal, unit cell  $a$ , consisting of cylinders ( $n_{\text{cyl}} = 3.6$ ) of radius  $r = 0.35a$  in air. Modes in band I are antisymmetric (A) in the  $\Gamma$ - $M$  direction and symmetric (S) in the  $\Gamma$ - $K$  direction. Band II is symmetric (S) in the  $\Gamma$ - $M$  direction and antisymmetric (S) in the  $\Gamma$ - $K$  direction. (b) Effective refractive index  $n_{\text{eff}}^{\text{d}}$  corresponding to band I and band II.

64-period wide photonic crystal slab using the transfer-matrix method.<sup>Rey00b</sup> Figure 2.5 shows the result and compares with the reflectivity of a hypothetical homogeneous material with the same index. Clearly, the photonic crystal does not reflect like a  $n < 1$  dielectric.

This behavior is the consequence of the interplay between the photonic band structure, which applies for an infinite crystal, and the mode-matching problem, which applies to the interface between the two media. In effect, while some modes can be coupled from plane waves some cannot. In contrast, metamaterials in the long-wavelength regime couple plane waves into modes which are basically plane waves and thus obey the same rules as homogeneous materials.

To illustrate this issue, I compare the band diagram and the transmission spectra. The symmetry of the modal field distributions explains in part the transmission properties of each mode. The modes are either symmetric or antisymmetric about the axis connecting the cylinder centers corresponding to the direction of propagation. For  $\Gamma$ - $M$  modes of a hexagonal lattice of unit cell  $a$ , the axis connects second-nearest neighboring cylinders, while for the  $\Gamma$ - $K$  modes, the axis connects adjacent cylinders. As mentioned

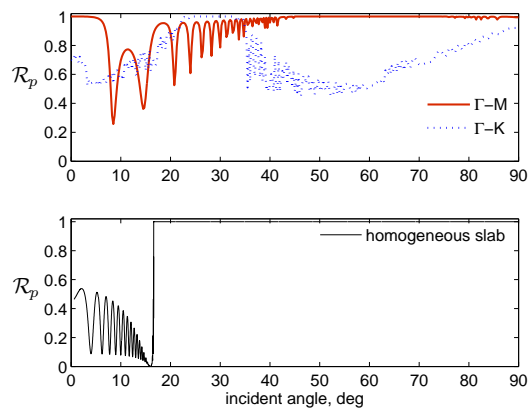


Figure 2.5: Reflectivity of finite-thickness slabs in vacuum. The electric field is normal to the cylinder axes and in the plane of incidence ( $p$ -polarization). Top: A 64-period photonic crystal slab consisting of a hexagonal array of cylinders ( $n_{\text{cyl}} = 3.6$ ) at normalized frequency  $\frac{a}{\lambda_0} = 0.62$ . Bottom: A homogeneous dielectric slab with refractive index  $n=0.286$  and the same thickness as the photonic crystal slab.

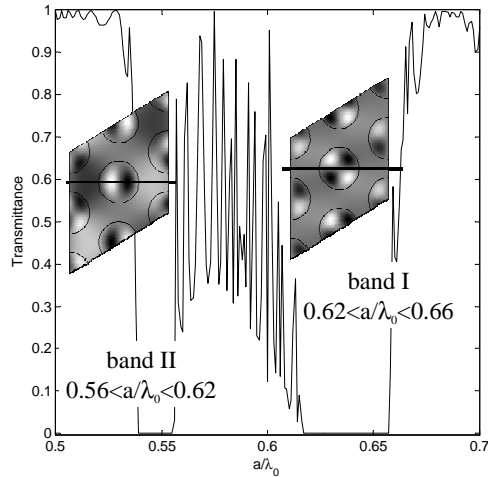


Figure 2.6: Transmission through 64 periods of the hexagonal photonic crystal described in Fig. 2.4 oriented in the  $\Gamma - M$  direction. Note that symmetric modes correspond to non-zero transmission regions, while anti-symmetric modes correspond to zero-transmission regions (insets). The lines in the mode-field plots denote the  $\Gamma - M$  propagation direction.

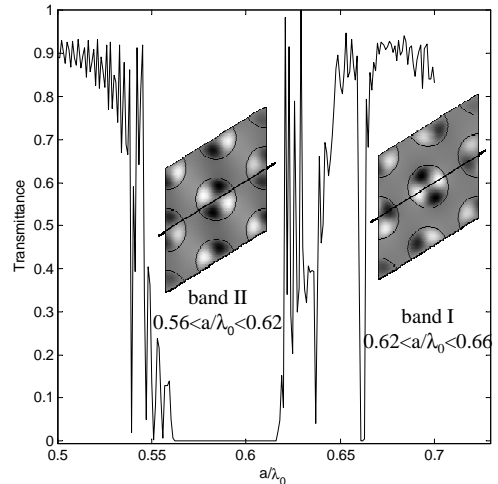


Figure 2.7: Transmission through 64 periods of the hexagonal photonic crystal described in Fig. 2.4 oriented in the  $\Gamma - K$  direction. Note that symmetric modes correspond to non-zero transmission regions, while anti-symmetric modes correspond to zero-transmission regions (insets). The lines in the mode-field plots denote the  $\Gamma - M$  propagation direction.

above, an incident plane wave propagating along the symmetry axis can couple only into symmetric modes. As shown in Figs. 2.6 and 2.7 the zero-transmission regions correspond to antisymmetric modes.

The second example of photonic crystal with circular equifrequency surface is composed of a hexagonal array of air-holes in a host medium ( $n_{\text{host}} = 3.6, 2r = 0.8a$ ).<sup>Not00</sup> For TM modes (electric field parallel to the cylinders), this structure has a circular equifrequency surface for frequencies in band I and band II in Fig. 2.8a, corresponding to an effective index  $-1 < n_{\text{eff}}^{\text{EFS}} < 0$  for band I, and  $0 < n_{\text{eff}}^{\text{EFS}} < 0.5$  for band II, as shown in Fig. 2.8b.

Again, the angle dependent reflectivity (Fig. 2.9) shows that even for the symmetric modes, the photonic crystal does not have the reflectivity of a homogeneous dielectric with  $n < 1$ . Moreover, observing the band diagram (Fig. 2.8) and transmission spectra (Figs. 2.10 and 2.11) I find zero transmission for band I and band II frequencies incident in the  $\Gamma - K$  direction.

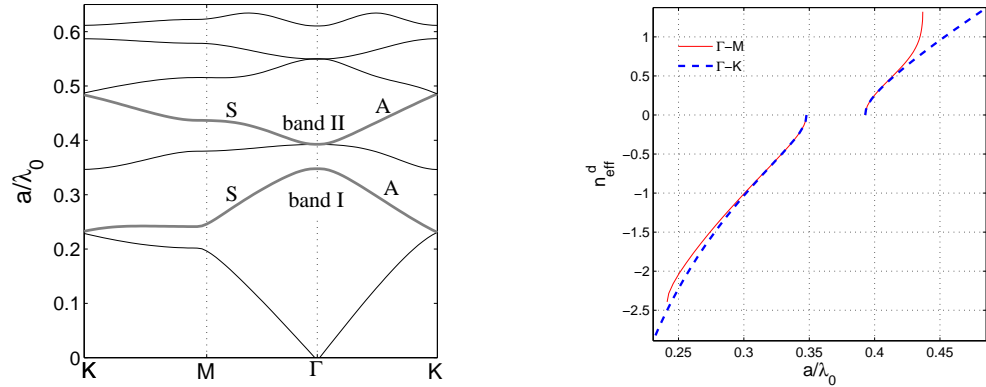


Figure 2.8: (a) Dispersion diagram of a two-dimensional hexagonal photonic crystal, unit cell  $a$ , consisting of air-holes of radius  $r = 0.40a$  in a dielectric host ( $n_{\text{host}} = 3.6$ ). Band I is symmetric (S) in the  $\Gamma$ - $M$  direction and antisymmetric (A) in the  $\Gamma$ - $K$  direction. Band II is symmetric (S) in the  $\Gamma$ - $M$  direction and antisymmetric (A) in the  $\Gamma$ - $K$  direction. (b) Effective refractive index  $n_{\text{eff}}^d$  corresponding to band I and band II.

### 2.4.3 Square photonic crystals

Gralak *et al*<sup>GET00</sup> presented a similar design of a photonic crystal with an effective refractive index composed of a square array of dielectric cylinders ( $n_{\text{cyl}} = 3.0$ ) with diameter  $2r = 0.748a$  where  $a$  is the unit cell length. For TM modes (electric field parallel to the cylinders), this structure has a circular equifrequency surface in a small frequency range close to  $\Omega_1 = 0.496$  just above the band gap.

Figure 2.12a shows the band diagram of this photonic crystal calculated using finite-element software.<sup>Com04</sup> The circular equifrequency surface at  $\Omega_1$  corresponds to the fourth band, as noted in the band diagram. As shown in the inset, both of these

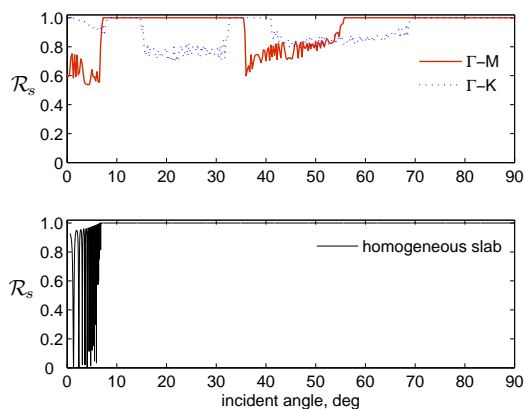


Figure 2.9: Reflectivity of finite-thickness slabs in a surrounding medium of refractive index  $n = 3.6$ . The electric field is parallel to the cylinder axes and normal to the plane of incidence ( $s$ -polarization). Top: A 64-period photonic crystal slab consisting of a hexagonal array air-cylinders in a dielectric host ( $n_{\text{host}} = 3.6$ ) at normalized frequency  $\frac{a}{\lambda_0} = 0.41$ . Bottom: A homogeneous dielectric slab with refractive index  $n=0.427$  and the same thickness as the photonic crystal slab.

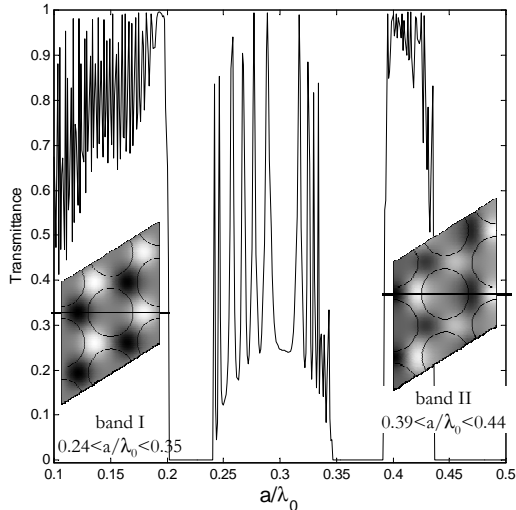


Figure 2.10: Transmission through 64 periods of the hexagonal photonic crystal described in Fig. 2.8 oriented in the  $\Gamma$ - $M$  direction. Note that symmetric modes correspond to non-zero transmission regions, while anti-symmetric modes correspond to zero-transmission regions (insets). The lines in the mode-field plots denote the  $\Gamma$ - $M$  propagation direction.

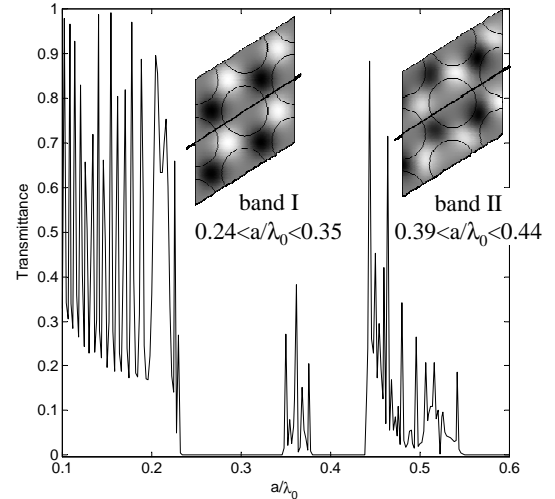


Figure 2.11: Transmission through 64 periods of the hexagonal photonic crystal described in Fig. 2.8 oriented in the  $\Gamma$ - $K$  direction. Note that symmetric modes correspond to non-zero transmission regions, while anti-symmetric modes correspond to zero-transmission regions (insets). The lines in the mode-field plots denote the  $\Gamma$ - $K$  propagation direction.

modes, unlike the hexagonal photonic crystal discussed above, are symmetric at  $\Omega_1$ , and hence can be excited by an incident plane wave. The second intersection of the fourth mode at  $\Omega_1$  in the  $\Gamma$ - $M$  section, near the  $\Gamma$  point, is antisymmetric, and hence cannot be excited by an incident plane wave.

The band index  $n_{\text{eff}}^{\text{d}}$ , plotted in Fig. 2.12b, shows the same band index for  $\Gamma$ - $X$  and  $\Gamma$ - $M$  propagation directions at frequencies just above the band gap. Note again that these index values differ slightly from those reported in Ref. GET00 and are calculated with a different numerical method.

Since the photonic crystal modes at  $\Omega_1$  are both symmetric, one could expect that it would exhibit angle-dependent reflectivity consistent with the Fresnel formulae, including total external reflection (TER). However, the critical angle of a dielectric with refractive index  $n < 0.1$  is less than  $5.7^\circ$ . Yet, as shown in Fig. 2.13, the reflectivities at  $\Omega_1$  are less than one at several angles exceeding the critical angle for both  $\Gamma$ - $X$  and  $\Gamma$ - $M$  orientations. Moreover, TER does not even occur at neighboring frequencies, as the

transmission of a finite slab for light incident at  $45^\circ$  is non-zero, and independent of the slab thickness, as shown in Fig. 2.14. Since changing the slab length shifts frequencies of each transmission peak, they are due to interference, and not TER. As noted in Section 2.3.4, the transmission frequency spacing corresponds to the group refractive index.

While this photonic crystal does not have an effective index consistent with its dynamic reflection properties, Gralak *et al* show that it obeys Snell's law, and hence the kinematic properties are consistent with a dielectric with  $n < 1$ .

## 2.5 Discussion

Quantitatively, refraction and reflection from homogeneous materials are described by kinematic properties (like Snell's law) and dynamic properties (Fresnel formulae). The refractive index plays a critical part in both cases. In the case studies presented above I have analyzed these properties in photonic crystals at (free-space)

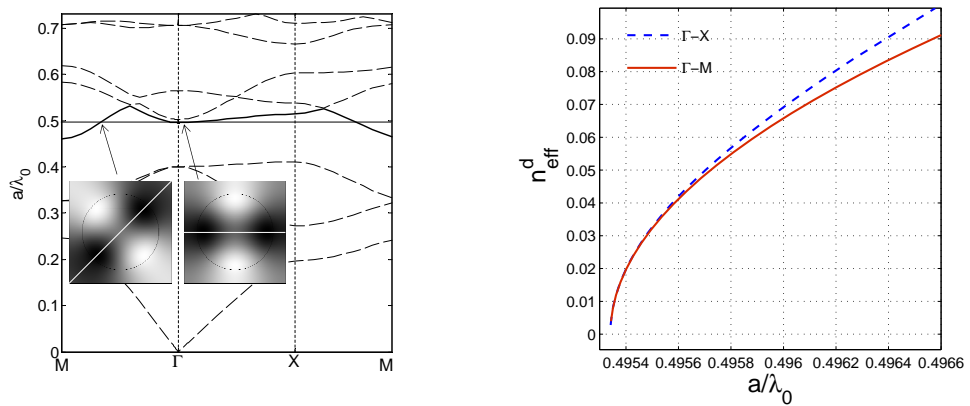


Figure 2.12: (a) Dispersion diagram (TM modes, electric field is parallel to cylinder axis) of a two-dimensional square photonic crystal, unit cell  $a$ , consisting of dielectric cylinders of radius  $r = 0.374a$  and refractive index  $n = 3.0$ . The insets show the electric field of modes with frequency  $\frac{a}{\lambda_0} = 0.496$ . (b) Effective refractive index  $n_{\text{eff}}^d$  above band gap.

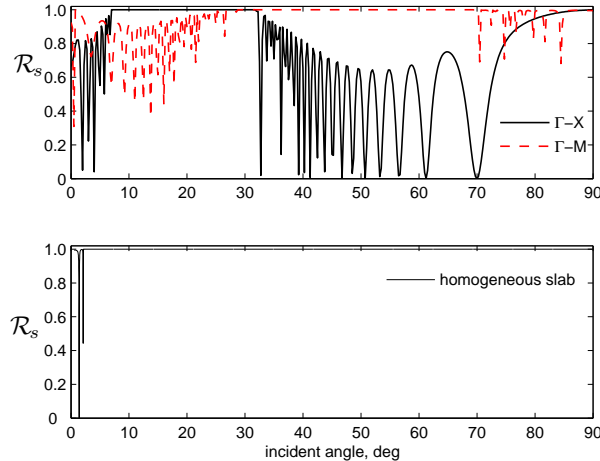


Figure 2.13: Reflectivity of finite-thickness slabs in vacuum. The electric field is parallel to the cylinder axes and normal to the plane of incidence ( $s$ -polarization). Top: A 64-period photonic crystal slab consisting of a square array of cylinders ( $n=3$ ) at normalized frequency  $\frac{a}{\lambda_0} = 0.4956$ . Bottom: A homogeneous dielectric slab with refractive index  $n=0.04$  and the same thickness as the photonic crystal slab.

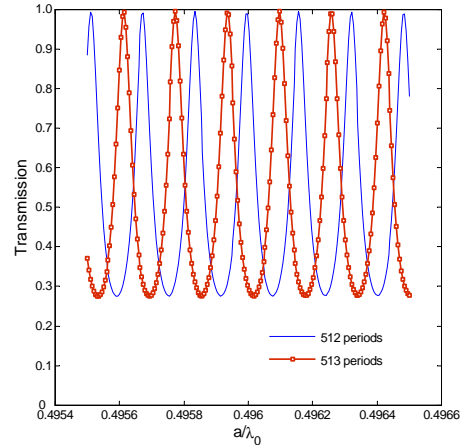


Figure 2.14: 45 degree-incidence transmission through 512 and 513 periods of square photonic crystal described in Fig. 2.12,  $\Gamma$ - $X$  direction. Since the transmission minima depend on the length of the photonic crystal slab, none of them are due to total external reflection occurring at a specific frequency.

wavelengths comparable to the unit cell size. For the silver nanowire photonic crystal, the band index predicts both its kinematic and dynamic optical properties. However, for the dielectric photonic crystal the band index, even if associated with circular equifrequency surfaces, predicts only their kinematic properties provided that plane waves can couple into the mode for which the band index is defined.

The effective index discussed for the dielectric photonic crystals belong to the short-wavelength regime ( $\lambda_0 \gtrsim a$ ). The fields inside the photonic crystals are Bloch waves with a high degree of complexity because they belong to higher bands. They are thus very different from plane waves. Because the Fresnel formulae are derived from the plane-wave solutions to Maxwell's equations, we should not expect them to apply to structures that support Bloch waves, and they cannot be used for impedance matching to photonic crystals unless proven otherwise. Mode symmetry, for example, plays an important role at interfaces between homogeneous materials and photonic crystals. Modes are either symmetric or antisymmetric about the photonic crystal symmetry axis. Consider a plane wave incident on a finite photonic crystal such that

$\mathbf{k}$  is parallel to the symmetry axis of the photonic crystal. Since the incident wave is symmetric about this axis, it will excite only a symmetric mode.<sup>RAM<sup>+</sup>92,Sak01,Par05</sup> If the only mode at this frequency is antisymmetric, all light will be reflected, which would contradict the Fresnel equations if a non-zero  $n_{\text{eff}}^{\text{d}}$  was used.

Nevertheless, in the silver-wire photonic crystal, with wires much smaller than both the unit cell and free-space wavelength, the propagating Bloch modes strongly resemble plane waves (Fig. 2.2). In this case the Fresnel formulae are a good approximation to predict the metamaterial's dynamic optical properties.<sup>Bro53</sup> Since this effective index predicts both its kinematic and dynamic optical properties, it can be used in an effective-medium approach, even though the metamaterial is outside of the long-wavelength limit. This suggests that in the limit of small inclusions, such as thin cylinders, in a host material with the unit cell only slightly smaller than half the free-space wavelength, the modes corresponding to the lowest bands can be excited and associated with an effective index that is consistent with the dynamic properties. This behavior can be observed regardless of the existence of a band gap at higher frequencies.

I have analyzed the dynamic properties of photonic crystals at the interface with a homogeneous material and observed that they cannot always be described in terms of an effective (complex) refractive index. The main implication is that in general, the nature of wave-phenomena generated by photonic crystals cannot be reduced to a description in terms of a single number, i.e. the effective index.

Even if the kinematic properties of a photonic crystal can be predicted by an effective index derived from the band diagram, the effectiveness of any application of the photonic crystal will depend on its dynamic behavior. For example if a device is designed for a specific purpose but no modes can be excited, its utility would be hampered. This should not be understood as a drawback of photonic crystals but rather as a shortcoming of an oversimplified model. In fact, a photonic crystal design could outperform in terms of transmissivity a homogenous material design having the

same band index.

On the other hand, in the cases for which an effective index can describe both the kinematic and dynamic properties, the photonic crystal can be used as a building block for more complicated structures and still be modeled (at least in first approximation) as a homogeneous material.

## **2.6 Conclusions**

I investigated the different definitions of effective refractive index and their limits of applicability. As an example I showed that the reflection and refraction at the interface between air and certain metamaterials are consistent with a unique refractive index. In contrast, the dynamic properties of certain photonic crystals with frequencies near the band edge cannot be simplified to a description in terms of a unique effective refractive index, even though their kinematic properties can.

## Chapter 3

### Imaging properties of negative-effective-index photonic crystal slabs and index-equivalent homogeneous slabs

#### 3.1 Summary

Photonic crystal slabs with a negative refractive index  $n_{\text{eff}}^d$  computed from their band diagram have been shown to have lens-like imaging properties. Here I show that such imaging devices do not create images of the same size or intensity as an equivalent homogeneous slab with refractive index  $n = n_{\text{eff}}^d$ . The incomplete nature of defining an effective refractive index with only the band diagram accounts for these discrepancies.

#### 3.2 Introduction and Methods

In Chapter 2 and Ref. SP05c I considered the refraction and reflection properties of photonic crystals with  $n_{\text{eff}}^d < 1$  and showed that this effective refractive index, predicted by the dispersion curve, was not sufficient to predict its transmission and reflection properties according to the Fresnel formulae. A recent study found similar properties in photonic crystals with negative effective refractive index.<sup>RQX<sup>+</sup>05</sup> This has important consequences for the imaging properties of so-called negative refractive index photonic crystals.

A planar slab of material with a negative refractive index has imaging properties because, like a lens, it refracts diverging rays back toward the optical axis. Current publications on negative refractive index<sup>Smi</sup> often attribute this realization to Vese-

lago,<sup>Ves67, Ves68</sup> though he acknowledges previous work that addresses the subject.<sup>HKBJ03</sup>

Focusing of light with a negative refractive index medium is said to amplify evanescent waves and hence image feature sizes smaller than the diffraction limit.<sup>Pen00, LL03, PLVS03, QTSJ03, ME04, H</sup>

As an extension of previous work,<sup>SP05a, SP05b</sup> I compare the reflectivity  $\mathcal{R}(\theta)$  and imaging properties of a photonic crystal with  $n_{\text{eff}}^{\text{d}} = -1$ , and compare them to that of a homogeneous slab with refractive index  $n = n_{\text{eff}}^{\text{d}}$ . The spot size and intensity for the photonic crystal slab differ from that of its equivalent homogeneous slab with negative refractive index. However, a lens made of the silver-air metamaterial discussed in Chapter 2 performs very similarly to its equivalent homogeneous lens.

I analyze a photonic crystal that has been considered for super-lensing applications:<sup>WRK05, BMS<sup>+</sup>04</sup> a hexagonal array of air-holes ( $2r = 0.8a$ ) in an  $n_{\text{host}} = 3.6$ . At normalized frequency  $\Omega \equiv \frac{a}{\lambda_0} \approx 0.30$ , the equifrequency surface is circular corresponding to an effective refractive index  $n_{\text{eff}}^{\text{d}} = -1$ .<sup>Not00, WRK05</sup>

### 3.3 Results

As in the previous cases shown above, the angle-dependent reflectivity (Fig. 3.1) shows that the photonic crystal does not have the reflectivity of a homogeneous dielectric with the same refractive index. If the photonic crystal had an isotropic effective index, the normal incidence reflectivity would be the same for both the  $\Gamma$ - $K$  and  $\Gamma$ - $M$  orientations. As discussed in Ref. SP05c, the mode symmetries partially explain this difference. For the  $\Gamma$ - $K$  orientation,  $\mathcal{R} = 1$ , because the mode is antisymmetric, and hence cannot couple an incident plane wave.

Imaging with an  $n_{\text{eff}}^{\text{d}} = -1.0$  slab can illustrate how this photonic crystal's band index defined by its circular equifrequency surface agrees with Snell's law, but not the Fresnel formulae. Here I compare the imaging of a point source with photonic crystal slabs of negative band index with the image location and intensity to homogeneous slabs of refractive index equal to the photonic crystal's band index ( $n_{\text{eff}}^{\text{d}} = -1.0$  at  $\frac{a}{\lambda_0}$

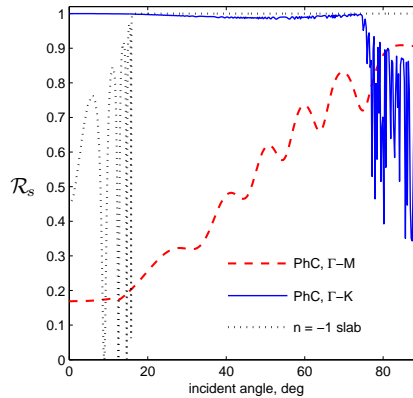


Figure 3.1: Reflectivity of finite-thickness slabs in a surrounding medium of refractive index  $n = 3.6$ . The electric field is parallel to the cylinder axes. The photonic crystal is an 8-period photonic crystal slab consisting of a hexagonal array air-cylinders in a dielectric ( $n_{\text{host}} = 3.6$ , ( $2r = 0.8a$ )) at normalized frequency  $\frac{a}{\lambda_0} = 0.301$ , where  $n_{\text{eff}}^d = -1.0$ .

$= 0.301$ ). I used a finite-element solver<sup>Com04</sup> to find image locations and intensities for for  $21 \times 8$  unit cell slabs illuminated by a Gaussian source ( $2W = \frac{2\lambda_0}{3}$ ) at different distances from the slab, an example of which is shown in Fig. 3.2.

Figure 3.3 compares the imaging properties of the photonic crystal slab and its equivalent homogeneous slab. Interestingly, as shown by the ray optics prediction (dotted line) in Fig. 3.3(a), and noted in Ref. LL03, the distance between the object and the image is invariant with the position of the negative-index slab along the optic axis. A simple ray trace shows this distance to be  $d_T = d_{\text{slab}}(1 - \frac{n_1}{n_{\text{slab}}})$ , where  $n_1$  is the refractive index of the ambient medium and  $d_{\text{slab}}$  and  $n_{\text{slab}}$  are the slab thickness and refractive index respectively. For small object distances  $d_o$ , numerical simulations of both the photonic crystal and homogeneous slab show this trend. As  $d_o$  increases, the image ap-

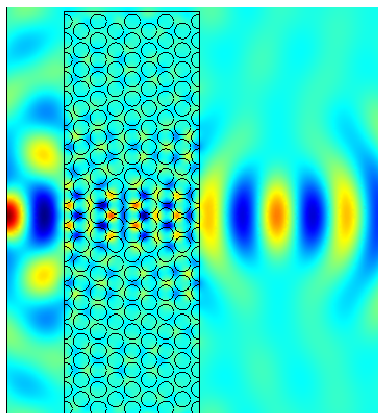


Figure 3.2: Imaging of a Gaussian source ( $\frac{a}{\lambda_0} = 0.301$ ,  $2W = \frac{2\lambda_0}{3}$ ) by the photonic crystal described in Fig. 3.1 oriented in the  $\Gamma$ - $M$  direction. Electric field is parallel to the axis of the cylindrical holes.

proaches the slab's exit plane and the overlap between the intensity maxima inside and outside the slab (shown in Fig. 3.2) increases, hence distorting the image location. This effect is larger for the photonic crystal because, as shown in Fig. 3.3(d), the photonic crystal slab has a larger point spread function than its equivalent homogeneous slab.

Yet, this effect does not fully explain the differences in image locations between the photonic crystal and equivalent homogeneous slab. Even without the overlap effect, we should not expect the photonic crystal slab to produce an image at the same location as its equivalent homogeneous slab because their angular-dependent reflectivity differ (Fig. 3.1). Hence, the intensity distribution at the slab-air interface in the photonic crystal slab differs from that of the homogeneous slab, which in turn results in different intensity maxima locations.

Further, Fig. 3.3(c) and Fig. 3.3(d) shows the corresponding peak intensities

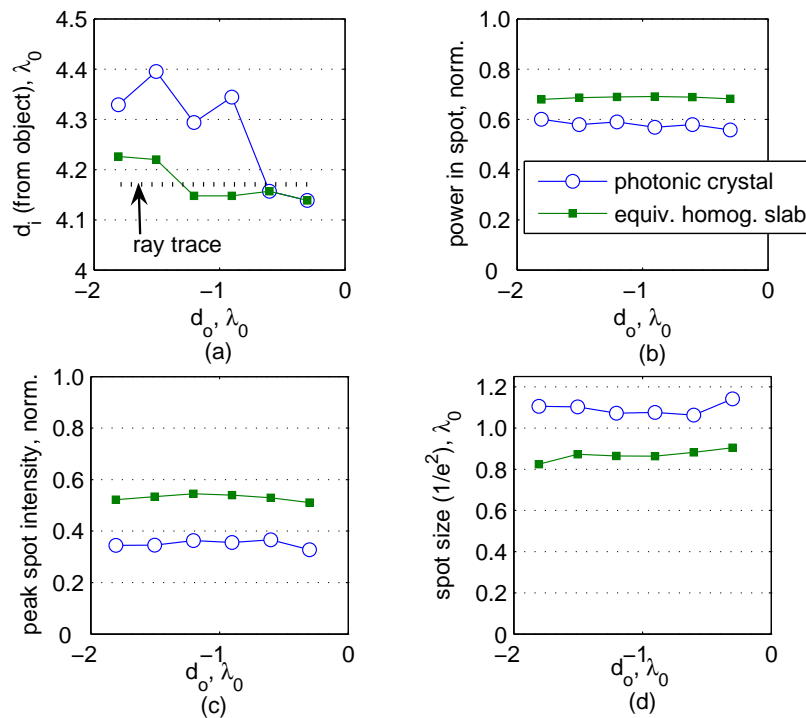


Figure 3.3: Comparison of imaging of a Gaussian source ( $\frac{a}{\lambda_0} = 0.301$ ,  $2W = \frac{2\lambda_0}{3}$ ) by a photonic crystal slab, described in Fig. 3.1, with  $n_{\text{eff}}^d = -1$  and a homogeneous slab with index  $n = -1$ . (a) Image distance as a function of object distance, (b) Power in Gaussian spot, (c) Peak intensity, (d) FWHM Spot size. The homogeneous ( $n = -1$ ) slab imaging system is lossy because of its finite width. The object distance  $d_o$  is the distance between the object and the slab interface closer to the object. The image distance  $d_i$  is the distance between the object and the image.

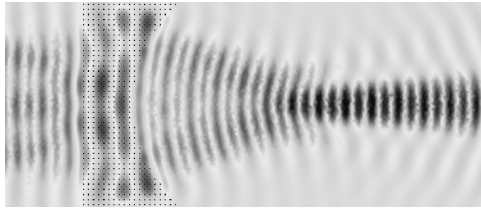


Figure 3.4: Finite-element simulation of  $\lambda_0 = 1 \mu\text{m}$  light incident on a plano-concave ULIM lens ( $n_{\text{eff}} = 0.61 + 0.022i$ ) with a radius of curvature  $R=5 \mu\text{m}$ .

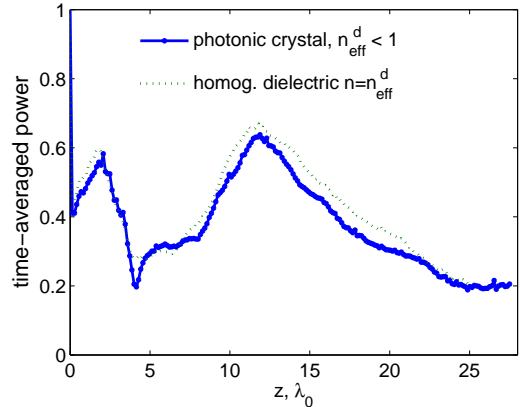


Figure 3.5: On-axis power of plane wave focused by a ULIM lens, described in Fig. 3.4, and a homogeneous lens with refractive index  $n = n_{\text{eff}}$ .

and spot sizes do not match, which is consistent with previous research on photonic crystal coupling efficiency.<sup>QTSJ03</sup> Note also that the image of the subwavelength object produced by the homogeneous negative-index slab has a  $\frac{1}{\epsilon^2}$  spot width smaller than the free-space wavelength. Yet, the photonic crystal with  $n_{\text{eff}}^{\text{d}} = -1.0$  does not achieve such subwavelength imaging.

The difference in the angle-dependent reflectivity of photonic crystal and homogeneous slab (Fig. 3.1) explains the different spot sizes and shapes. The differences between the photonic crystal slab and its equivalent homogeneous slab decrease as the Gaussian beam width increases, as wider sources have narrower angular spectra.

In previous publications,<sup>SP03,SP04a</sup> I showed that a metamaterial composed of silver wires embedded in air can have an effective refractive index less than the one at optical wavelengths. In this case, the wavelength was much larger than the wire width, but only slightly longer than twice the unit cell length. Unlike the dielectric photonic crystals considered above, the propagating modes in the ultralow index metamaterial (ULIM) resemble plane waves, and the effective refractive index, when used with the Fresnel formulae, accurately predicted the metamaterial's angle-dependent reflectivity.<sup>SP05c</sup>

To demonstrate that this photonic crystal has both the refraction and reflection properties of its equivalent-index homogeneous material, I model a focusing lens. A

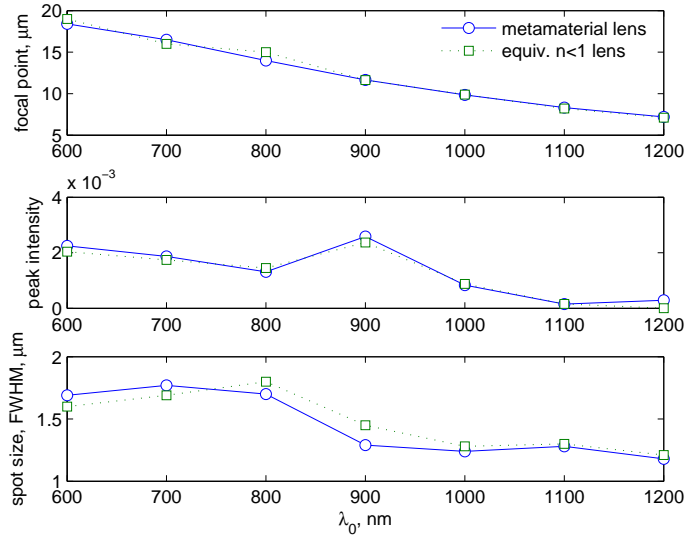


Figure 3.6: Comparison of imaging by a metamaterial lens, described in Fig. 3.4, with a lens made of a homogeneous dielectric with the same refractive index.

beam incident on a planar interface between air and a ULIM is refracted away from the normal, as opposed to refracting toward the normal as it would with most optical materials. If one were to build a plano-concave lens with a ULIM, the result would be a converging device, as shown in Fig. 3.4. Figures 3.5 and 3.6 show that both the location and intensity of the beam focused by the metamaterial lens agrees with that of the equivalent lens made of a homogeneous dielectric with refractive index  $n = n_{\text{eff}}^{\text{d}}$ .

While  $n_{\text{eff}}^{\text{d}}$  predicts reflection and transmission properties consistent with the Fresnel formulae for photonic crystals with thin inclusions, it does not for the dielectric photonic crystals considered here. A sufficient condition for the Fresnel formulae to hold is that the photonic crystal mode must resemble a plane wave, as these are assumed in the derivation of the Fresnel formulae. This can occur in two situations: when the wavelength is much longer than the unit cell or when the inclusions in a host material are much smaller than the wavelength, even if the unit cell is not.

### 3.4 Conclusion

The effective refractive index of a photonic crystal with  $n_{\text{eff}}^{\text{d}} < 0$  defined by its dispersion diagram does not necessarily predict its reflectivity and transmissivity at

an interface with a homogeneous material. While its imaging properties are similar to that of a homogeneous slab with a negative refractive index, they are not the same. In the imaging example shown here, a hypothetical homogeneous negative index slab exhibits subwavelength imaging while a photonic crystal with the same band index does not. Thus such a photonic crystal cannot be considered as completely equivalent to a homogeneous material with an effective refractive index.

## Chapter 4

### Ultralow Index Metamaterials\*

#### 4.1 Summary

Metamaterials composed of metal-dielectric nano-structures are engineered to have an effective refractive index less than unity at optical wavelengths. The effect of total external reflection is demonstrated when light is incident from vacuum onto these materials at an angle exceeding the critical angle defined by Snell's Law. Novel approaches are discussed to derive the effective index of refraction from the reflection and refraction properties of finite slabs. The effect of losses and dispersion are analyzed in the visible range of frequencies considering the measured properties of silver. The differences among ultra-low refractive index metamaterials, photonic band gap materials, and metals are discussed. Remarkably, a band gap is not required in order to obtain total external reflection.

#### 4.2 Introduction

There has been a growing interest in the optical properties of micro- and nano-structured materials because of their ability to control light in unconventional ways. Research on photonic crystals has been focused at engineering band gaps for a variety of applications.<sup>JMW95</sup> Lately, several groups have reported novel physical properties of metamaterials presenting simultaneous negative permittivity and permeabil-

---

\* A version of chapter was originally published as Ref. SP03

ity .<sup>SSS01, Pen00, VWV02, GNV02a, GNV02b</sup> However, the implementation of these so-called negative-index materials in the optical regime is still a challenging task.

As discussed in Section 1 and Ref. SP02, the absolute value of the index contrast is also important. Current nano-fabrication techniques can generate feature sizes much smaller than visible wavelengths, thus enabling the fabrication of these metamaterials in the optical regime. However, in this regime the limitations of nanofabrication and the scaling of physical properties of metals and dielectrics require special attention.

In this chapter I propose the use of metamaterials with real part of the effective index less than unity ( $0 \leq \text{Re}\{n_{\text{eff}}\} \leq 1$ ) as a building block for photonic applications.<sup>SP02</sup> First I discuss basic phenomena and the feasibility of metal-dielectric structures with  $0 \leq \text{Re}\{n_{\text{eff}}\} \leq 1$  using approximate analytical models. I then study the refraction and reflection properties of finite slabs of the metamaterial using numerical models and show that total external reflection (TER) from air is possible with simple structures. Finally, I discuss the effects of losses and dispersion and compare these metamaterials with photonic band gap materials and bulk metals.

### 4.3 Background research and its relation to ULIM

The analysis of artificial composite materials has been carried out under several different frameworks such as transmission line models,<sup>Bro60</sup> effective medium theory,<sup>Asp82</sup> homogenization,<sup>FB97</sup> and photonic crystals.<sup>JMW95</sup> As long as fifty years ago it was recognized that artificial dielectrics can have an effective index of refraction below unity.<sup>Bro53</sup> Investigations have shown its potential application in the design of antennae.<sup>Bro60, Gup71, ETS+02</sup> Recent investigations have also shown the potential of zero permittivity materials as band gap structures.<sup>GPX02</sup> This is a limiting case of the ULIMs when losses are neglected ( $\epsilon_{\text{eff}} = 0$  leads to  $n_{\text{eff}} = 0$ ). Low permittivity materials are related to what is known in electromagnetics as high-impedance surfaces.<sup>Sie99</sup>

It should be noted, however, that these investigations do not provide a proper

analysis of the behavior of ULIMs in the visible regime. At these frequencies metal losses and dispersion become critical and cannot be neglected. In addition, features much smaller than the wavelength are hard to fabricate and thus, in general, the long-wavelength approximation does not hold.

The goal of this chapter is to analyze the reflection and transmission properties of ULIMs at optical frequencies. In particular, I investigate for the first time the effect of total external reflection (TER) as defined by a critical angle in Snell's law.

Total *internal* reflection is a very well known optical effect and is the basis of various technologies such as index waveguides, polarizing devices, and near-field microscopes. Similarly, total *external* reflection (TER) occurs when light propagating in vacuum is incident on a medium with a refractive index less than unity at an angle exceeding the critical angle defined by Snell's Law. This effect is very well known for x-rays incident on planar interfaces at grazing angles.<sup>Att99</sup> In the x-ray regime, the index of refraction is expressed in the form  $n = 1 - \delta + i\beta$  where, typically,  $\delta \approx 10^{-5}$  and  $\beta \approx 10^{-7}$ . For angles exceeding the critical angle, as defined for the lossless case, the refracted waves are inhomogeneous, the refracted angle is very close to  $\frac{\pi}{2}$ , and the reflectivity is very close to unity.<sup>Att99</sup> Here, in contrast, I describe metamaterials exhibiting total external reflection at visible wavelengths. The real part of the refractive index is well below unity ( $0 < \delta \leq 1$ ) while the loss component is small compared to bulk metals ( $\beta \ll 1$ ).

#### 4.4 Theory

Effective medium theories allow the characterization of the electromagnetic properties of composite materials when the wavelength is much larger than the unit cell in periodic composites or the scale of the particles in disordered composites. The properties depend on the host permittivity, the guest permittivity, the volume fraction, the frequency, and the morphology of the composite material. When all other variables are

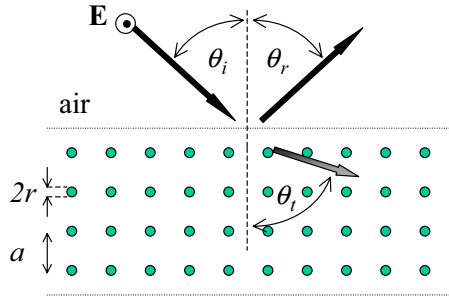


Figure 4.1: Refraction and reflection at the interface of air and a two-dimensional metamaterial with ultralow effective refractive index. Light is refracted off the normal to the surface and the refracted waves are inhomogeneous. In a specific design the metamaterial is composed of a square array of cylindrical wires and the incident light is polarized parallel to the wires.

given, changes in the morphology allow for a wide range of values in the permittivity and permeability.<sup>Asp82</sup>

To demonstrate the design of ULIMs, I have chosen a simple structure consisting of an array of metallic cylindrical wires embedded in air. Above the cutoff frequency of the structure the metamaterial behaves like a homogeneous material with permittivity below unity. These metamaterials are lossy so their refractive index is in fact complex, the real part satisfying  $0 \leq \text{Re}\{n_{\text{eff}}\} \leq 1$ . I used an approximate analytic model as a starting point in the design of a structure with  $0 \leq \text{Re}\{n_{\text{eff}}\} \leq 1$  at  $\lambda = 0.5 \mu\text{m}$  for light polarized parallel to the wires (and thus propagating normal to the wire axes) (Fig. 6.1). The model provides an effective relative dielectric constant  $\epsilon_{r\perp}(\omega)$  as a function of frequency  $\omega$  according to the expression

$$\epsilon_r = 1 - \frac{\omega_p^2}{\omega(\omega + i\gamma)}. \quad (4.1)$$

where  $\omega_p$  is the analogue of the plasma frequency and  $\gamma$  a damping frequency. These parameters depend on the unit cell geometry and the conductivity of the metal  $\sigma(\omega)$  and can be calculated as  $\omega_p^2 = \frac{2\pi c_0^2}{a^2 \ln(\frac{a}{r})}$  and  $\gamma = \frac{\epsilon_0 a^2 \omega_p^2}{\pi r^2 \sigma}$ ,<sup>PHRS98</sup> where  $a$  is the period,  $r$  the radius, and  $c_0$  is the speed of light in vacuum, and are valid for  $r \ll a$ . The expression for complex frequency-dependent conductivity is  $\sigma = \frac{\epsilon_0 (\omega_p^{Ag})^2}{(\gamma^{Ag} - i\omega)}$ ,<sup>RMC93</sup> where  $\omega_p^{Ag}$  and  $\gamma^{Ag}$  are the plasma frequency and electron collision frequency of silver. I obtained these parameters by fitting the Drude model to measured refractive index values in the

frequency range of interest (Fig. 4.2).

This type of model can be interpreted in terms of conventional electrodynamics and can be derived in several ways, including transmission line models and homogenization theory.<sup>PE02,WVV01,Rot62,FB97</sup> It has also shown fair agreement with numerical and experimental results.<sup>PHRS98</sup> Although approximate, this model takes into account the effects of polarization, dispersion, losses, and geometry of the metamaterial.

Hence, I first used Eq. (4.1) as a guide to find the geometry of a wire array with  $0 < \text{Re}\{\epsilon_{r\perp}\} < 1$  at  $\lambda = 0.5 \mu\text{m}$ , and then I studied the optical properties using numerical models. For silver wires of radius  $r = 15 \text{ nm}$  in a square lattice with  $a = 200 \text{ nm}$  unit cells, the effective resonance wavelength is  $\lambda_p = 0.8 \mu\text{m}$ , and the effective (relative) dielectric constant  $\epsilon_{\text{eff}}$  is between zero and one at slightly shorter wavelengths (Fig. 4.3). I considered these predictions to be approximate because the unit cell length is just less than half the minimum operating wavelength. Note that this structure also has an effective permeability that in general is different from unity,<sup>Bro60</sup> thus affecting the effective index.

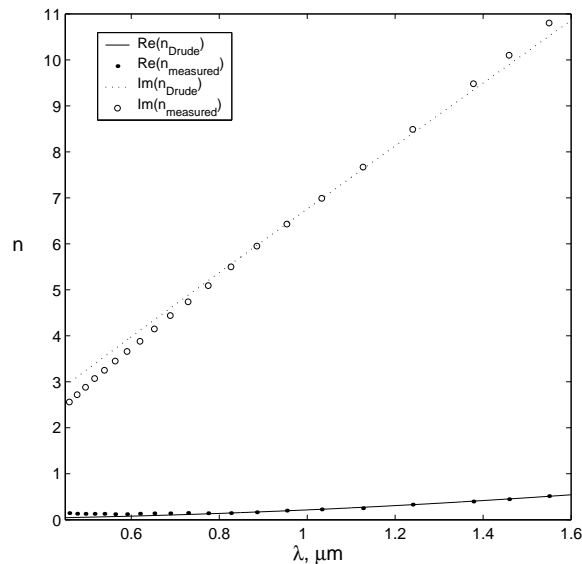


Figure 4.2: Experimental values<sup>LH91</sup> and best-fit Drude model predictions ( $\nu_p^{Ag} = 1174.8 \text{ THz}$ ,  $\gamma^{Ag} = 205.2 \text{ THz}$ ) for the refractive index of silver for wavelengths between  $0.45 \mu\text{m}$  and  $1.6 \mu\text{m}$ .

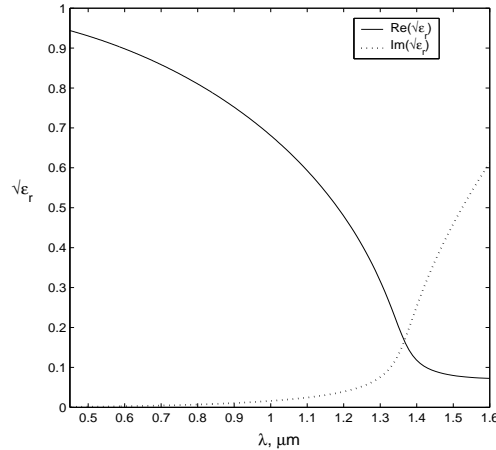


Figure 4.3: Square root of the effective relative dielectric constant (Eq. (4.1)) of silver-air metamaterial as a function of free-space wavelength. Wire radius:  $r = 15$  nm, unit cell size:  $a = 200$  nm.

## 4.5 Dispersion diagram

The calculated dispersion curves for the first few modes of the specified wire array composed of perfect conductors, are shown in Fig. 4.4. The calculations were performed by a finite-element Maxwell's Equation solver.<sup>Ans01</sup> The difference between the left ( $\Gamma - X$ ) and right-hand ( $M - \Gamma$ ) sides of the dispersion curve shows that the metamaterial is anisotropic. This anisotropy disappears in the long-wavelength limit. Figure 4.4 shows that the lowest frequency mode is above the light line, which suggests that the wire array has an effective refractive index  $n_{\text{eff}} = \frac{ck}{\omega}$  less than unity in agreement with the analytical model. For the design frequency (600 THz) there is only one propagating mode, a necessary condition to assign a well-defined refractive index to a metamaterial. Also note the absence of a band gap in the region of interest, which differentiates the nature of the ultralow refractive index discussed here from other related effects that require a band gap.<sup>Not00</sup>

An approximate effective index could be obtained from the phase velocity of the propagating mode  $v = \omega/k$  inside the infinitely periodic structure. However, such an effective index is not accurate because the model does not account for the finiteness of real structures.<sup>SSMS02,AAD00</sup> In effect, evanescent modes at the boundaries of finite structures ensure field continuity at interfaces. Since  $\frac{a}{\lambda} \lesssim \frac{1}{2}$ , these modes are more

significant than in structures with smaller  $\frac{a}{\lambda}$  values, so neglecting this effect can lead to inaccuracies in the predicted effective index.

#### 4.6 Refraction at a planar interface and calculation of the effective index

Both the analytic model and the dispersion curves provide only an approximate qualitative prediction for the refractive index (see Fig. 4.3). Calculating an accurate effective refractive index requires numerical techniques that account for losses and the finite character of real structures. Hence, I calculated the refracted fields when a plane wave is incident normal to a planar air-metamaterial interface. The refracted waves are inhomogeneous because of the metal losses, which correspond to a complex refractive index. For the metamaterial to have an effective index less than one, it must properly refract light. That is, light must propagate inside the metamaterial the same way it would in a transparent homogeneous material with  $Re\{n\} < 1$ , should one exist.

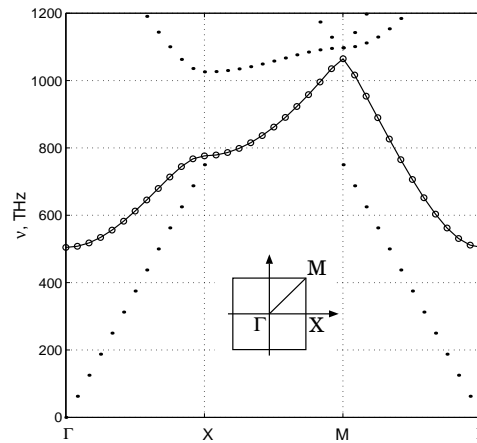


Figure 4.4: Dispersion diagram of a two-dimensional square array of silver wires. The wires have radius  $r = 15$  nm and are spaced 200 nm apart. The two straight lines are the dispersion curves of light in free-space.

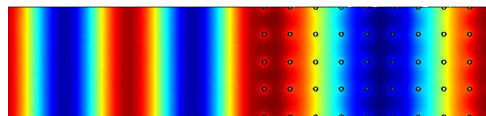


Figure 4.5: Electric field magnitude (parallel to the wires) of  $\lambda_0 = 1.0 \mu\text{m}$  light normally incident on silver-air metamaterial.

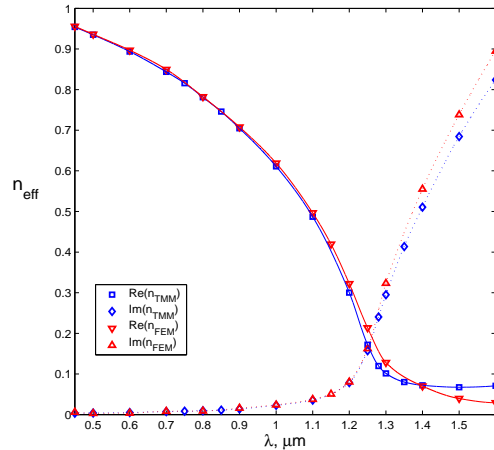


Figure 4.6: Refractive index (real and imaginary parts) of the metamaterial as a function of free-space wavelength as predicted by its normal incidence refraction (FEM) and angle dependent reflectivity (TMM). Wire radius:  $r = 15$  nm, unit cell size:  $a = 200$  nm.

I used a finite-element Maxwell's equations solver<sup>Com04</sup> to compute the fields refracted by the metamaterial, as shown in Fig. 4.5. To determine the metamaterial's effective index at each wavelength, I used a minimization algorithm to find the refractive index of a homogeneous material that transmits the same electric field as the metamaterial (inhomogeneous plane wave with the same complex propagation constant). The algorithm required an initial guess for the complex refractive index, and the resulting effective index values are insensitive to these guesses to four decimal places. This method for calculating  $n_{\text{eff}}$  differs from previous methods,<sup>Bro60, SSMS02, GMTV98</sup> which rely on the reflection coefficients and present ambiguity in the phase of the reflected wave.

Accurate modeling of metamaterials in the optical regime requires consideration of losses and materials dispersion. In our simulations I used interpolated values of the refractive index of silver, shown in Figure 4.2.

Figure 4.6 shows the calculated effective index confirming that indices with real part below unity are feasible at optical frequencies. Although the general behavior coincides with the predictions of the analytical models (Fig. 4.3), the numerical model predicts different effective plasma wavelengths. This occurs in part because the accuracy of the analytical model requires  $\lambda \gg a$ . The metamaterial's fairly low loss ( $\text{Im}(n_{\text{eff}}) \ll 1$ ) is a promising property for practical purposes.

## 4.7 Reflection at a planar interface

ULIMs have interesting reflection properties because the real part of the index is lower than the index of air. Therefore, Snell's law predicts a critical angle above which total reflection occurs. I studied numerically TER for slabs of ULIMs and used the reflectivity at all angles to calculate the effective index, which was compared with the results obtained by refraction (Sec. 4.6).

The transfer matrix method (TMM)<sup>BPMW95,Rey00b</sup> was used to find the reflectivity  $\mathcal{R}_{TE}$  and transmissivity  $\mathcal{T}_{TE}$  of ULIM slabs of different thicknesses at  $\lambda_0 = 0.5 \mu\text{m}$ . Figures 4.7 and 4.8 show the reflection and transmission properties of slabs containing 1 to 128 periods of the array and a comparison to equivalent homogeneous slabs with the same thickness and index. The thickness of the equivalent slab was determined as the number of layers multiplied by the unit cell width. The interface plane was chosen at a distance equal to half unit cell width before the first wire row (Fig. 6.1). A  $30 \times 30$  grid was used in the TMM to properly sample the two-dimensional unit cell. This was verified by increasing the sampling to a  $60 \times 60$  grid and obtaining the same effective index as discussed below. The dielectric constant of silver was obtained from experimental data as before (Fig. 4.2).

The structure behaves like a lossy dielectric with a refractive index less than unity for light polarized normal to the incident plane (TE) and parallel to the wires. At small incident angles there is little reflection, while at larger angles the structure abruptly becomes reflective. The reflectivity of a dielectric slab with an index of  $n = 0.935 + 0.0038i$  fits the reflectivity of the wire arrays with four or more periods. The critical angle, defined here as the inflection point of  $\mathcal{R}_{TE}$ , is 68 degrees, which agrees with the critical angle defined by Snell's law.

Due to absorption, the transition to high reflection is not as abrupt as with total internal reflection from transparent dielectrics, much like the known TER of x-

rays. Note that with only four rows of wires, there is a critical angle above which, loss notwithstanding, total external reflection occurs. As a consequence, just a few periods may suffice for practical applications of this effect, easing the fabrication. The effective index properly describes the behavior of the slab even for the case of two layers of wires, a property that could not have been predicted with the long wavelength approximation. Also note that  $\mathcal{R}_{TE} + \mathcal{T}_{TE} < 1$  because of losses.

Hence, the reflection data can be used as an alternative method to calculate the refractive index. I calculated the complex refractive index of a homogeneous dielectric slab whose reflectivity best matches that of the finite wire array at all incident angles for polarization normal to the incident plane (TE) and parallel to the wires. That is, I determined the effective index by comparing the reflectivity of the metamaterial with that of a homogeneous material as predicted by the Fresnel formulae. This method also differs from those using only a single angle incidence reflection and transmission coefficients<sup>Bro60,SSMS02</sup> and should give a more reliable value that is appropriate for all incident angles despite the slight anisotropy due to a relative large unit cell. The results are summarized in Fig. 4.6 and show a striking agreement with the effective

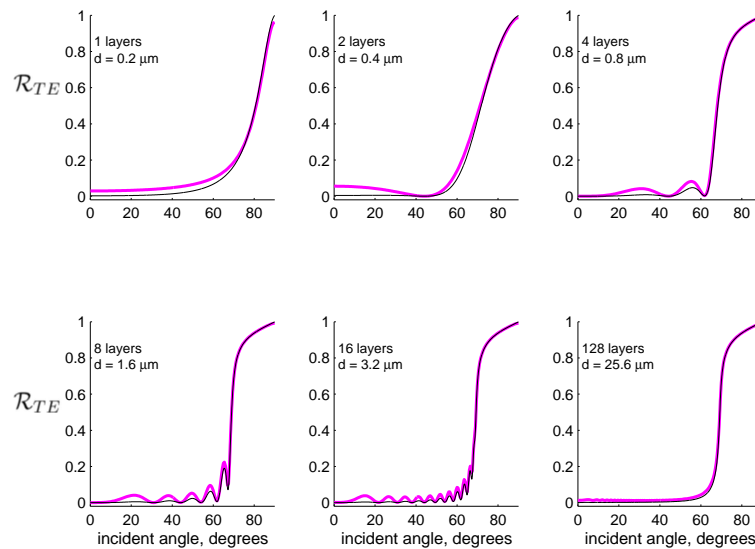


Figure 4.7: Total external reflection: reflectivity at  $\lambda_0=0.5 \mu\text{m}$  as a function of incident angle. Thick curve: transfer matrix method predictions for silver wire metamaterials. Thin curve: analytical calculations based on Fresnel formulae for homogeneous  $n = 0.935 + 0.0038i$  slabs of the same thickness as the metamaterial. Wire radius:  $r = 15 \text{ nm}$ , unit cell size:  $a=200 \text{ nm}$ , homogeneous slab thickness  $d$ .

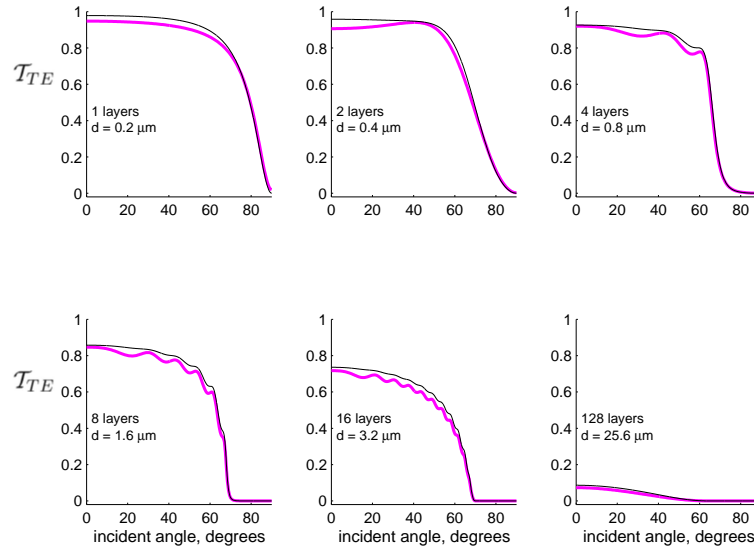


Figure 4.8: Transmission at  $\lambda_0 = 0.5 \mu\text{m}$  as a function of incident angle. Thick curve: transfer matrix method predictions for silver wire metamaterials. Thin curve: analytical calculations based on Fresnel formulae for homogeneous  $n = 0.935 + 0.0038i$  slabs of the same thickness as the metamaterial. Wire radius:  $r = 15 \text{ nm}$ , unit cell size:  $a = 200 \text{ nm}$ , homogeneous slab thickness  $d$ .

index obtained with refraction (Sec. 4.6).

## 4.8 Discussion

The designed ULIM behaves on refraction, reflection, and transmission as a low-loss dielectric with  $0 \leq \text{Re}\{n_{\text{eff}}\} \leq 1$  for wavelengths between roughly  $0.45 \mu\text{m}$  and  $1.2 \mu\text{m}$ , as shown in Fig. 4.6. The reflectivity at shorter wavelengths ceases to resemble total external reflection because  $\lambda$  approaches  $2a$ . At longer wavelengths, loss dominates as  $\text{Re}(n_{\text{eff}})$  decreases, and the reflectivity resembles that of a high-loss dielectric. Note that even though the metamaterial is lossy and dispersive, for a proper design the attenuation of waves propagating in the metamaterial is much lower than in metals at optical frequencies. While in metals at optical wavelengths the imaginary part of the refractive index dominates, in the metamaterial it can be more than two orders of magnitude smaller than the real part. Note that the use of real parameters for the composing materials (including losses and dispersion) is critical to achieve an accurate picture because optical properties of metals do not scale with frequency.

The recently proposed zero-permittivity materials ( $\epsilon_{\text{eff}} = 0$ ) as band gap struc-

tures<sup>GPX02</sup> can be considered a limiting case of the ULIMs presented here ( $0 \leq \text{Re}\{n_{\text{eff}}\} \leq 1$ ). However, they do not show the effect of TER defined by a critical angle different from zero. Moreover, our calculations indicate that losses produced by real metals should play a critical role at optical frequencies in the  $\epsilon \rightarrow 0$  limit, suggesting that in this limiting case, further investigation is required.

Note that dielectric photonic band gap materials can also refract light incident in vacuum away from the surface when working close to the band gap. Thus one could assign them a refractive index less than unity and even less than zero that will be consistent with Snell's law.<sup>Not00</sup> However, this effect differs from the reflection from ULIM: a) the photonic band gap materials do not in principle have the same angle-dependent reflectivity and transmissivity predicted by Fresnel formulae,<sup>1</sup> . b) their unusual values of refractive index only apply for narrow bandwidths, and c) they require a band gap.

#### 4.9 Conclusions

I have analyzed optical metamaterials with  $0 \leq \text{Re}\{n_{\text{eff}}\} \leq 1$  at optical frequencies using approximate analytical models, accurate numerical models, and experimentally-determined metal optical constants to provide an accurate picture of the effect of losses and dispersion. Methods for determining a realistic effective index based on reflected and refracted fields were implemented. To the best of the authors' knowledge, this is the first time a metamaterial is shown to exhibit total external reflection at optical visible wavelengths. No band gap is required to observe this effect. Such flexibility in the specification of the effective properties of a material opens up new opportunities for device applications.

---

<sup>1</sup> This is the subject of Chapter 2

## Chapter 5

### Waveguiding in air by total external reflection from ultra-low index metamaterials\*

#### 5.1 Summary

Metamaterials composed of metal-dielectric nano-structures can be engineered to have the real part of the effective refractive index less than unity at optical wavelengths, and hence exhibit total external reflection. This chapter demonstrates how to utilize this effect to design and analyze slab waveguide structures that guide visible light in an air core.

#### 5.2 Introduction

Optical micro- and nano-structured materials are intriguing because of their ability to control light in unconventional ways. For example, photonic crystals<sup>JMW95</sup> and metamaterials<sup>Pen03</sup> have novel physical properties with potential application in photonic integration.

Lately, several groups have reported novel physical properties of metamaterials presenting simultaneous negative permittivity and permeability, and hence a negative effective refractive index.<sup>SSS01, Pen03</sup> Waveguides composed of these metamaterials have been studied in the microwave region.<sup>NT02, CCI01</sup> In these and similar studies,<sup>HEO03, PB03</sup> the metamaterial fills the waveguide core and is assumed to be lossless and homogeneous.

---

\* A version of this chapter was originally published as Ref. SP04a.

Here I focus on the use of metamaterials with  $0 \leq \text{Re}(n_{\text{eff}}) \leq 1$  for the cladding of an air-core waveguide operating at visible wavelengths. I also account for the effects of losses, dispersion, and the metamaterial's inherent inhomogeneities.

In Chapter 4 I proposed the use of ultra-low refractive-index metamaterials (ULIM) with real part of the effective index less than unity as a building block for photonic applications.<sup>SP03</sup> The demonstrated metamaterial was a two-dimensional square array of cylindrical silver wires embedded in an air host medium. The designed ULIM behaved on refraction, reflection, and transmission as a low-loss dielectric with  $0 \leq \text{Re}(n_{\text{eff}}) \leq 1$  for wavelengths between  $0.45 \mu\text{m}$  and  $1.2 \mu\text{m}$  for light polarized parallel to the wires. (See Fig. 6.1.) I determined the effective refractive index from refraction and reflection calculations using Fresnel formulae and discussed the effect of total external reflection from finite slabs of the metamaterial using numerical models. Here, I study for the first time the possibility of guiding light in an air core by the effect of TER from ULIMs.

### 5.3 Methods

Waveguide design with ULIMs benefits from their additional degrees of freedom available for index specification. In particular, one advantage of using ULIMs is the possibility of designing a waveguide with a lossless and dispersionless core such as air or vacuum. Nevertheless, such a waveguide will still have a lossy and dispersive cladding. In what follows I show how to design a single mode slab waveguide with ULIM cladding and minimum loss at  $\lambda_0 = 0.5 \mu\text{m}$ .

I used the transfer-matrix method (TMM)<sup>BPMW95, Rey00b, SP03</sup> to calculate the effective refractive index  $n_{\text{eff}}(\lambda_0)$  of metamaterials of different unit cells as a function of silver fill factor. In this Letter, I use wires with square cross-sections instead of cylindrical wires, as square wires allow for more efficient numerical modeling. Figure 5.1 shows the effective refractive index as a function of wire width  $b$  for a square array with unit cell  $a=200 \text{ nm}$ .

For each of these  $n_{\text{eff}}$  values, I used both analytical<sup>Rei73</sup> and numerical<sup>Com04</sup> models to calculate the complex propagation constant  $\beta$  for a single-mode slab waveguide with a core index  $n_{\text{co}} = 1$  and homogeneous cladding of  $n_{\text{cl}} = n_{\text{eff}}$ . To ensure low-loss single-mode operation, the core width of each waveguide was 95% of the single-mode cutoff,  $d_{\text{co}} = \frac{\lambda_0}{2NA}$ , where  $NA = \sqrt{n_{\text{co}}^2 - \text{Re}(n_{\text{cl}}^2)}$  is the numerical aperture.

## 5.4 Results

Figure 5.2 shows the  $\frac{1}{e}$  power attenuation distance  $z_c = \frac{1}{2\text{Im}(\beta)}$ , corresponding to the  $n_{\text{eff}}$  values in Fig. 5.1. The dotted curves show the loss of waveguides with homo-

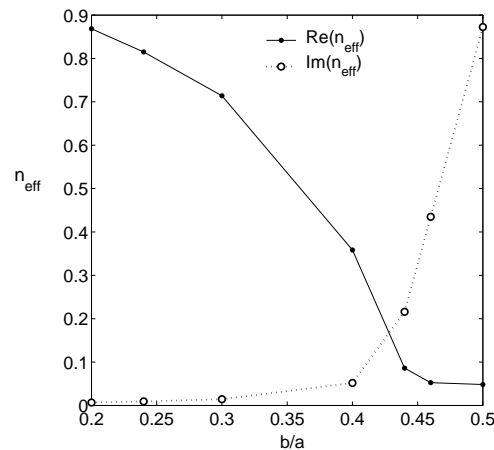


Figure 5.1: Refractive index (real and imaginary parts) of the metamaterial as a function of wire width  $b$  as predicted by its angle-dependent reflectivity. Unit cell size:  $a = 200$  nm,  $\lambda_0 = 0.5$   $\mu\text{m}$ .

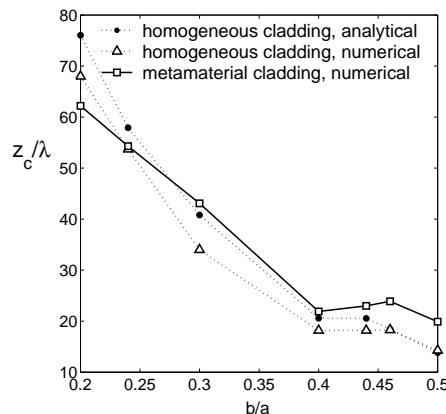


Figure 5.2: Power attenuation ( $\frac{1}{e}$ ) at  $\lambda_0 = 0.5$   $\mu\text{m}$  in single mode slab waveguides with a homogeneous ultra-low index cladding corresponding to the predicted  $n_{\text{eff}}$  in Fig. 5.1, and with metamaterial cladding (Unit cell size:  $a = 200$  nm, wire width  $b$ ).

geneous claddings calculated both analytically and numerically. To find the loss of the ULIM waveguide (the solid curve in Fig. 5.2), I replaced the hypothetical homogeneous  $0 \leq \text{Re}(n_{\text{eff}}) \leq 1$  dielectric claddings with their corresponding silver-air ULIMs. The excitation electric field for the numerically modeled waveguides was the single-mode field profile calculated for the corresponding analytical model. I determined the loss using a finite-element Maxwell's equations solver<sup>Com04</sup> to compute the complex propagation constant  $\beta$  that best fits the electric field along the core center. Computing propagation distance  $z_c$  required fitting the electric field in the waveguide to an exponentially decaying field. I achieved convergence to  $\pm 3\lambda_0$  using a waveguide of length  $9z_c$  and cladding width of nine periods to contain the most weakly-guided modes. Note the good agreement between the full finite-element calculations and those using effective index values.

While a waveguide with the thinnest wires minimizes loss,<sup>AO96</sup> it maximizes fabrication complexity, which is driven by wire cross section and cladding thickness (number of periods required to guide the wave). As shown in Fig. 5.1, as wire width decreases,  $n_{\text{eff}}$  approaches unity ( $n_{\text{eff}} \rightarrow 1$ ). Therefore, the less lossy waveguide modes are weakly guided and more periods of the metamaterial are required to contain them without radiation losses.

Among the metamaterial-cladding geometries considered in Fig. 5.2, I investigated the performance of a waveguide with metamaterial cladding corresponding to  $\frac{b}{a}=0.2$  ( $n_{\text{eff}}=0.87+0.0067i$ ), as shown in Fig. 5.3.

## 5.5 Discussion

The metamaterial waveguide has a similar loss characteristics and mode profile as the equivalent waveguide with an hypothetical homogeneous  $\text{Re}(n_{\text{eff}}) < 1$  cladding (Fig. 5.3). The mode profile depends only slightly on its location relative to the silver wires. Therefore, one can obtain a first design using the effective index values without

need to model the full nanostructured metal-dielectric waveguide. This represents a significant advantage in terms of computation and modeling time.

It is worth comparing the performance of ULIM waveguides to that of other types of waveguides such as metal waveguides, standard dielectric waveguides, and photonic crystal waveguides.

I first compare the attenuation of the ULIM waveguide with a hollow-metallic waveguide. Silver is best for an air-core slab waveguide with metal cladding because it has relatively low losses at visible wavelengths. At  $\lambda_0=500$  nm, its refractive index is  $n_{\text{Ag}}=0.13+2.9i$ , which corresponds to a maximum single-mode core width of  $d_{\text{co}} = 250$  nm. The TE mode in a silver waveguide with  $d = 0.95d_{\text{co}}$  is attenuated by  $\frac{1}{e}$  before it propagates eight wavelengths. As shown in Fig. 5.2, the  $\frac{1}{e}$  power attenuation for the

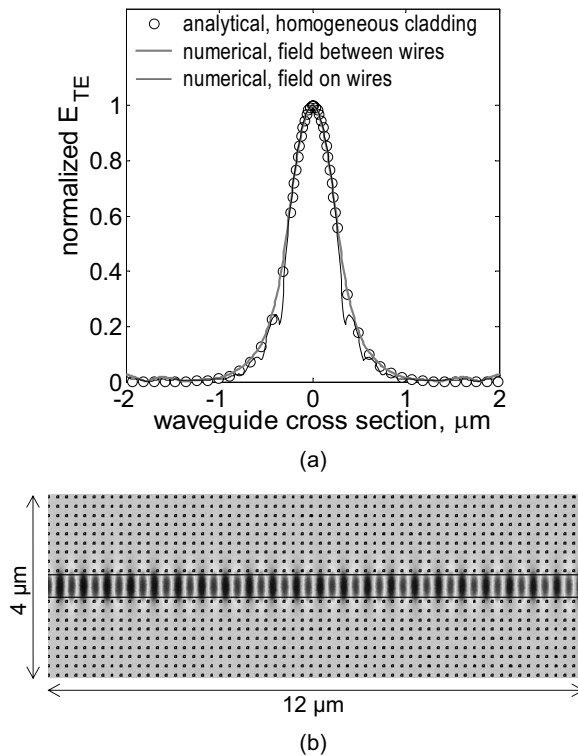


Figure 5.3: (a) Comparison of mode profiles ( $\lambda_0 = 0.5 \mu\text{m}$ ) in slab waveguide with core width  $d_{\text{co}}=0.48 \mu\text{m}$ . The metamaterial cladding is a square array of  $b=40$  nm square silver wires in a  $a=200$ -nm unit cell while the homogeneous cladding has  $\text{Re}(n_{\text{c1}}) < 1$  corresponding to the metamaterial's effective refractive index at  $\lambda_0$ . (b) Electric field (TE) of the metamaterial-cladding waveguide mode.

metamaterial waveguide is more than seven times lower than an optimized waveguide with homogeneous silver cladding. This shows that although there is more penetration into the cladding for the ULIM waveguide than for the silver waveguide, the result is still a less lossy design. Clearly a tradeoff exists between the confinement and the attenuation: For a given unit cell size, thinner wires lead to higher penetration and lower loss<sup>AO96</sup> while thicker wires yield more confinement and higher losses. However, this change is not monotonic as shown in Fig. 5.2 which shows a local optimum at  $\frac{b}{a} \simeq 0.46$ .

Silver has also been used to make nanoparticle plasmon waveguides that propagate electromagnetic energy as surface plasmon polaritons.<sup>QLKA98</sup> Because of their sub-wavelength scale, these devices have potential applications in near-field optical microscopy and integrated optical circuits. They can propagate visible light on the order of a wavelength,<sup>MKA+03</sup> which is appropriate to these applications. In contrast, the metamaterial waveguide designs presented here do not have the same confinement characteristics but can propagate visible light more than 60 wavelengths.

Photonic crystal waveguides also employ periodic structures with line-defects to propagate light by photonic band gap effects, i.e. light in the band gap frequencies can not propagate into the photonic crystal cladding. These waveguides have promising characteristics for photonic integration but still require tight tolerances to reduce scattering losses.<sup>CSVZ01,CSVZ02</sup> Note that ULIM waveguides guide light not by photonic band gap effect but by TER. Therefore, the metamaterial does not require a band gap as shown in Ref. SP03.

Since the ULIM waveguide guides light by TER, I expect that tolerances in the metamaterial's periodicity will only slightly change its index producing low additional losses. For index guided waveguide, the minimum radius of curvature is the figure of merit. For a given radius of curvature, bend loss decreases exponentially with the waveguide's profile height parameter  $\Delta = \frac{n_{co}^2 - n_{cl}^2}{2n_{co}^2}$ .<sup>SL83</sup> Therefore, to obtain sharp bends with ULIM waveguides one would need to maximize the index contrast. This fact

creates another tradeoff between attenuation and bending diameter. Therefore, tapered designs where the confinement is increased as the waveguide approaches a bend can be envisioned and are currently under investigation.

Note that ULIM waveguides can be designed using conventional methods and tabulated values of the effective index. Rigorous electromagnetic methods are needed only in the final stage of optimization. However, as opposed to conventional waveguides, ULIM waveguides can have an air core.

## **5.6 Conclusion**

I have demonstrated for the first time the possibility of guiding light in air by TER using metamaterials with low refractive index. The design of air-core metamaterial-cladding waveguides involves the consideration of several tradeoffs. The examples presented show that the flexibility in the specification of the effective properties of a metamaterial opens up new opportunities for device applications.

## Chapter 6

### Near-IR Total External Reflection Metamaterial Waveguides and Scaling limitations in optical metamaterials\*

#### 6.1 Summary

In Chapter 5 I showed that two-dimensional silver-air metamaterials with  $\text{Re}(n_{\text{eff}}) < 1$  at visible wavelengths can be designed for the cladding of a slab waveguide with a hollow core.<sup>SP04a</sup> Here I design a similar waveguide for near-IR wavelengths and explore the possibility of making a hollow core waveguide with one-dimensional metamaterial cladding. I also consider the scaling effects of nanometer scale metal clusters.

#### 6.2 Ultra-low index optical metamaterials

Ultra-low refractive-index metamaterials (ULIM) with real part of the effective index less than unity are a suitable building block for photonic applications.<sup>SP03</sup> Reference SP03 demonstrated a metamaterial with a two-dimensional square array of cylindrical silver wires embedded in an air host medium. These ULIMs behave like a low-loss dielectric with  $0 < \text{Re}(n_{\text{eff}}) < 1$  on refraction, reflection, and transmission for wavelengths between  $0.45 \mu\text{m}$  and  $1.2 \mu\text{m}$  and light polarized parallel to the wires (see Figs. 6.1 and 6.2). The effective refractive index can be obtained from refraction and reflection calculations using Fresnel formulae. Total external reflection (TER) from finite slabs of the metamaterial has been studied using numerical models.

---

\* This chapter was originally published as Ref. SP04b

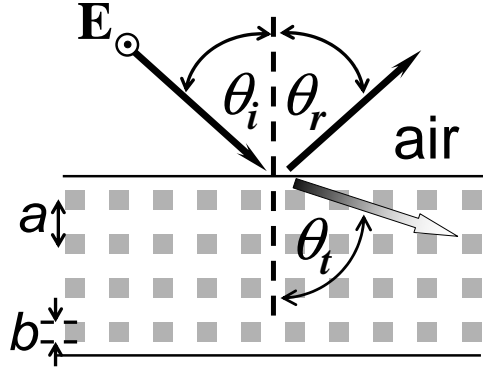


Figure 6.1: Refraction and reflection at the interface of air and a two-dimensional metamaterial with ultra-low effective refractive index. Light is refracted off the normal to the surface and the refracted waves are inhomogeneous. The metamaterial is a square array, period  $a$ , of silver wires of width  $b$  and the incident light is polarized parallel to the wires.

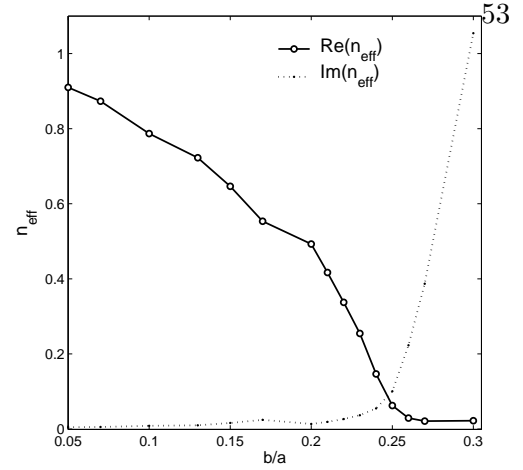


Figure 6.2: Refractive index (real and imaginary parts) of the silver-air metamaterial as a function of wire width  $b$  as predicted by its angle-dependent reflectivity. Unit cell size:  $a = 600$  nm,  $\lambda_0 = 1550$  nm.

### 6.3 Waveguide with ultralow index metamaterial cladding

A slab waveguide with hollow core and metamaterial cladding has been designed and presented in Chapter. 5. The guiding is produced by TER because the cladding's refractive index (real part) is smaller than the core refractive index. Numerical simulations have shown that ULIM waveguides can propagate visible light more than 60 wavelengths, which compares well with current plasmonic waveguides.<sup>QLKA98, MKA<sup>+</sup>03</sup>

Unlike photonic crystal waveguides, which require a photonic band gap to confine light, metamaterial cladding waveguides guide light by TER and do not require a band gap. However, metamaterials with ultralow index are inherently lossy. Nevertheless, photonic crystal waveguides still require tight tolerances to reduce scattering losses.<sup>CSVZ01, CSVZ02</sup> I expect that tolerances in the metamaterial's periodicity will only slightly change its index producing only low additional losses. Moreover, insertion losses should be lower in ULIM waveguides because the modes decay into the cladding as they do in conventional dielectric waveguides, reducing the mode matching problem.

Losses and mode profiles of ULIM waveguides can be predicted using simple and well known analytical models<sup>Rei73</sup> because they are index guided waveguides. The effective refractive index  $n_{\text{eff}}$  of the metamaterial cladding can be obtained with the transfer-matrix method (TMM).<sup>BPMW95, Rey00b, SP03</sup>

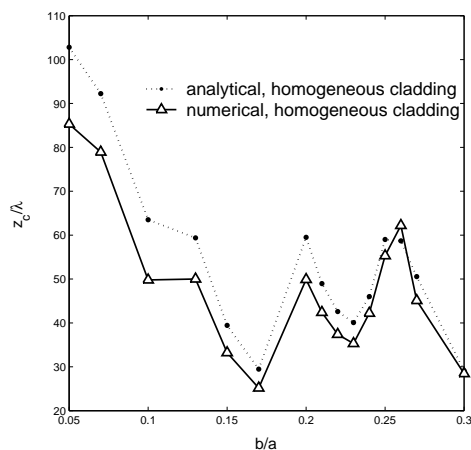


Figure 6.3: Power attenuation ( $\frac{1}{e}$ ) at  $\lambda_0=1550$  nm in single mode slab waveguides with a homogeneous ultralow index cladding corresponding to the predicted  $n_{\text{eff}}$  in Fig. 6.2, and with metamaterial cladding (unit cell size:  $a = 600$  nm, wire width  $b$ ).

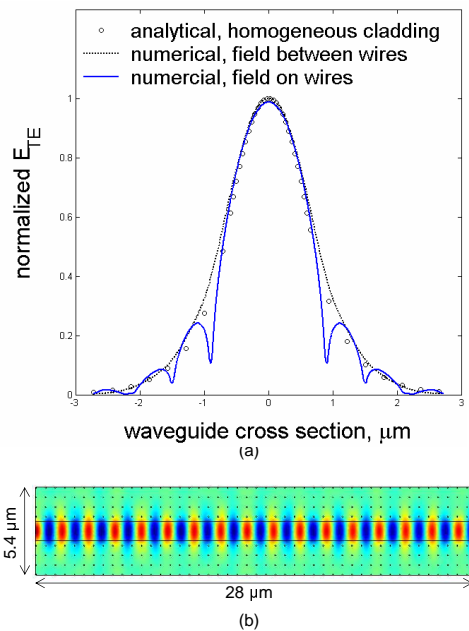


Figure 6.4: (a) Comparison of mode profiles ( $\lambda_0 = 1550$  nm) in slab waveguide with core width  $d_{\text{co}}=1.2 \mu\text{m}$ . The metamaterial cladding is a square array of  $b=60$  nm square silver wires in a  $a=600$ -nm unit cell while the homogeneous cladding has  $\text{Re}(n_{\text{cl}}) < 1$  corresponding to the metamaterial's effective refractive index at  $\lambda_0$ . (b) Electric field (TE) of the metamaterial-cladding waveguide mode.

In Chapter. 5 I considered waveguides for visible light, and here I apply the same process to the infrared. For  $\lambda_0 = 1550$  nm, a metamaterial with unit cell  $a=600$  nm and varying wire widths provides a good range of effective index values for waveguide design, as shown in Fig. 6.2. Figure 6.3 shows the  $\frac{1}{e}$  power attenuation distance  $z_c = \frac{1}{2\text{Im}(\beta)}$ , corresponding to the  $n_{\text{eff}}$  values in Fig. 6.2. These waveguide designs are less lossy than a single-mode hollow waveguide with a silver cladding ( $n_{\text{Ag}}(\lambda_0)$ ), for which  $z_c = 23.4 \lambda_0$  at 1550 nm.

Among the metamaterial-cladding geometries considered in Fig. 6.3, I investigated the performance of a waveguide with metamaterial cladding corresponding to  $\frac{b}{a}=0.1$  ( $b = 60$  nm,  $n_{\text{cl}} = n_{\text{eff}} = 0.79 + 0.0086i$ ), which has an numerical aperture  $NA = \sqrt{n_{\text{co}}^2 - \text{Re}(n_{\text{cl}}^2)} = 0.61$ , accessible with common lenses. This metamaterial waveguide, shown in Fig. 6.4, has similar loss characteristics and mode profile to the waveguide with the equivalent hypothetical homogeneous  $\text{Re}(n_{\text{eff}}) < 1$  cladding. In numerical simulations with only four rows of wires in the metamaterial cladding, the waveguide loss converged to  $z_c = 52\lambda_0$ , which matches the solid curve in Fig. 6.3 at  $\frac{b}{a}=0.1$ . The

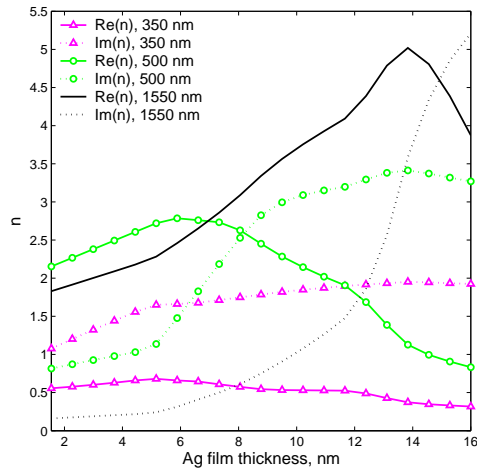


Figure 6.5: Refractive index of silver thin film as a function of film thickness. Data is extrapolated from modified Drude model parameters found in Ref. AO96. The bulk refractive index of silver at  $\lambda=500$  nm is  $0.13 + 2.9i$ .

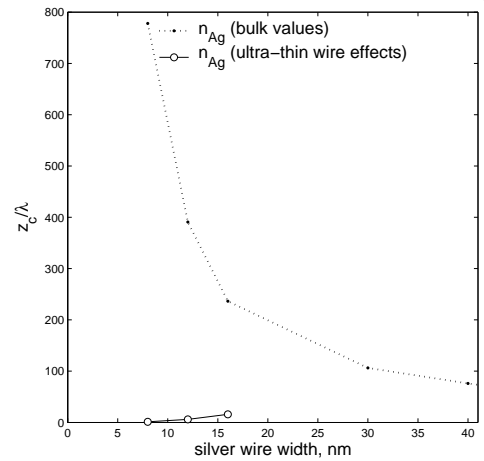


Figure 6.6: Mode propagation distance ( $\frac{1}{\epsilon}$ ) in silver-air metamaterial waveguides (unit cell  $a=200$  nm,  $\lambda_0 = 500$  nm). Top curve: assuming bulk refractive index values of silver. Lower curve: (open circles) computed with thickness-dependent refractive index of ultra-thin silver film.<sup>AO96</sup>

mode profile depends only slightly on its location relative to the silver wires, as shown in Fig. 6.4.

While a waveguide with the thinnest wires minimizes loss, it maximizes fabrication complexity, which is driven by wire cross section and cladding thickness (number of periods required to guide the wave). As shown in Fig. 6.2, as wire width decreases,  $n_{\text{eff}}$  approaches unity ( $n_{\text{eff}} \rightarrow 1$ ). Therefore, the less lossy waveguide modes are weakly guided and more periods of the metamaterial are required to contain them without radiation losses.

Note that thinner wires minimize loss so long as the silver wires are thick enough to retain the optical properties of bulk silver. The refractive index of silver films thinner than  $d \approx 15$  nm have been shown to diverge from their bulk values because of intrinsic size effects, which result in size dependent dielectric functions.<sup>AO96</sup> Since the optical properties of such thin films depend not only on thickness, but on morphology, and hence fabrication conditions, the refractive index values shown in Fig. 6.5 are not necessarily representative of all silver films of a specific thickness. Nevertheless, these results illustrate that the bulk refractive index values commonly used<sup>LH91</sup> do not necessarily apply to such thin silver films.

It is instructive to calculate the performance of metamaterial waveguides with ultra-thin wires ( $b \leq 16$  nm) with the same thickness and structural morphology as the

films studied in Ref. AO96. That is, I assume that a silver wire of width  $b \leq 16$  nm has the same refractive index as a thin film of width  $b$  studied in Ref. AO96. Fig. 6.5 shows that at  $\lambda_0 = 1550$  nm,  $\text{Re}(n_{\text{Ag}}) > 1$  for silver films thinner than 16 nm. Hence, metamaterials made with ultra-thin wires will also have  $\text{Re}(n_{\text{eff}}) > 1$ , and cannot be used as a cladding for a hollow waveguide.

However, at  $\lambda_0 = 500$  nm,  $\text{Re}(n_{\text{Ag}}) < 1$  for thin films thicker than 14 nm, so a metamaterial containing wires of this thickness can guide light by TER. Figure 6.6 shows the  $\frac{1}{e}$  power attenuation distance  $z_c = \frac{1}{2\text{Im}(\beta)}$ , corresponding to the  $n_{\text{eff}}$  values of silver-air metamaterials with wires thinner than 40 nm. Accounting for thin-wire effects on the refractive index of silver dramatically affects the predicted waveguide loss. Therefore, it is possible to find an optimum wire width considering the tradeoffs imposed by the size-dependent index of refraction at the nanoscale and the losses of ULIM waveguides.

#### 6.4 One-Dimensional Stack

As discussed above, a two-dimensional silver-air metamaterial is a candidate for the cladding of a TER-based optical waveguide, but the thin wires required make fabrication a challenge. It is worthwhile to determine here whether a low-loss one-dimensional silver-dielectric metamaterial can have  $\text{Re}(n_{\text{eff}}) < 1$  and be the cladding material for a waveguide.

A periodic layered medium has the optical properties of a birefringent uniaxial crystal at wavelengths much larger than its period. The structural anisotropy of a periodic layered medium yields the equivalent effect known as *form birefringence*.<sup>?</sup> For wavelengths much larger than each layer, the electric field in the layer can be considered constant and simple analytical expressions for the ordinary and extraordinary effective refractive indices are as follows:

$$n_o^2 = \frac{1}{a} (h_2 n_2^2 + h_3 n_3^2) \quad (6.1)$$

$$\frac{1}{n_e^2} = a \left( \frac{1}{h_2 n_2^2} + \frac{1}{h_3 n_3^2} \right) \quad (6.2)$$

where  $n_i$  and  $h_i$  are the refractive indices and thickness of the layers and  $a = (h_2 + h_3)$ .<sup>?,?</sup>

I need to choose component materials with refractive index values that yield

$n_o < 1$  (Eq. 6.1) to design a one-dimensional stack with an  $\text{Re}(n_{\text{eff}}) < 1$  for s-polarized light (electric field parallel to the stack layers). Because of their low refractive index values for visible light,  $\text{MgF}_2$  and silver are good candidates to design a multilayer stack with index less than one. At  $\lambda_0 = 500$  nm, the bulk refractive index values are  $n_{\text{MgF}_2} = 1.38$  <sup>Dod84</sup> and  $n_{\text{Ag}} = 0.13 + 2.9i$ . <sup>LH91</sup>  $\text{MgF}_2$  has a low refractive index compared to other optical films, and while for bulk silver,  $\text{Re}(n_{\text{Ag}}) < 1$  over the visible spectrum, the lowest loss is at  $\lambda_0 \approx 500$  nm.

Let us consider, as an example, an Ag- $\text{MgF}_2$  stack of period  $a$  and silver fill factor  $f = 0.15$ . According to Eq. 6.1, the ordinary refractive index (for light polarized parallel to the layers) should be  $n_{\text{o,eff}} = 0.48 + 0.12i$ . However, as discussed above, for a stack to have the optical properties of a homogeneous dielectric, the period  $a$  must be much smaller than the wavelength. To quantify how small  $a$  should be, I calculated the complex refractive index of homogeneous dielectric slabs whose reflectivity  $\mathcal{R}(\theta)$  best matches that of a metal-dielectric stack <sup>BW80</sup> with fill-factor  $f$  and period  $a$  at all incident angles for polarization normal to the incident plane (TE) and parallel to the layers. That is, I determined the effective index by comparing the reflectivity of the metamaterial with that of a homogeneous material as predicted by the Fresnel formulae. As shown in Fig. 6.7, the effective index of stacks of different silver fill-factors converges to within 10% of the predicted form-birefringence value for  $a < \frac{\lambda}{20}$ .

Note that the stack with a 0.15 silver fill factor converges faster than the others, as  $\Delta < 5\%$  for  $\frac{a}{\lambda} < 0.18$ . Yet, for a stack with this fill-factor and unit cell size, the silver films are thinner than 16 nm, and hence will not have the bulk optical properties assumed when calculating  $n_{\text{o,eff}}$  in Fig. 6.7. Hence, to design a Ag- $\text{MgF}_2$  stack that can potentially have  $n_{\text{o,eff}} < 1$ , I must first consider the refractive index of ultra-thin silver films and then determine the optimum geometry.

From Fig. 6.5 I observe that at  $\lambda_0 = 500$  nm, the size-dependent refractive index yields  $\text{Re}(n_{\text{Ag}}) < 1$  for thin films of widths between 14 nm and 16 nm. Therefore I studied the effective index of Ag- $\text{MgF}_2$  stacks with 16-nm thick silver films at  $\lambda_0 = 500$  nm, which have the lowest loss and smallest  $\text{Re}(n_{\text{Ag}})$  in this thickness range. Figure 6.8 summarizes these results and shows that both the real and imaginary part of the refractive index are too high for a low loss Ag- $\text{MgF}_2$  stack with  $\text{Re}(n_{\text{eff}}) < 1$  for any

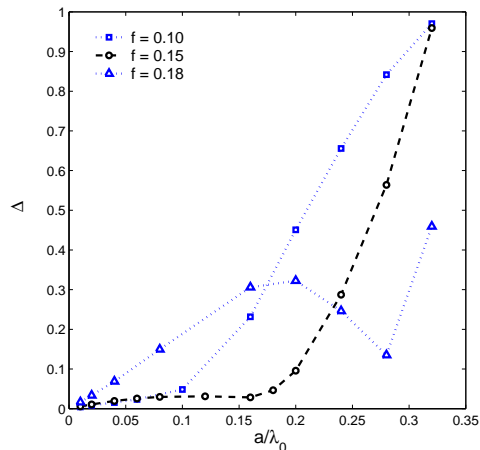


Figure 6.7: Convergence of Ag-MgF<sub>2</sub> stack effective index to form birefringence prediction (Eq. 6.1) as period  $a$  gets very small compared to the wavelength,  $\lambda_0=500$  nm. Each curve represents a different silver fill-factor  $f = \frac{hAg}{a}$ .  $\Delta$  denotes the relative difference between the numerical transfer-matrix method ( $n_{\text{TMM}}$ ) and analytical refractive index ( $n_o$ ) predictions;  $\Delta = 2 \left| \frac{n_{\text{TMM}} - n_o}{n_{\text{TMM}} + n_o} \right|$ .

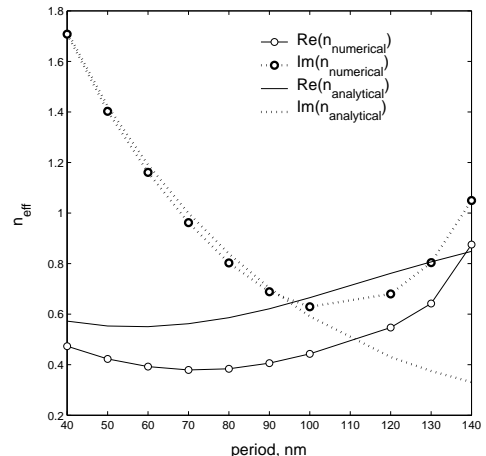


Figure 6.8: Effective refractive index of silver-MgF<sub>2</sub> dielectric stacks as a function of period, calculated both numerically and analytically (Eq. 6.1) at  $\lambda_0 = 500$  nm. The silver films in each stack are 16-nm thick. Numerical predictions are based on the complex refractive index that best fits  $\mathcal{R}(\theta)$  of the slab.

silver fill-factor. This suggests that one-dimensional metal-dielectric stacks might not be appropriate for TER waveguides.

## 6.5 Conclusion

Two-dimensional silver-air metamaterials can be designed for the cladding of a TER slab waveguide with relatively low loss. Nevertheless, implementing such designs is still challenging. Numerical models predict TER at visible wavelengths for one-dimensional Ag-MgF<sub>2</sub> stacks that can be easily fabricated. Yet, for such stacks to exhibit true form birefringence, i.e. have an effective refractive index at these wavelengths, the silver films must be approximately 15 nm thick. However, the refractive index of such films diverges from their bulk values such that they are no longer suitable for ultralow refractive index metamaterials. Therefore, current research is directed to optimize two- and three-dimensional geometries for TER waveguides.<sup>†</sup>

<sup>†</sup> Since the original publication of this chapter, preliminary TMM simulations have shown  $n_{\text{eff}}^R = 0.92 + 0.01i$  (based on angle-dependent reflectivity, both  $s$  and  $p$  polarizations) at  $\lambda_0 = 500$  nm for an inverted opal structure with unit cell  $a = 346$  nm and a silver coating thickness  $t_c = 1$  nm. This simulation assumes the bulk refractive index of silver, which, as discussed here, is not a valid assumption. These simulations also involve extremely coarse sampling of the unit cell, as discussed for other opals photonic crystals in Chapter 7.

## Chapter 7

### Modifying silica opal photonic crystal spectra with thin conformal alumina coatings

#### 7.1 Summary

Atomic layer deposition rates of alumina on silica opals match the alumina deposition rates on planar substrates when the coating thickness is less than 10% of the opal sphere radius. Controlling opal coating thicknesses facilitates the precise engineering of photonic band gaps in synthetic opals. Thin alumina films on opals are required for the conformal deposition of metals on silica opals, which have applications for photonic band gap materials.

#### 7.2 Introduction

As discussed in the Chapter 1, inverted opal photonic crystals can exhibit photonic band gaps at visible wavelengths if the dielectric constant contrast between the two component materials is sufficiently high.<sup>Yab87, Joh87, YG89</sup> In such a structure, the ratio of the dielectric constants of the solid material and the spherical voids must exceed 7.8 and the gap width ranges from 5-15% of the center frequency.<sup>BJ98</sup> Coated opal structures consisting of dielectric or metal films over a hollow opal have similar optical properties.<sup>RPGT05, ZLW+00, WCZ+01</sup>

Compared to other structures with three-dimensional periodicity, a synthetic dielectric opal structure can be fabricated affordably and reliably via self-assembly<sup>LVM+97, CGMA03, NAM</sup> of individual spheres produced by the Stöber method.<sup>WSB68</sup> Common ways of creating inverted or coated opal structures is to infiltrate the dielectric opal structure with a thin metal or high-refractive index coating and then etch away the dielectric yielding

an inverted opal network of connected spherical shells.<sup>VK97,SSL<sup>+</sup>ed</sup> Methods include thermal decomposition,<sup>GKK<sup>+</sup>01</sup> spray pyrolysis,<sup>AYLK04</sup> ceramic fabrication,<sup>SCSH99</sup> and atomic layer deposition, which was used for the opals discussed here.

Atomic layer deposition is a chemical vapor deposition (CVD) process where the full reaction to create the atomic layer is divided into two alternating steps, each involving the deposition of one of two gaseous precursors  $A$  and  $B$ . Precursor  $B$  reacts with the previously-applied precursor  $A$  to both form the desired coating and prepare the surface for another deposition of  $A$ . Hence the number of coating cycles determines the coating thickness.<sup>OK96</sup>

Atomic layer deposition (ALD) is a suitable method of depositing material on an opal structure because it results in uniform and conformal coatings, even on high aspect ratio geometries such as opals where precursor molecules must travel long paths through narrow channels.<sup>MEG<sup>+</sup>03</sup> Such coatings are necessary to minimize defects that can destroy a photonic band gap.<sup>KNS<sup>+</sup>03,RBGT03</sup>

Coating thickness can determine whether the photonic crystal exhibits a PBG and how wide the gap is. Metal spheres arranged in various close-packing arrangements can exhibit a photonic band gap if their filling fraction exceeds a critical value, for example, 53% for a face-centered cubic array.<sup>ZLW<sup>+</sup>00</sup> Since dielectric nanoscale spheres are easier to fabricate than those made of metal, metal opal photonic crystals have generally consisted of dielectric spheres with a metal coating thicker than its relevant skin depth. Such a structure mimics that of solid metal spheres.<sup>WCZ<sup>+</sup>01</sup> Since metals at optical wavelength have non-negligible loss, an optimized metal-coating is just thick enough to shield the core from electric fields. While a thicker metal coating on the sphere increases its radius and theoretically the gap width, it increases attenuation. Hence, increasing the net sphere radius is best done by increasing the size of the dielectric spheres. Coating thickness is also critical for the band-gap properties of tungsten-coated opal structures,<sup>vFJSD<sup>+</sup>04</sup> which will be discussed in Chapter 8.

Atomic layer deposition could also be used to create metallic nanoshells. Their optical resonances depend strongly on shell thickness<sup>SJOH98</sup> and have applications in optical devices, chemical and biological sensors, and cancer treatments.<sup>Hal01, Bro03</sup>

Hence precise control and knowledge of the thickness of the metal film deposited

via ALD is critical. In this Chapter I discuss ALD of alumina on silica opals. While self-assembled opal structures commonly employ silica spheres, not all coatings deposited via ALD can nucleate, that is, form a uniform conformal coating, on the silica spheres. Because they can do so on alumina, alumina has functioned as an adhesion layer between the opal material of the desired coating.<sup>EWS<sup>+</sup>03,SFH<sup>+</sup>at</sup>

An adhesion layer can also serve to change the photonic crystal geometry. While several sizes of silica nanospheres are commercially available, the best photonic crystal geometry may require an in-between size. In the case of metal-coated opals, precise control of the adhesion layer can effectively enlarge the spheres and can fine tune the opal geometry before depositing the metal coating.

One method of estimating the coating thickness on opals is to directly measure the coating deposition rate on a planar substrate and assume the same rate applies to the opals. However, ALD precursors must travel in large aspect ratio paths in the opal, which increase further as coating thickness  $t_c$  increases. For an f.c.c. (face-centered cubic) lattice of spheres of radius  $r$ , the coating completely fills the voids then  $t_c = (\sqrt{2} - 1)r = 0.414r$ . In this limiting case, the almost completely-infiltrated opal has an extremely high aspect ratio, and planar deposition rate certainly does not apply. Hence, the purpose of the numerical simulations discussed in this chapter is to find the applicable range of this approximation and validate the accuracy of laboratory methods of controlling coating thickness. A forthcoming publication will address the details of the experiment.<sup>SSL<sup>+</sup>ed</sup>

### 7.3 Methods

One method of determining the thickness of a coating on an opal structure is to compare its reflectance spectrum with an analytical model or numerical simulation of the coated opal's reflectivity. The Bragg Law is a simple analytical model to characterize opal photonic crystals according to the wavelength  $\lambda_{\max}$  corresponding to the maximum reflected intensity of the first diffraction order.<sup>BB24,LVM<sup>+</sup>97,BML99</sup>

$$\lambda_{\max} = 2d_{111}\sqrt{n_{\text{eff}}^2 - \sin^2(\theta)}. \quad (7.1)$$

Here,  $d_{111}$  is the distance between planes of spheres normal to the  $\langle 111 \rangle$  propagation direction and  $\theta$  is the incident angle with respect to the  $\langle 111 \rangle$  planes. The effective

refractive index  $n_{\text{eff}}$  is approximated by the sum of the refractive indices of each component material (host (h), sphere (s), and coating (c)) weighted by their respective fill factors:  $n_{\text{eff}} = n_h f_h + n_s f_s + n_c f_c$ . As discussed in Chapter 2, the method of approximating the refractive index applies best in the long-wavelength limit. Yet, in this application, the peak wavelength is typically less than twice the lattice constant, and has been found to overestimate the diameter of uncoated opals by 2.5%.<sup>RCGV+99</sup>

The transfer-matrix method (TMM)<sup>BPMW95</sup> implemented as the Translight software package,<sup>Rey00b</sup> already discussed in previous chapters, provides a more rigorous method of characterizing coated opals and hence determining the coating thickness. While this method is more computationally intensive than the Bragg Law, it is more accurate. The TMM accounts for the opal's subwavelength feature sizes and can find peak spectral wavelengths for opal structures of finite thickness. As will be shown below, the locations of these peaks depend on sample thickness for opals consisting of fewer than about 10 layers.

## 7.4 Numerical Simulation

A representative geometry of bare opal structure is required for accurate modeling with the Bragg Law and transfer-matrix method. The relevant parameters are the peak wavelength of the bare opals used in the experiment, the interplanar spacing  $d_{111}$  and sample thickness, the refractive index of the silica and alumina, and the alumina deposition rate.

The average peak wavelength of 17 different uncoated opals<sup>1</sup> was  $\lambda_0 = 576 \pm 6$  nm. SEM scans of the opals showed that the interplanar spacing  $d_{111} = 216 \pm 9$  nm, which, assuming a perfect opal structure, means that the average sphere diameter is  $2r_s = \sqrt{\frac{3}{2}}d_{111} = 132$  nm. The opal structures were  $2.5 \mu\text{m}$  thick, which means that on average each sample consisted of 12 sphere planes. The alumina deposition rate on silica was found to be  $1.33 \text{ \AA}$  per coating cycle,<sup>SSL+ed</sup> which agrees with previous findings.<sup>EG03</sup>

The refractive index of silica nanospheres ranges from  $n_{\text{sp}} = 1.415$  to  $n_{\text{sp}} = 1.455$  at  $\lambda_0 = 589$  nm and depend on how they are prepared.<sup>CJN04</sup> The simulation results

---

<sup>1</sup> Opal fabrication, self-assembly, and characterization were performed by Z. A. Sechrist, J. H. Lee, F. H. Fabreguette, J. A. McCormick, and S. M. George in the Department of Chemistry and Department of Electrical and Computer Engineering at the University of Colorado.

shown here used a mid-range value of  $n_{\text{sp}} = 1.43$  and a refractive index of ALD alumina films of  $n_{\text{al}} = 1.65$  in accordance with previous measurements.<sup>OMK<sup>+</sup>96</sup>

Translight was run on a dual Xeon 3.60 GHz processor Dell Precision Workstation 670 with 4 GB RAM running Windows XP Professional (32-bit). For good numerical stability, the three template files that comprise the opal  $\langle 111 \rangle$  unit cell were split into three files, creating an interleaved lattice.<sup>PM92,Rey00a</sup> In this configuration, the smallest cubic grid spacing within the cubic unit cell  $a$  was  $\frac{a}{24}$ , or in the  $\langle 111 \rangle$  direction of propagation  $\min(\Delta) = \frac{d_{111}}{14}$ . At this resolution, computing the reflection and transmission coefficients at one wavelength took more than one hour. Virtual memory limits prevented using denser meshes. The results presented here are for simulations with  $\Delta = \frac{d_{111}}{8}$ . Appendix A discusses convergence of  $\lambda_{\text{max}}$  as a function of mesh spacing, and concludes that  $\lambda_{\text{max}}$  computations with  $\Delta = \frac{d_{111}}{8}$  mesh spacing are approximately 5 nm higher than the converged value.

## 7.5 Results

Figure 7.1 compares the shift in peak wavelength and change in peak intensity as a function of alumina coating thickness for two experimental data sets and Translight simulation of a 96-layer thick opal. This plot assumes the planar deposition rate of 1.33 Å/cycle for the experimental data sets. In the numerical simulations, the peak wavelength ceases to increase for coatings thicker than  $t_c = 33$  nm. The experimental data shows only a slight leveling off, and the continues to  $\lambda_0 = 677$  nm. Table 7.1 summarizes the results and compares them to the Bragg law predictions (Eq. 7.1). The numerical simulation prediction of the  $\Delta\lambda_{\text{max}}$  is within 5.5% of the Bragg law prediction.

Table 7.1: Transfer-matrix method (TMM)<sup>Rey00b</sup> and Bragg law prediction (Eq. 7.1) of  $\lambda_{\text{max}}$ , the peak of the reflection spectrum of silica opal ( $n=1.43$ ) photonic crystals in the ( $\langle 111 \rangle$  orientation) orientation. The bare opal has no coating. In the filled opal, the alumina coating ( $n = 1.43$ ) completely fills the voids between the silica spheres. The planar spacing is  $d_{111} = 216$  nm.

	experiment	TMM,	Bragg Law
$\lambda_{\text{max}}$ uncoated opal	576 nm	574 nm	569 nm
$\lambda_{\text{max}}$ filled opal	677 nm	645 nm	642 nm
$\Delta\lambda_{\text{max}}$	101 nm	69 nm	73 nm

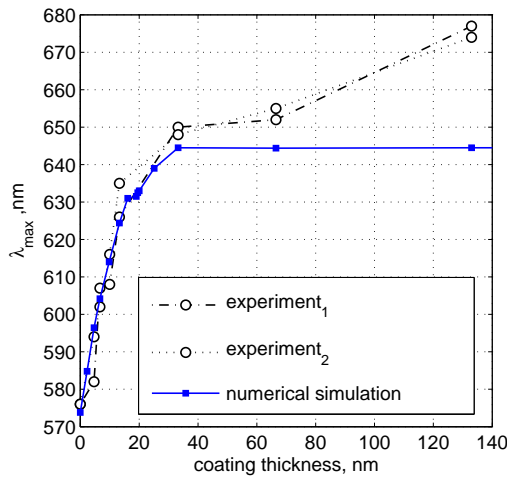


Figure 7.1: Shift in maxima of reflection spectrum of silica opal photonic crystals ( $\langle 111 \rangle$  orientation) as a function of alumina coating thickness. Planar spacing for numerical simulations is  $d_{111} = 216$  nm. For experimental data sets, coating deposition rate is assumed to be  $1.33 \text{ \AA/cycle}$ .

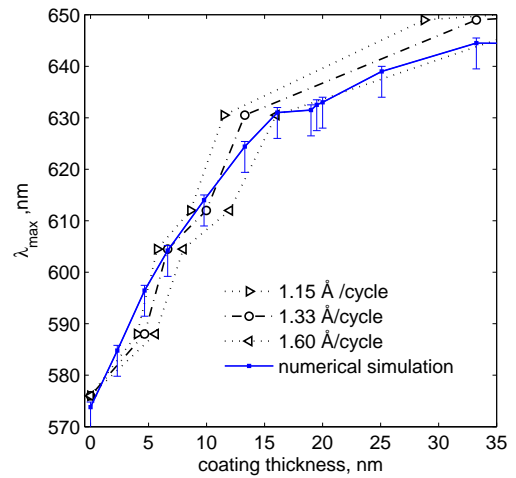


Figure 7.2: Linear region of Fig. 7.1 for three alumina deposition rates on silica opal. The planar deposition rate is  $1.33 \text{ \AA/cycle}$ . See Appendix A for the derivation of the error bar values.

If the  $1.33 \text{ \AA/cycle}$  planer deposition rate were valid for opals, the alumina would infiltrate the opal at approximately 410 cycles, or 65-nm thick alumina coating. Since Fig. 7.1 shows that this is not the case, it is worth determining a range of deposition rates on the silica spheres by fitting the experimental values of  $\lambda_{\max}$  to the numerical predictions. Figure 7.2 shows this for coating thicknesses corresponding to incompletely infiltrated opals. The  $1.33 \text{ \AA/cycle}$  planer deposition rate provides a good fit for  $t_c \lesssim 15$  nm. More experimental data points corresponding to  $15 \text{ nm} < t_c < 35 \text{ nm}$  are needed to determine the deposition rate the best applies for these coating thicknesses.

As suggested in the Section 7.2, one reason that  $\lambda_{\max}$  continues to shift is that the coating does not completely infiltrate the voids because coated opal's increased aspect ratio decreases the alumina growth rate. As the alumina conformally coats the spheres, the gaps between the spheres shrink, which hinders the path of precursor molecules to the deeper layers of opal. Since the ALD process depends on alternating occurrences of two different precursor reactions, decreasing the probability of either event decreases the yield of the total process, and hence decreases the film growth rate.<sup>EG03,SSL<sup>+</sup>ed</sup>

While decreased growth rate accounts for the wavelength maxima not leveling off, it does not account for the larger wavelength shift. The distribution of spheres sizes could account for this difference. If the larger spheres contribute most to the lattice spacing, the presence of smaller spheres in such a lattice decreases the net fill factor from the 74% corresponding to a f.c.c. lattice. Compared to the “filled” lattice, this small-fill fraction lattice can accommodate more alumina and hence allow for larger wavelength shifts.

## 7.6 Conclusions

Assuming an alumina coating deposition rate valid for flat substrates, the numerical simulations agree with the experimental results for alumina coatings thinner than  $t_c \sim 15$  nm ( $\sim 110$  cycles), or a fractional coating thickness of  $\frac{t_c}{r} = 0.11$ . Since artificial opal photonic crystals with thinner coatings have exhibited a photonic band gap,<sup>ZLW+00,RCJA01</sup> the results shown here suggests that this method of determining opal coating thickness is applicable to engineering photonic band gap structures and fine tuning their spectral properties.

## Chapter 8

### Photonic band gap in the near-IR with tungsten-coated artificial opals

#### 8.1 Summary

Numerical simulations of metal-coated synthetic opals were shown to exhibit a photonic band gap effect consistent with experimental measurements of tungsten-coated opals. These structures have potential applications as efficient lighting devices.

#### 8.2 Introduction

For a photonic crystal to exhibit a photonic band gap, the ratio of the dielectric constants of the constituent materials must exceed a threshold value.<sup>Yab87, Joh87</sup> Compared to other structures with three-dimensional periodicity, an inverted opal structure can be fabricated affordably and reliably. In such a structure, the ratio of the dielectric constant  $\epsilon$  of the solid material and the spherical voids must exceed about 8.<sup>BJ98</sup> Coated opal structures consisting of dielectric films over a hollow opal have similar optical properties.<sup>RPGT05</sup>

Fabricating inverse opal photonic crystals with band gaps at visible wavelengths is challenging because few materials have a sufficiently high dielectric constant at these wavelengths.<sup>Pal91</sup> Because impurities in fabricated photonic crystals invariably distort the band structure and can destroy a band gap,<sup>LZ00</sup> dielectric constant contrasts are required for structures more tolerant to such lattice imperfections.<sup>Mor99</sup> However, a recent numerical and experimental study suggests a photonic band gap effect in the visible with tantalum nitride ( $\epsilon \approx 9$ ) shells.<sup>RPGT05</sup>

Another approach to achieving a three-dimensional photonic band gap structure at visible wavelengths has been to design metal photonic crystals.<sup>SCHS95, EKSB+00</sup> While

dielectric photonic crystals are generally lossless and hence have good transmission properties, several layers are required to achieve the band gap effect. Since metals typically have low loss at centimeter and millimeter wavelengths, metal photonic crystals can achieve low-loss band gap effects with fewer periods than dielectric band gap structures, and are hence easier and less costly to fabricate than other geometries.<sup>BM95,OTS+96</sup>

While metals are more lossy at visible wavelengths than in the microwave region, the real parts of their dielectric functions are large and negative, which makes them candidates for components of photonic crystals in this spectral region. For example, in terms of the dielectric constant ratio, an FCC lattice of metal spheres is similar to that of an inverted opal consisting of hollow spheres in a high- $\epsilon$  host.<sup>Mor99</sup>

FCC arrays of metal spheres have band gaps of widths ranging from 30% to 60% of the center frequency close to  $\lambda_0 = 1 \mu\text{m}$ .<sup>ZLW+00,WCZ+01</sup> The metal spheres required for such PBG structures have a radius close to 160 nm, which is larger than typical metal nanoparticles. However, dielectric spheres of this size are common,<sup>Duk04</sup> and when coated with metal, can be considered equivalent to coated opal structures if the coatings thicker than the skin depth.<sup>WCZ+01</sup>

One difference between a photonic crystal consisting of isolated metal elements, such as metal spheres in an FCC array, and one where the metals touch, such as a metal inverted opal, is that the latter has a *network topology*. While a photonic crystal of isolated metal scatterers can produce a band gap as dielectric photonic crystals do, photonic crystals with a network topology have a cutoff wavelength above which no modes propagate. (See, for example, the band diagram of two-dimensional metal wire photonic crystals shown in Fig. 2.2 and Fig. 4.4). Hence, instead of a band gap, such structures exhibit a band edge or stop band. The photonic crystal geometry determines the cutoff frequency, below which no modes propagate, which for two-dimensional periodic structures is

$$\nu_c \approx \frac{c}{\sqrt{\epsilon_{\text{eff}}} a}, \quad (8.1)$$

where  $a$  is the period of the photonic crystal and  $\epsilon_{\text{eff}}$  is its effective dielectric constant.<sup>SCHS95,PE02</sup>

This approximation can be understood if the photonic crystal is viewed as an array of planar mirror waveguides. For  $s$  polarized light incident normal to the plane

of the waveguides, the tangential component of the electric field is continuous across the air-metal boundary. Since the conducting walls hold no field, and the field in the waveguide is zero at the air-metal interface. The sinusoidal mode solutions in each waveguide limit  $m$ , the number of allowed modes, to  $m < \frac{2a}{\lambda}$ . For  $a < \frac{\lambda_0}{2}$ ,  $m = 0$ , and the grating structure does not guide s-polarized light through it.

Since the metal-coated opal has non-planar boundaries, this approximation serves only as a rough guideline. As applied to light the metal coated opals in the  $\langle 111 \rangle$  orientation, the relevant spacing in Eq. 8.1 is the interplanar spacing  $d_{111} = \frac{a}{\sqrt{3}}$  and  $\epsilon_{\text{eff}} \cong 1$  because the metal coating significantly shields the silica spheres inside. The result is the Bragg law applied at normal incidence, Eq. 7.1, and the cutoff wavelength is simply

$$\lambda_c = 2d_{111} = 3.266r \quad (8.2)$$

Expressed as a normalized frequency,  $\Omega_c \equiv \frac{a}{\lambda_c} = \frac{\sqrt{3}}{2} = 0.866$ .

Tungsten has received this attention because of its high melting point<sup>Lid</sup> and the ability to use photonic band gaps to engineer thermal radiation spectra. A photonic band gap corresponds to a zero photon density of states (DOS) at frequencies within the gap. If the photonic crystal is heated to a temperature such that its peak radiation wavelength  $\lambda_m$  (according to Wien's displacement law) is within the band gap, the radiation peak will not occur at  $\lambda_m$ , but a wavelength corresponding to a higher DOS.<sup>LF EK03, Li02, LNCJ04</sup> Photonic crystals engineered to have this higher DOS at visible wavelengths have applications for efficient lighting devices.

Tungsten has recently been used in fabrication of photonic crystals with omnidirectional stop bands. A "woodpile" structure containing  $1.2 \mu\text{m}$  wide tungsten bars stacked orthogonally and spaced by  $4.2 \mu\text{m}$  has been shown to have a photonic bandgap between 8 and  $20 \mu\text{m}$ .<sup>FLEK+02, LEKH+03</sup> A smaller structure consisting of  $0.50 \mu\text{m}$  wide tungsten bars stacked orthogonally and spaced by  $1.5 \mu\text{m}$  has a bandgap starting at  $1.5 \mu\text{m}$  and exhibits efficient radiation near this wavelength when a voltage is applied to it.<sup>LF EK03</sup>

While tungsten's high melting point qualifies it for potential applications in photonic crystal lighting, its established use in atomic layer deposition<sup>KFG00, ENGG01, SFH+at</sup> suggests that an inverted opal structure would be a promising geometry for mass pro-

duction. In this chapter I use numerical simulations to validate the reflectance spectra showing the band edge of three sizes of silica opals (nominal radii  $2r=0.70\ \mu\text{m}$ ,  $1.0\ \mu\text{m}$ , and  $1.6\ \mu\text{m}$ ) coated with 25-nm thick tungsten films. They are fabricated via the atomic layer deposition process described in Chapter 7.

### 8.3 Methods

To simulate the tungsten-coated opal, the opals were assumed to occupy a perfect FCC lattice with unit cell  $a = 2r\sqrt{2}$ , which yields a 74% sphere fill-fraction. Table 8.1 summarizes the experimental and numerical opal geometries.

Since the absolute value of both the real and imaginary part of metal dielectric constants are large at visible and near-IR wavelengths, I recompiled Translight,<sup>Rey00b,Rey00a</sup> a transfer-matrix program<sup>BPMW95</sup> to accept these ranges of values for coatings. For convergence, the three template files representing the unit cell were split into two sets of three files. Since this software can model only a single coating layer, the alumina nucleation layer between the silica and tungsten was neglected. As in Chapter 7, the refractive index of silica used in the simulations was  $n=1.43$  and computer memory limits the spatial resolution of the TMM numerical simulations.

As discussed above, the dielectric constant contrast between the opal spheres and their surroundings is critical to the formation of a photonic band gap. To accurately simulate the tungsten coating on the silica opal, an appropriate dielectric constant should be used. A natural choice would be that measured for tungsten,<sup>LH91,OLB+83</sup> but as shown in Fig. 8.1, their reflectance spectra are not similar.<sup>1</sup> The black solid curve is

<sup>1</sup> Thin-film reflectivity measurements performed by Zachary Sechrist with the Cary 500 UV-VIS-NIR Spectrophotometer in the W.M. Keck Optical Measurement Laboratory at JILA, University of Colorado.

Table 8.1: Sphere radii and unit cell sizes of silica opals used in experiments and numerical simulations. Unit cell values assume a perfect FCC lattice, where  $2r$  is the sphere diameter and unit cell  $a = 2r\sqrt{2}$ .

$2r$ experiment*	$2r$ simulation	$a$ experiment	$a$ simulation
$701 \pm 9\ \text{nm}$	700 nm	$991 \pm 25\ \text{nm}$	990.0 nm
$993 \pm 10\ \text{nm}$	1000 nm	$1404 \pm 28\ \text{nm}$	1414 nm
$1587 \pm 21\ \text{nm}$	1600 nm	$2244 \pm 59\ \text{nm}$	2263 nm

\*Average sphere diameter and standard deviation. Data and spheres supplied by Duke Scientific Corporation.<sup>Duk04</sup>

the reflectivity of a tungsten film deposited by ALD under the same conditions as the silica opals. Note that its reflectivity is constant at wavelengths longer than  $\lambda_0 \approx 1.5 \mu\text{m}$ , while tungsten's refractive index values predict a constant reflectivity above  $\lambda_0 \approx 2.3 \mu\text{m}$ .

To remove this discrepancy, simulations were done assuming the refractive index of silver, which has a constant reflectivity at visible and near-IR wavelengths, shown by the thick gray curve in Fig. 8.1. Since the magnitude of the reflectivity differs from that measured for tungsten, this simulation should predict only the shift in the cutoff wavelength  $\lambda_c$  (and corresponding normalized cutoff frequency  $\Omega_c \equiv \frac{a}{\lambda_c}$ ) as a function of sphere size, and not the magnitude of reflectivity. Since computations of FCC arrays of non-touching copper, nickel, and silver have shown similar trends in their band gap locations,<sup>WCZ<sup>+</sup>01</sup> modeling silver-coated opals should be adequate to validate the experimental measurements of tungsten-coated opals.

## 8.4 Results

As discussed in Chapter 7, limited computer memory limited the sampling density in the opal unit cell such that the sample spacing exceeded half the tungsten coating thickness,  $t_c = 25 \text{ nm}$ . Appendix B shows numerical predictions of cutoff frequency serve as lower limits because of the coarse sampling.

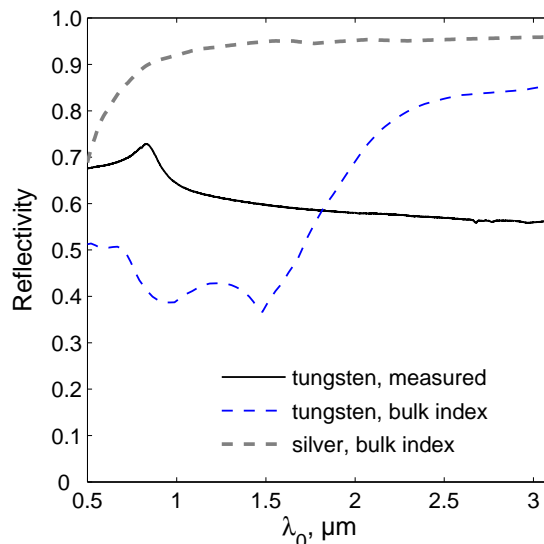


Figure 8.1: Reflectivity of 25-nm metal films. Black solid line: measured reflectivity of tungsten film. Others: calculated from refractive index data. Refractive index data for curves marked with ♣ and ◇ are from Ref. LH91 and Ref. OLB<sup>+</sup>83 respectively.

Having established the lower bound for the numerically computed cutoff frequency, I can now compare the numerically simulated spectra to those measured. Figures 8.2, 8.3, and 8.4 show these for the  $2r = 700$  nm,  $2r = 1000$  nm, and  $2r = 1600$  nm opals, respectively. While the simulations with coarse sampling show a longer cutoff wavelength (see Appendix B) than the experimental data, the difference decreases as the sampling density increases. Table 8.2 summarizes the converged cutoff wavelengths and corresponding normalized cutoff frequencies. In addition to the convergence of the numerical simulations, geometrical differences between the opal in the numerical simulations and the fabricated synthetic opals may account for the discrepancies in cutoff wavelengths  $\lambda_c^{\text{exp}}$  and  $\lambda_c^{\text{TMM}}$  in Table 8.2.

One such cause is that the fabricated opal was not perfectly periodic. This occurs because of imperfect self-assembly, which yields isolated regions of an FCC lattice separated by fissures and/or non-periodic regions.<sup>VDN00,CGMA03</sup> While these defects certainly distort the reflectance spectrum, quantifying them would require probing small regions of the opal corresponding to different geometries.<sup>CGMA03</sup>

Another cause could be sphere deviations of sphere diameters in the self-assembled opal, shown in Table 8.1. This distribution in sphere sizes smears out the cutoff wavelength, as the spectrum is effectively a superposition of opals with spatially varying planer spacings  $d_{111}$  determined by the size of the specific spheres in the area.

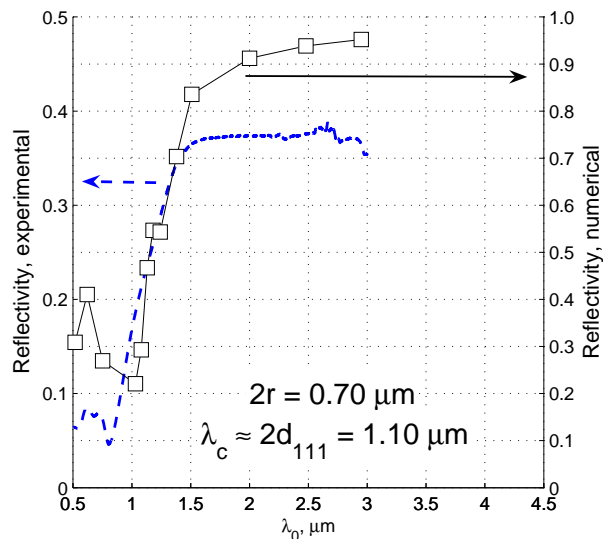


Figure 8.2: Reflectivity spectra of a silica opal ( $2r=700$  nm) photonic crystal coated with 25-nm tungsten coating. The grid spacing for the numerically-simulated spectrum in this plot is  $\Delta = 58$  nm, and the plotted reflectivity is the average of TE and TM polarizations.

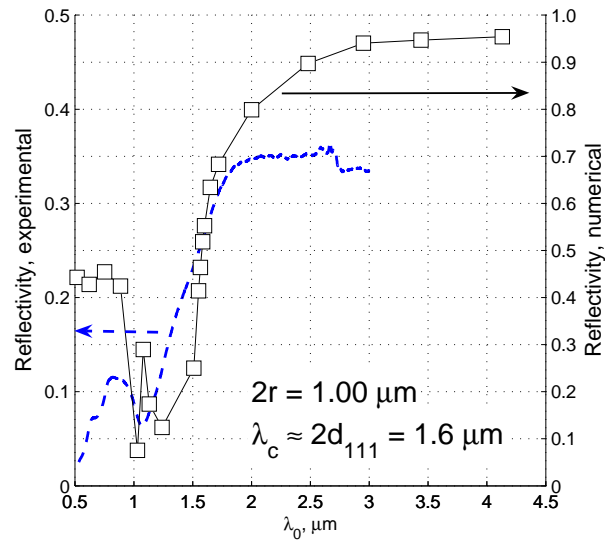


Figure 8.3: Reflectivity spectra of a silica opal ( $2r=1000$  nm) photonic crystal coated with 25-nm tungsten coating. The grid spacing for the numerically-simulated spectrum in this plot is  $\Delta = 82$  nm, and the plotted reflectivity is the average of TE and TM polarizations.

If this explains the difference in measured and predicted cutoff wavelengths, the Bragg law for metal-coated opals, Eq. 8.2, can provide estimate a range of cutoff wavelengths based on the standard deviations of sphere sizes. Yet, the standard deviations of sphere diameter in Table 8.1 yield ranges in cutoff wavelengths of 58 nm, 64 nm, and 146 nm for the smallest to largest spheres, respectively. Since these values are much a

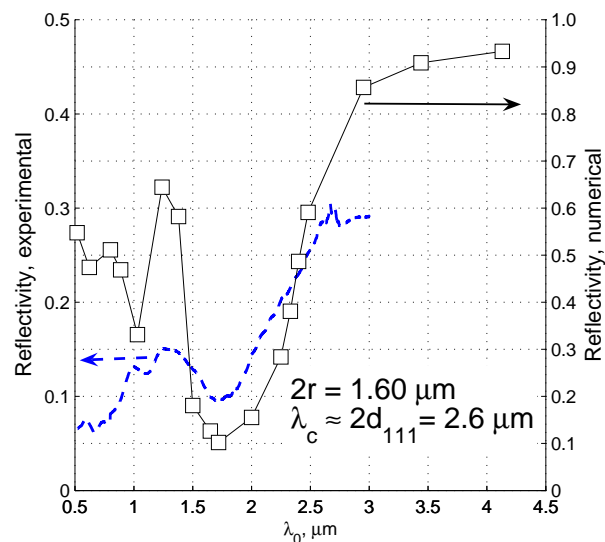


Figure 8.4: Reflectivity spectra of a silica opal ( $2r=1600$  nm) photonic crystal coated with 25-nm tungsten coating. The grid spacing for the numerically-simulated spectrum in this plot is  $\Delta = 109$  nm, and the plotted reflectivity is the average of TE and TM polarizations.

Table 8.2: Cutoff wavelengths  $\lambda_c$  (and corresponding frequencies normalized by lattice constant  $a$ ) of metal-coated silica opal photonic crystals of three different sphere sizes as measured (tungsten coating,  $\lambda_c^{\text{exp}}$ ) and predicted by numerical simulations (silver coating,  $\lambda_c^{\text{TMM}}$ ). Coating thickness:  $t_c=25$  nm.

		$\lambda_c^{\text{exp}}$	$\lambda_c^{\text{TMM}}$
2r=700 nm	$\lambda_c$	1.01 $\mu\text{m}$	< 1.14 $\mu\text{m}$
	$a/\lambda_c$	0.98	> 0.87
2r=1000 nm	$\lambda_c$	1.33 $\mu\text{m}$	< 1.53 $\mu\text{m}$
	$a/\lambda_c$	1.07	> 0.92
2r=1600 nm	$\lambda_c$	2.00 $\mu\text{m}$	< 2.31 $\mu\text{m}$
	$a/\lambda_c$	1.13	> 0.98

smaller than the differences in  $\lambda_c^{\text{exp}}$  and  $\lambda_c^{\text{TMM}}$ , shown in Table 8.2, the range of sphere sizes cannot account for the differences in predicted and measured cutoff frequencies. Hence, the absence of numerical convergence are the primary cause of the differences between  $\lambda_c^{\text{exp}}$  and  $\lambda_c^{\text{TMM}}$ .

For the coated opal photonic crystals to have the thermal emission spectra mentioned above, they must exhibit a complete band gap, that is, that must forbid light propagation in all directions within the crystal. Since silica spheres can self-assemble in the  $\langle 100 \rangle$  of an FCC lattice, their reflectance spectra are worth investigation. Figure 8.5 shows numerical simulations of the reflectivity of the three opal structures for light incident on the photonic crystal in the  $\langle 100 \rangle$  orientation. Since the discretized unit cell is larger than the  $\langle 111 \rangle$  orientation, convergence is more difficult to achieve. Even with coarse sampling, the transition from low to high reflectivity roughly correlates with the Bragg law prediction, which for the  $\langle 100 \rangle$  case is  $\lambda_c^{[100]} = 2a$ . That  $\lambda_c^{[100]} > \lambda_c^{[111]}$ , that is, the cutoff wavelengths for the  $\langle 100 \rangle$  orientation ( $\Gamma$ - $X$  symmetry point) is longer than for the  $\langle 111 \rangle$  orientation, is also consistent with the band diagrams for metal-coated dielectric sphere photonic crystals.<sup>WCZ<sup>+</sup>01,ZLW<sup>+</sup>00</sup>

## 8.5 Conclusions

Numerically computed reflectance spectra of silver-coated silica opal structures have shown cutoff wavelengths in the near-IR above with reflectivity exceeding 93%. These cutoff wavelengths correspond with those found experimentally for tungsten-coated opals of the same geometry, and hence confirm the existence of a photonic band gap effect in these structures. Such photonic crystals have applications in efficient light

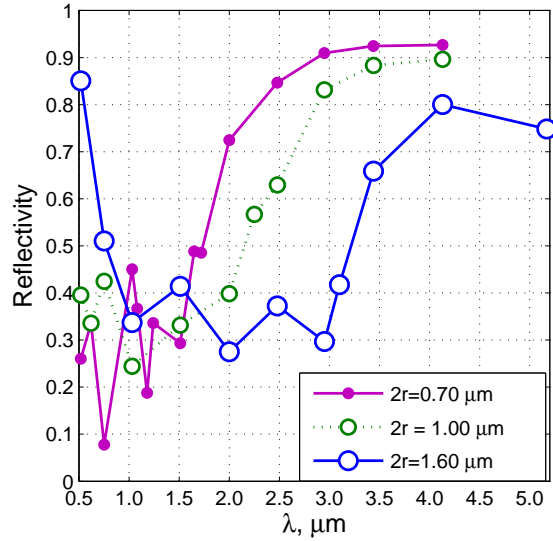


Figure 8.5: Reflectivity spectrum of a silica opal photonic crystal ( $(100)$  orientation) coated with 25-nm silver coating for silica spheres of different radii  $r$ . The mesh spacings, from smallest to largest spheres, are  $\Delta = 71$  nm, 101 nm, and 90 nm. The plotted reflectivity is the average of TE and TM polarization.

sources.

Future work will include numerical modeling of silica opals coated with a metal that best matches the measured reflectivity of the tungsten films and running numerical simulations that adequately sample the smallest features of the coated opal photonic crystal. Since the opal coating thicknesses required for band gap effects are on the order of the metal skin depth, more efficient methods the employ metal spheres are available and should be investigated.<sup>SYM00</sup>

## Chapter 9

### Conclusions and future work

This dissertation provides primary contributions to photonic crystal research concerning their effective refractive index, applications of ultralow index metamaterials, and coated opal photonic crystals with a band gap at near-IR and potentially visible wavelengths.

#### 9.1 Effective refractive index

For a photonic crystal to behave as a metamaterial, its effective refractive index  $n_{\text{eff}}^d$  computed from its dispersion curve must be consistent with the  $n_{\text{eff}}^R$  and  $n_{\text{eff}}^r$ , defined by its reflection and refraction properties, respectively. A photonic crystal mimics the reflection properties of its equivalent homogeneous materials to the extent that the photonic crystal modes resemble plane waves, which are the assumed wave form in the derivation of the Fresnel formulae. For example, this occurs in structures with thin metal wires, but not in dielectric band gap structures with large features, which support strongly-modulated Bloch modes. In general, photonic crystal modes resemble plane waves in the long-wavelength limit, or in the cases studied here, when the inclusions are very small compared to the wavelength, while the unit cell need only be smaller than approximately half the wavelength.

A popular application of photonic band gap materials with an effective index is a slab with  $n_{\text{eff}}^d = -1$ . A homogeneous material with this refractive index images sources as a lens does, with notable exceptions that the magnification is unity and the image distance does not depend on the distance between the slab and the object. However, the performance of such dielectric photonic band gap materials does not match those of their equivalent homogeneous slabs. In the example considered, the photonic crystal

does not have the subwavelength resolving power as its equivalent homogeneous slab. While such structures may have useful applications, the effective refractive index defined by the dispersion curve does not reliably predict their performance as it does for photonic crystals with eigenmodes resembling plane waves.

This difference between photonic crystals with strongly-modulated Bloch modes and those with plane-wave-like modes suggests the need to quantify the validity of  $n_{\text{eff}}^d$  for photonic crystals as a function of inclusion size and refractive index contrast. For example, one method is to quantify the difference in angular-dependent reflectivity between the photonic crystal and its equivalent homogeneous slab with index  $n_{\text{eff}}^d$ .

## 9.2 Ultralow index metamaterials

Two-dimensional arrays of thin wires were shown to act as ultralow index metamaterials (ULIMs): low-loss metamaterial with the real part of their effective refractive index less than one ( $\text{Re}(n_{\text{eff}} < 1)$ ) at visible and near-IR wavelengths. Ultralow index metamaterial waveguides have applications in integrated optical components.

Preliminary designs of ULIM devices, such as the waveguides and lenses discussed here, can be obtained quickly by modeling their equivalent homogeneous structures. More rigorous methods are needed only to optimize performance.

Numerical simulations of one-dimensional silver-dielectric stacks showed that for such structures to act as an ULIM at visible or near-IR wavelengths, the silver films would be less than 20-nm thick. At such dimensions the refractive index of silver deviates from its bulk value because of both purely geometric effects and inhomogeneities caused by fabrication conditions. Such deviations can drastically effect the performance of a metamaterial. This effect is an important consideration for photonic crystals with complete band gaps at visible wavelengths, discussed in Chapter 8, as among the most promising of such geometries are synthetic opals coated with a thin metal film.

Optimizing the waveguide performance at selected visible and near-IR wavelengths involved changing the silver-wire fill-factor, and hence the metamaterial's effective refractive index. This process demonstrates how two and three-dimensional metamaterials can be engineered to have a specific refractive index at a specific wavelength. Unlike similar cases involving one-dimensional structures that exhibit form-birefringence

in the long-wavelength limit, higher-dimensional periodic structures behave as metamaterials at wavelengths just slightly longer than twice the unit cell length.

Future work should involve designing three-dimensional ULIMs that can be fabricated using existing scalable methods, for example, synthetic opals created via self-assembly and coated with metal by atomic layer deposition. Valid numerical simulations of such structures using the methods presented here will require more powerful computers and/or more advanced modeling methods.

### 9.3 Coated-opal photonic crystals

Atomic layer deposition rates of alumina on silica opals were shown to match the alumina deposition rates on planar substrates when the coating thickness is less than 10% of the opal sphere radius. Such control of coating thicknesses allows for the precise engineering of photonic band gap structures required to optimize them for specific applications.

As an adhesion layer, alumina allows for the conformal deposition of metals, such as tungsten, on silica opals. Numerical simulations of metal-coated synthetic opals were shown to exhibit a photonic band gap effect consistent with experimental measurements of tungsten-coated opals. These structures have potential applications as efficient lighting and thermophotovoltaic devices.

Subsequent work should include numerical modeling of silica opals coated with a metal that best matches the measured reflectivity of the tungsten films. As with the opal ULIMs, more accurate numerical simulations using the transfer-matrix method that adequately sample the smallest features of the coated opal photonic crystal will require more computational memory. Since the opal coating thicknesses required for band gap effects are on the order of the metal skin depth, more efficient methods should be investigated. Further research should also explore the promising applications of tungsten-coated opals in lighting and thermophotovoltaic applications.

## Bibliography

- [AAD00] O Acher, A L Adenot, and F Duverger. Fresnel coefficients at an interface with a lamellar composite material. Phys. Rev. B, 62(20):13748–13756, 2000.
- [Ans01] Ansoft Corporation, Pittsburgh, PA. Ansoft HFSS Version 8.0.25, (2001).
- [AO96] Ilsin An and Kyekyun Oh. Optical properties of silver thin films: three-parameter spectroscopic ellipsometry studies. J. Kor. Opt. Soc., 29:370–376, 1996.
- [Asp82] D E Aspnes. Local-field effects and effective-medium theory: A microscopic perspective. Am J. Phys., 50:704–709, 1982.
- [Att99] David Attwood. Soft X-Rays and Extreme Ultraviolet Radiation: Principles and Applications. Cambridge University Press, 1999.
- [AYLK04] S M Abrarov, Sh U Yuldasheva, S B Leeb, and T W Kanga. Suppression of the green photoluminescence band in zno embedded into porous opal by spray pyrolysis. J. Lumin., 109:25–29, 2004.
- [BB24] W H Bragg and W L Bragg. X Rays and Crystal Structure. G. Bell and Sons, Ltd., London, 4 edition, 1924.
- [BDM82] J M Bell, G H Derrick, and R C McPhedran. Diffraction gratings in the quasi-static limit. Opt. Act., 29:1475–1489, 1982.
- [BJ98] Kurt Busch and Sajeev John. Photonic band gap formation in certain self-organizing systems. Phys. Rev. E, 58:3896–3908, 1998.
- [BM95] E R Broan and O B McMahan. Large electromagnetic stop bands in metallodielectric photonic crystals. App. Phys. Lett., 67(15):2138–2140, 1995.
- [BML99] H Míguez A Blanco, F Meseguer, and C López. Bragg diffraction from indium phosphide infilled fcc silica colloidal crystals. Phys. Rev. B, 59(3):1563–1566, 1999.
- [BMS<sup>+</sup>04] A Berrier, M Mulot, M Swillo, M Qiu, L Thyln, A Talneau, and S Anand. Negative refraction at infrared wavelengths in a two-dimensional photonic crystal. Phys. Rev. Lett., 93:073902(4), 2004.

- [BPMW95] P M Bell, J B Pendry, L Martín Moreno, and A J Ward. A program for calculating photonic band structures and transmission coefficients of complex structures. Comp. Phys. Comm., 85:306–322, 1995.
- [Bra54] R N Bracewell. Analogues of an ionized medium. Wireless Engineer, 31:320–326, 1954.
- [Bro53] J Brown. Artificial dielectrics having refractive indices less than unity. Proc. IEE, 100C:51–62, 1953.
- [Bro60] J Brown. Artificial dielectrics. Progress in Dielectrics, 2:193–225, 1960.
- [Bro03] Mark L Brongersma. Nanoshells: gifts in a gold wrapper. Nature Mat., 2:296–297, May 2003.
- [BW80] M Born and E Wolf. Principles of Optics. Cambridge University Press, 6 edition, 1980.
- [CCI01] C Caloz, C C Chang, and T Itoh. Full-wave verification of the fundamental properties of left-handed materials in waveguide configurations. J Appl Phys, 90(11):5483–5486, December 2001.
- [CGMA03] D Comoretto, R Grassi, F Marabelli, and LC Andreani. Growth and optical studies of opal films as three-dimensional photonic crystals. Mat. Sci. Eng., 23:61–65, 2003.
- [CJN04] A A Chabanov, Y Jun, and D J Norris. Avoiding cracks in self-assembled photonic band-gap crystals. App. Phys. Lett., 84(18):3573–3575, 2004.
- [Com04] Comsol Corporation Burlington, MA. Femlab 3.1, 2004.
- [CSVZ01] A Cucinotta, S Selleri, L Vincetti, and M Zoboli. Impact of the cell geometry on the spectral properties of photonic crystal structures. Applied Physics B- Lasers and Optics, 73(5-6):595–600, 2001.
- [CSVZ02] A Cucinotta, S Selleri, L Vincetti, and M Zoboli. Perturbation analysis of dispersion properties in photonic crystal fibers through the finite element method. Journal of Lightwave Technology, 20(8):1433–1442, August 2002.
- [CVG<sup>+</sup>91] Petr Chýlek, Gordon Videen, D J Wally Geldart, J Steven Dobbie, and H C William Tso. Comments on the optical constants of metals and an introduction to the data for several metals. In Michael I Mishchenko, Joop W Hovenier, and Larry D Travi, editors, Light scattering by nonspherical particles: theory, measurements, and applications, pages 273–308. Academic Press, 1991.
- [DB94] Jonathan P Dowling and Charles M Bowden. Anomalous index of refraction in photonic bandgap materials. J. Mod. Opt., 41:345–351, 1994.
- [Dod84] Marilyn J. Dodge. Refractive properties of magnesium fluoride. App. Opt., 23:1980–1984, 1984.

- [Duk04] Certified particle size standards. Bulletin 92 O, Duke Scientific Corporation, 2004.
- [EG03] J W Elam and S M George. Growth of  $\text{ZnO}/\text{Al}_2\text{O}_3$  alloy films using atomic layer deposition techniques. *Chem. Mater.*, 15:1020–1028, 2003.
- [EKSB<sup>+</sup>00] I El-Kady, MM Sigalas, R Biswas, KM Ho, and CM Soukoulis. Metallic photonic crystals at optical wavelengths. *Phys. Rev. B*, 63:15299–15302, 2000.
- [ENGG01] J W Elam, C E Nelson, R K Grubbs, and S M George. Nucleation and growth during tungsten atomic layer deposition on  $\text{SiO}_2$  surfaces. *Thin Sol. Films*, 386:41–52, 2001.
- [ETS<sup>+</sup>02] S Enoch, G Tayeb, P Sabouroux, N Guerin, and P Vincent. A metamaterial for directive emission. *Phys. Rev. Lett.*, 89:213902, 2002.
- [EWS<sup>+</sup>03] J W Elam, C A Wilson, M Schuisky, Z A Sechrist, and S M George. Improved nucleation of tin atomic layer deposition films on silk low-k polymer dielectric using an  $\text{Al}_2\text{O}_3$  atomic layer deposition adhesion layer. *J. Vac. Sci. Technol. B*, 21(3):1099–1107, 2003.
- [FB97] D Felbacq and G Bouchitt. Homogenization of a set of parallel fibres. *Waves Random Media*, 7:245–256, 1997.
- [Fel02] D Felbacq. Noncommuting limits in homogenization theory of electromagnetic crystals. *J. Math. Phys.*, 43:52–55, 2002.
- [FES03] S Foteinopoulou, E N Economou, and C M Soukoulis. Refraction in media with a negative refractive index. *Phys. Rev. Lett.*, 90:107402(4), 2003.
- [FLEK<sup>+</sup>02] JG Fleming, SY Lin, I El-Kady, R Biswas, and KM Ho. All-metallic three-dimensional photonic crystals with a large infrared bandgap. *Nature*, 417:52–55, 2002.
- [GET00] Boris Gralak, Stefan Enoch, and Grard Tayeb. Anomalous refractive properties of photonic crystals. *J. Opt. Soc. Am. A*, 17:1012–1020, 2000.
- [GKK<sup>+</sup>01] V G Golubev, V A Kosobukin, D A Kurdyukov, A V Medvedev, and A B Pevtsov. Photonic crystals with tunable band gap based on filled and inverted opalsilicon composites. *Semiconductors*, 35(6):680–683, 2001.
- [GMTV98] G Guida, D Maystre, G Tayeb, and P Vincent. Mean-field theory of two-dimensional metallic photonic crystals. *J. Opt. Soc. Am. B*, 15:2308–2315, 1998.
- [GNV02a] N Garcia and M Nieto-Vesperinas. Is there an experimental verification of a negative index of refraction yet? *Opt. Lett.*, 27:885, 2002.
- [GNV02b] N Garcia and M Nieto-Vesperinas. Left-handed materials do not make a perfect lens. *Phys. Rev. Lett.*, 88:2070703, 2002.

- [GPX02] N Garcia, E V Ponizovskaya, and John Q Xiao. Zero permittivity materials: Band gaps at the visible. App. Phys. Lett., 80:1120–1122, 2002.
- [Gup71] K C Gupta. Narrow-beam antennas using an artificial dielectric medium with permittivity less than unity. Electronics Letters, 7, 1971.
- [Hal01] Naomi Halas. Tiny but mighty. OE Magazine, 1(12):296–297, December 2001.
- [HEO03] K Halterman, J M Elson, and P L Overfelt. Characteristics of bound modes in coupled dielectric waveguides containing negative index media. Optics Express, 11(6):521–529, March 2003.
- [HH04] A Husakou and J Herrmann. Superfocusing of light below the diffraction limit by photonic crystals with negative refraction. Opt. Exp., 12:6491–6495, 2004.
- [HKA99] P Halevi, A A Krokhin, and J Arriaga. Photonic crystal optics and homogenization of 2d periodic composites. Phys. Rev. Lett., 82:719–722, 1999.
- [HKBJ03] Christopher L Holloway, Edward F Kuester, and James Baker-Jarvis. A double negative (dng) composite medium composed of magnetodielectric spherical particles embedded in a matrix. IEEE Trans. Ant. Prop., 51:2596–2603, 2003.
- [HS62] Z Hashin and S Shtrikman. A variational approach to the theory of effective magnetic permeability of multiphase materials. J. Appl. Phys., 33:3125–3131, 1962.
- [Jac75] John David Jackson. Classical Electrodynamics. John Wiley and Sons, 2 edition, 1975.
- [JJ01] Steven G. Johnson and J. D. Joannopoulos. Block-iterative frequency-domain methods for maxwell’s equations in a planewave basis. Opt. Express, 8(3):173–190, 2001.
- [JMW95] John D Joannopoulos, Robert D Meade, and Joshua N Winn. Photonic Crystals. Princeton U. Press, 1995.
- [Joh87] Sajeev John. Strong localization of photons in certain disordered dielectric structures. Phys. Rev. Lett., 58:2486–2489, 1987.
- [JYZ02] D Y Jeong, Y H Ye, and Q M Zhang. Effective optical properties associated with wave propagation in photonic crystals of finite length along the propagation direction. J. Appl. Opt., 92:4194–4200, 2002.
- [KFG00] J W Klaus, S J Ferro, and S M George. Atomic layer deposition of tungsten using sequential surface chemistry with a sacrificial stripping reaction. Thin Sol. Films, 360:145–153, 2000.

- [KHA02] A A Krokhin, P Halevi, and J Arriaga. Long-wavelength limit (homogenization) for two-dimensional photonic crystals. Phys. Rev. B, 65:115208(17), 2002.
- [KNS<sup>+</sup>03] J S King, C W Neff, C J Summers, W Park, Blomquist, E Forsythe, and D Morton. High-filling-fraction inverted zns opals fabricated by atomic layer deposition. App. Phys. Lett., 83(13):2566–2568, 2003.
- [Lak96] A Lakhtakia, editor. Selected Papers on Linear Optical Composite Materials, volume MS 120. SPIE Optical Engineering Press, 1996.
- [LEKH<sup>+</sup>03] Zhi-Yuan Li, I El-Kady, Kai-Ming Ho, SY Lin, and JG Fleming. Photonic band gap effect in layer-by-layer metallic photonic crystals. J. Appl. Phys., 93:38–42, 2003.
- [LFEK03] SY Lin, JG Fleming, and I El-Kady. Highly efficient light emission at  $\lambda = 1.5 \mu\text{m}$  by a three-dimensional tungsten photonic crystal. Opt. Lett., 28:1683–1685, 2003.
- [LH91] David W Lynch and W R Hunter. Comments on the optical constants of metals and an introduction to the data for several metals. In Edward D. Palik, editor, Handbook of Optical Constants of Solids, pages 275–368. Academic Press, 1991.
- [LH98] Philippe Lalanne and Jean-Paul Hugonin. High-order effective medium theory of subwavelength gratings in classical mounting: application to volume holograms. J. Opt. Soc. Am. A, 15(7):1843–1851, 1998.
- [LH03] Philippe Lalanne and Mike Hutley. Artificial media optical properties-subwavelength scale. In Ronald Driggers, editor, Encyclopedia of Optical Engineering, pages 62–71. Marcel Dekker, 2003.
- [LHWJ96] Shawn-Yu Lin, V M Hietala, Li Wang, and E D Jones. Highly dispersive photonic band-gap prism. Opt. Lett., 21:1771–1773, 1996.
- [Li02] Zhi-Yuan Li. Modified thermal radiation in three-dimensional photonic crystals. Phys. Rev. B, 66:241103, 2002.
- [Lid] David R Lide, editor. CRC Handbook of Chemistry and Physics, Internet Version 2005. CRC PRes, Boca Raton, FL. <<http://www.hbcnetbase.com>>.
- [LL03] Zhi-Yuan Li and Lan-Lan Lin. Evaluation of lensing in photonic crystal slabs exhibiting negative refraction. Phys. Rev. B, 68:245110, 2003.
- [LLL96] Philippe Lalanne and Dominique Lemerrier-Lalanne. On the effective medium theory of subwavelength periodic structures. J. Mod. Opt., 43(10):2063–2085, 1996.
- [LNCJ04] Chiyun Luo, Arvind Narayanaswamy, Gang Chen, and J D Joannopoulos. Thermal radiation from photonic crystals: A direct calculation. Phys. Rev. Lett., 93:213905, 2004.

- [LTOSSD02] F López-Tejiera, T Ochiai, K Sakoda, and J Sánchez-Dehesa. Symmetry characterization of eigenstates in opal-based photonic crystals. Phys. Rev. B., 652, 2002.
- [LVM<sup>+</sup>97] C López, L Vázquez, F Meseguer, R Mayoral, M Oca na, and H Míguez. Photonic crystal made by close packing  $\text{SiO}_2$  submicron spheres. Mat. Sci. Eng., 22(3):399–404, 1997.
- [LZ00] Zhi-Yuan Li and Zhao-Qing Zhang. Fragility of photonic band gaps in inverse-opal photonic crystals. Phys. Rev. B, 62:1516–1519, 2000.
- [ME04] Daniel Maystre and Stefan Enoch. Perfect lenses made with left-handed materials: Alice’s mirror? J. Opt. Soc. Am., 21:122–131, 2004.
- [MEG<sup>+</sup>03] T M Mayera, J W Elamb, S. M. George, P G Kotula, and R S Goeke. Atomic-layer deposition of wear-resistant coatings for microelectromechanical devices. Appl. Phys. Lett., 82:28832885, 2003.
- [MKA<sup>+</sup>03] Stefan A Maier, Pieter G Kik, Harry A Atwater, Sheffer Meltzer, Elad Harel, Bruce Koel, and Ari A G Requicha. Local detection of electromagnetic energy transport below the diffraction limit in metal nanoparticle plasmon waveguides. Nature Materials, 2:229–232, April 2003.
- [Mor99] Alexander Moroz. Three-dimensional complete photonic-band-gap structures in the visible. Phys. Rev. Lett., 83(25):5274–5277, 1999.
- [NAM<sup>+</sup>97] D. J. Norris, E G Arlinghaus, L Meng, R Heiny, and L E Scriven. Opaline photonic crystals: How does self-assembly work? Adv. Mat., 16(16):1393–1399, 1997.
- [Not00] M Notomi. Theory of light propagation in strongly modulated photonic crystals: Refraction-like behavior in the vicinity of the photonic bandgap. Phys. Rev. B, 62:10696–10705, 2000.
- [NT02] I S Nefedov and S A Tretyakov. Waveguide containing a backward-wave slab. e-print in arXiv:cond-mat/0211185 v1, 2002. at <http://arxiv.org/pdf/cond-mat/0211185>.
- [OK96] S M George A W Ott and J W Klaus. Surface chemistry for atomic layer growth. J. Phys. Chem, 100:13121–13131, 1996.
- [OLB<sup>+</sup>83] M A Ordal, L L Long, R J Bell, S E Bell, R R Bell, R W Alexander Jr., and C A Ward. Optical properties of metals al, co, cu, au, fe, pb, ni, pd, pt, ag, ti, and w in the infrared and far infrared. App. Opt., 22:1099–1119, 1983.
- [OMK<sup>+</sup>96] A W Ott, K C McCarley, J W Klaus, J D Way, and S M George. Atomic layer controlled deposition of  $\text{Al}_2\text{O}_3$  films using binary reaction sequence chemistry. Appl. Surf. Sci., 107:1–270, 1996.

- [OTS<sup>+</sup>96] E Özbay, B Temelkuran, M Sigalas, G Tuttle, C M Soukoulis, and K M Ho. Defect structures in metallic photonic crystals. App. Phys. Lett., 69(25):3797–3799, 1996.
- [Pal91] Edward D. Palik, editor. Handbook of Optical Constants of Solids. Academic Press, 1991.
- [Par05] Wounjhang Park. Modeling of photonic crystals. In Michael Rietz and Wolfram Schommers, editors, Handbook of Theoretical and Computational Nanotechnology, volume 10. Am. Sci. Pub., 2005. To be published.
- [PB03] A C Peacock and N G R Broderick. Guided modes in channel waveguides with a negative index of refraction. Optics Express, 11(20):2502–2510, October 2003.
- [PE02] A L Pokrovsky and A L Efros. Electrodynamics of metallic photonic crystals an the problem of left-handed materials. Phys. Rev. Lett., 89:093901, 2002.
- [Pen00] J B Pendry. Negative refraction makes a perfect lens. Phys. Rev. Lett., 85:3966, 2000.
- [Pen03] Focus issue: Negative refraction and metamaterials. Optics Express, 11(7):639–838, 2003.
- [PHRS98] J B Pendry, A J Holden, D J Robbins, and W J Stewart. Low frequency plasmons in thin-wire structures. J. Phys. Condens. Matter, 10:4785–4809, 1998.
- [PLVS03] Patanjali V Parimi, Wentai T Lu, Plaranta Vodo, and Srtinivas Sridhar. Imaging by flat lens using negative refraction. Nature, 426:404, 2003.
- [PM92] J B Pendry and A MacKinnon. Calculation of photon dispersion relations. Phys. Rev. Lett., 69:2772–2775, 1992.
- [QLKA98] M Quinten, A Leitner, J R Krenn, and F R Aussenegg. Electromagnetic energy transport via linear chains of silver nanoparticles. Opt Lett, 23(17):1331–1333, 1998.
- [QTSJ03] Min Qiu, Laws Thylén, Marcin Swillo, and Bozena Jaskorzynska. Wave propagation through a photonic crystal in a negative phase refractive-index region. IEEE J. Sel. Top. Quantum Electron., 9:106–110, 2003.
- [RAM<sup>+</sup>92] W M Robertson, G Arjavalingam, R D Meade, K D Brommer, A M Rappe, and J D Joannopolous. Measurement of photonic band structure in a two-dimensional periodic dielectric array. Phys. Rev. Lett., 68:2023–2025, 1992.
- [RBGT03] Alessandro Ruggie, Jill S. Becker, Roy G. Gordon, and Sarah H Tolbert. Tungsten nitride inverse opals by atomic layer deposition. Nano Lett., 3(9):1293–1297, 2003.

- [RCGV<sup>+</sup>99] A Reynolds, D Cassagne, F J Garca-Vidal, C Jouanin, and J Snchez-Dehesa. Spectral properties of opal-based photonic crystals having a  $\text{SiO}_2$  matrix. Phys. Rev. B, 60:11422–11426, 1999.
- [RCJA01] A L Reynolds, D Cassagne, C Jouanin, and J M Arnold. Optical properties of bare, sintered and coated opal-based photonic crystals. Synth. Met., 116:453–456, 2001.
- [Rei73] A Reisinger. Characteristics of optical guided modes in lossy waveguides. App. Opt., 12(5):1015–1025, May 1973.
- [Rey00a] Andrew L. Reynolds. Modelling of photonic band gap materials for mm-wave & optical applications. PhD thesis, U. of Glasgow, 2000.
- [Rey00b] Andrew L. Reynolds. Translight Software. Optoelectronics Research Group, U. of Glasgow, 2000.
- [RMC93] John R Reitz, Frederick J Milford, and Robert W Christy. Foundations of Electromagnetic Theory. Addison-Wesley, 4 edition, 1993.
- [Rot62] Walter Rotman. Plasma simulation by artificial dielectrics and parallel-plate media. IRE Trans. Antennas Propag., AP10:82–95, 1962.
- [RPGT05] Alessandro Ruggie, Jin-Seong Park, Roy G. Gordon, and Sarah H Tolbert. Tantalum(v) nitride inverse opals as photonic structures for visible wavelengths. J. Phys. Chem., 109:3764–3771, 2005.
- [RQX<sup>+</sup>05] Zhichao Ruan, Min Qiu, Sanshui Xiao, Sailing He, and Lars Thyln. Coupling between plane waves and bloch waves in photonic crystals with negative refraction. Phys. Rev. B, 71:045111, 2005.
- [Ryt56] S M Rytov. Electromagnetic properties of a finely stratified medium. Sov. Phys. JETP, 2:466–475, 1956.
- [Sak97] Kazuaki Sakoda. Numerical analysis of the interference patterns in the optical transmission spectra of a square photonic lattice. J. Opt. Soc. Am. B, 14:1961–1965, 1997.
- [Sak01] Kazuaki Sakoda. Optical Properties of Photonic Crystals. Springer, 2001.
- [SCHS95] M M Sigalas, Cy Chan, KM Ho, and CM Soukoulis. Metallic photonic band-gap materials. Phys. Rev. B, 52:11744–11751, 1995.
- [SCSH99] G. Subramaniaa, K. Constant, R Biswas M M Sigalas, and K-M Ho. Optical photonic crystals fabricated from colloidal systems. App. Phys. Lett., 74:3933–3935, 1999.
- [SFH<sup>+</sup>at] Z A Sechrist, F H Fabreguette, O Heintz, T M Phung, D C Johnson, and S M George. Optimization and structural characterization of  $\text{W}/\text{Al}_2\text{O}_3$  nanolaminates grown using atomic layer deposition techniques. 17(13):3475–3485, Chem. Mat.

- [Sie99] D Sievenpiper. High-impedance electromagnetic surfaces. PhD thesis, Univ. California at Los Angeles, Dept. Elec. Eng., 1999.
- [Sih02] Ari H Sihvola. How strict are theoretical bounds for dielectric properties of mixtures? IEEE Trans. Geo. and Rem. Sens., 40:880–886, 2002.
- [SJOH98] S. L. Westcott S. J. Oldenburg, R. D. Averitt and N. J. Halas. Nanoengineering of optical resonances. Chem. Phys. Lett., 288:243–247, 1998.
- [SL83] Allan W Snyder and John D Love. Optical Waveguide Theory. Chapman and Hall, 2 edition, 1983.
- [Smi] D R Smith. The duke home page for research on negative refraction. [http://www.ee.duke.edu/drsmith/nim\\_pubs.htm](http://www.ee.duke.edu/drsmith/nim_pubs.htm).
- [SP02] Brian T Schwartz and R Piestun. Total external reflection at optical wavelengths. In OSA Trends in Optics and Photonics (TOPS) Vol. 75, Diffractive Optics and Micro-Optics, OSA Technical Digest, Postconference Edition, pages 175–177. Optical Society of America, Washington DC, 2002.
- [SP03] Brian T Schwartz and Rafael Piestun. Total external reflection from metamaterials with ultralow refractive index. J. Opt. Soc. Am. B, 20(12):2448–2453, 2003.
- [SP04a] B T Schwartz and R Piestun. Waveguiding in air by total external reflection from ultra-low index metamaterials. App. Phys. Lett., 85(1):1–3, 2004.
- [SP04b] B T Schwartz and R Piestun. Waveguiding light in air with ultralow index metamaterials. Proc. SPIE Int. Soc. Opt. Eng., pages 5515–27, 2004.
- [SP05a] B T Schwartz and R Piestun. Dynamic properties of finite photonic crystals with negative effective band index. In Integrated Photonics Research and Applications/Nanophotonics for Information Systems Topical Meetings on CD-ROM, page NThA4. Optical Society of America, Washington DC, 2005.
- [SP05b] B T Schwartz and R Piestun. How effective is the effective refractive index? In Conference on Lasers and Electro-Optics/Quantum Electronics and Laser Science and Photonic Applications, Systems and Technologies 2005, page QFA5. Optical Society of America, Washington DC, 2005.
- [SP05c] Brian T Schwartz and Rafael Piestun. Dynamic properties of photonic crystals and their effective refractive index. J. Opt. Soc. Am. B, 22:2018–2026, 2005.
- [SSL<sup>+</sup>ed] Z A Sechrist, B T Schwartz, J H Lee, F H Fabreguette, J A McCormick, R Piestun, W Park, and S M George. Model system for modifying of an opal photonic crystal using atomic layer deposition. to be published.

- [SSMS02] D R Smith, S Schultz, P Markos, and C M Soukoulis. Determination of effective permittivity and permeability of metamaterials from reflection and transmission coefficients. Phys. Rev. B, 65:195104(5), 2002.
- [SSS01] R A Shelby, D R Smith, and S Schultz. Experimental verification of a negative index of refraction. Science, 292:77–79, 2001.
- [SYM00] N Stefanou, V Yannopoulos, and A Modinos. Multem2: A new version of the program for transmission and band-structure calculations of photonic crystals. Comp. Phys. Comm., 132:189–196, 2000.
- [Vau89] J M Vaughan. The Fabry-Perot Interferometer. Adam Hilger, 1989.
- [VDN00] Y A Vlasov, M Deutsch, and D J Norris. Single-domain spectroscopy of self-assembled photonic crystals. Appl. Phys. Lett., 76(12):1627–1629, 2000.
- [Ves67] V G Veselago. Properties of materials having simultaneously negative values of the dielectric ( $\epsilon$ ) and the magnetic ( $\mu$ ) susceptibilities. Sov. Phys. Sol. St., 8:2854–2856, 1967.
- [Ves68] V G Veselago. The electrodynamics of substances with simultaneously negative values of  $\epsilon$  and  $\mu$ . Sov. Phys. Sol. St., 10:509–514, 1968.
- [vFJSD<sup>+</sup>04] Georg von Freymann, Sajeev John, Martin Schulz-Dobrick, Evangelios Vekris, Nicolas Tétreault, Sean Wong, Vladimir Kitaev, and Geoffrey A Ozin. Tungsten inverse opals: The influence of absorption on the photonic band structure in the visible region. Appl. Phys. Lett., 84:224–226, 2004.
- [VK97] O D Velev and E W Kaler. Structured porous materials via colloidal crystal templating: From inorganic oxides to metals. Adv. Mat., 12:531–534, 1997.
- [VWV02] P M Valanju, R M Walser, and A P Valanju. Wave refraction in negative-index media: always positive and very inhomogeneous. Phys. Rev. Lett., 88:187401, 2002.
- [WCZ<sup>+</sup>01] Zhenlin Wang, C T Chan, Weiyi Zhang, Naiben Ming, and Ping Sheng. Three-dimensional self-assembly of metal nanoparticles: Possible photonic crystal with a complete gap below the plasma frequency. Phys. Rev. B., 64:113108, 2001.
- [WRK05] X Wang, Z F Ren, and K Kempa. Improved superlensing in two-dimensional photonic crystals with a basis. App. Phys. Lett., 86:061105, 2005.
- [WSB68] Arthur Fink Werner Stöber and Ernst Bohn. Controlled growth of monodisperse silica spheres in the micron size range. J. Coll. Int. Sci., 26(1):62–69, 1968.

- [WVV01] Rodger M Walser, Alaka P Valanju, and Prashant M Valanju. Comment on ‘extremely low frequency plasmons in metallic mesostuctures’. Phys. Rev. Lett., 87:9701, 2001.
- [Yab87] Eli Yablonovitch. Inhibited spontaneous emission in solid-state physics and electronics. Phys. Rev. Lett., 58:2059–2062, 1987.
- [YG89] Eli Yablonovitch and T J Gmitter. Photonic band structure: The face-centered-cubic case. Phys. Rev. Lett., 63:1950–1953, 1989.
- [YY84] Amnon Yariv and Pochi Yeh. Optical Waves in Crystals. John Wiley and Sons, 1984.
- [ZLW+00] W. Y. Zhang, X Y Lei, Z L Wang, DG Zheng, W Y Tam, C T Chan, and Ping Sheng. Robust photonic band gap from tunable scatterers. Phys. Rev. B., 84:2853–2856, 2000.

## Appendix A

### Convergence of numerical predictions of first-order opal Bragg maxima

The numerical simulations predictions of the wavelength corresponding to the peak Bragg reflectivity,  $\lambda_{\max}$ , for an opal photonic crystal have two sources of error: wavelength spacing, and sampling the unit cell. The maximum wavelength resolution in a typical data set was 1 nm. For each simulation Translight<sup>Rey00a, BPMW95</sup> uses equally spaced sampling in the  $x$ ,  $y$ , and  $z$  directions. For the  $\langle 111 \rangle$  propagation direction of an f.c.c. lattice with unit cell of cube side  $a$ , the distance between planes of spheres, and dimension of the discretized cell in the  $z$  direction, is  $cell_z = d_{111} = \frac{a}{\sqrt{3}}$ . Accordingly,  $cell_x = a\sqrt{\frac{3}{2}}$  and  $cell_y = \frac{a}{\sqrt{2}}$ .<sup>Rey00a</sup>

To accurately model the coated opal structure, the sampling spacing should be less than half the smallest feature to satisfy the Nyquist condition. In this case, the smallest feature is the coating, which can be as thin as  $t_c = 5$  nm for the experiments and simulations presented here. For the  $d_{111} = 216$  nm planar spacing in the numerical simulations, achieving  $\Delta = \frac{t_c}{2}$  would require 92 samples between planes of spheres. As mentioned in Chapter 7, computer memory limited the simulations to a maximum of 14 sample points along the  $\langle 111 \rangle$  direction.

Figures A.1-A.4 show the effect of decreasing the discretization spacing on the predicted band gap location or reflection maxima for the bare opals and thpse with selected alumina coatings ranging from 4.7 to 33.3 nm thick. Since  $d_{111} = 216$  nm, the  $\Delta$  values of 27 nm, 22 nm, 18 nm, and 15 nm shown in these figured correspond to  $\Delta = \frac{d_{111}}{8}$ ,  $\Delta = \frac{d_{111}}{10}$ ,  $\Delta = \frac{d_{111}}{12}$ , and  $\Delta = \frac{d_{111}}{14}$  respectively. The  $\lambda_{\max}$  presented in Chapter 7 are based on simulations with  $\Delta = \frac{d_{111}}{8}$ .

In each of figure, simulations with finer sampling predict peak reflectivities at

shorter wavelengths than those with coarse sampling. A typical shift is  $\Delta\lambda_{\max}=-3$  nm, which in terms of normalized frequency is  $\Delta\Omega_{\max}=+0.003$  for wavelength ranges considered here. Since the magnitude of these shifts are similar for different coating thicknesses, correcting for the error caused by the coarse sampling will only shift the curves in Fig. 7.1 and Fig. 7.2 down. It will not significantly change their slopes, which are used to determine the validity of the using alumina planar atomic layer deposition rate on the opals.

Since the smallest sample spacings are larger half the coatings thicknesses, there is no reason to think that the shifts considered above are a lower limit for  $\lambda_{\max}$ . The spectra could conceivably continue to shift as discretization spacing  $\Delta$  decreases.

To establish a lower limit I compared Translight's predictions of the bare silica opal spectra to those in Ref. LTOSSD02 and Ref. RCGV<sup>+</sup>99 that employed a plane wave expansion method.<sup>JMW95</sup> While a silica opal photonic crystal does not have the refractive index contrast required for a complete photonic band gap, it does exhibit a band gap for light propagating in the  $\langle 111 \rangle$  ( $\Gamma$ - $L$ ) direction.<sup>RCGV<sup>+</sup>99,LTOSSD02</sup> Close examination of the band structure published in Ref. LTOSSD02<sup>1</sup> shows the band gap to occur in the normalized frequency range  $0.635 < \Omega < 0.669$ . Translight simulations of this photonic crystal with  $\Delta = \frac{d_{111}}{8}$  predicts a band gap in the the normalized frequency range  $0.628 < \Omega < 0.662$ , which corresponds to a  $\Delta\Omega_{\max} = +0.005$  deviation from the actual band gap location. For the opals considered in Chapter 7, the unit cell is  $a=374.1$  nm, and this deviation in normalized frequency corresponds to  $\Delta\lambda_{\max} = -5$  nm, the lower bound on the  $\lambda_{\max}$  values shown in Fig. 7.1 and Fig. 7.2.

---

<sup>1</sup> This simulation assumed a refractive index of  $n=1.4505$  for the silica spheres. While those in Chapter 7 used  $n=1.43$ , this difference should be negligible for establishing a lower error bound.

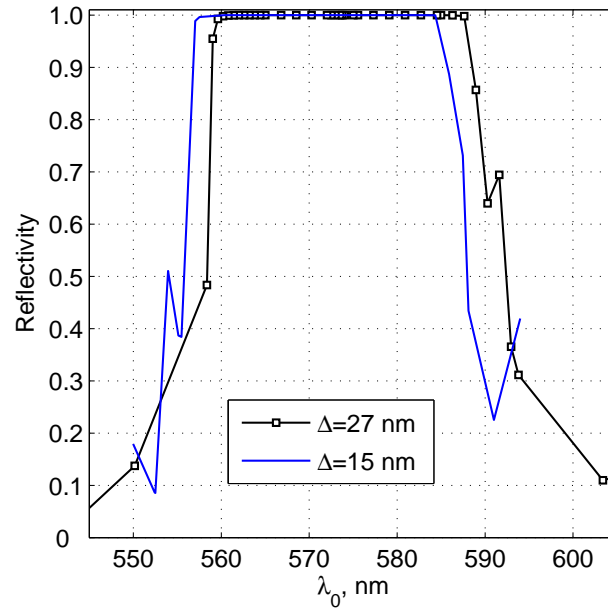


Figure A.1: Band gap ( $\Gamma$ - $L$  direction) of bare silica opal photonic crystal ( $\langle 111 \rangle$  orientation,  $d_{111}=216$  nm, 32 periods, 96 sphere planes) as a function of mesh spacings  $\Delta$  used in transfer-matrix method numerical simulation. Coating thickness: 4.7 nm.

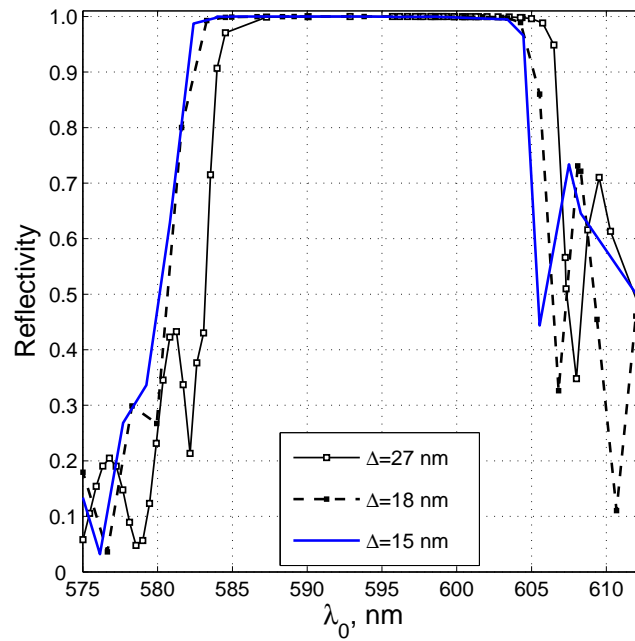


Figure A.2: Band gap ( $\Gamma$ - $L$  direction) of alumina-coated silica opal photonic crystal as a function of mesh spacings  $\Delta$  used in transfer-matrix method numerical simulation. Coating thickness: 4.7 nm. Photonic crystal geometry described in Fig. A.1.

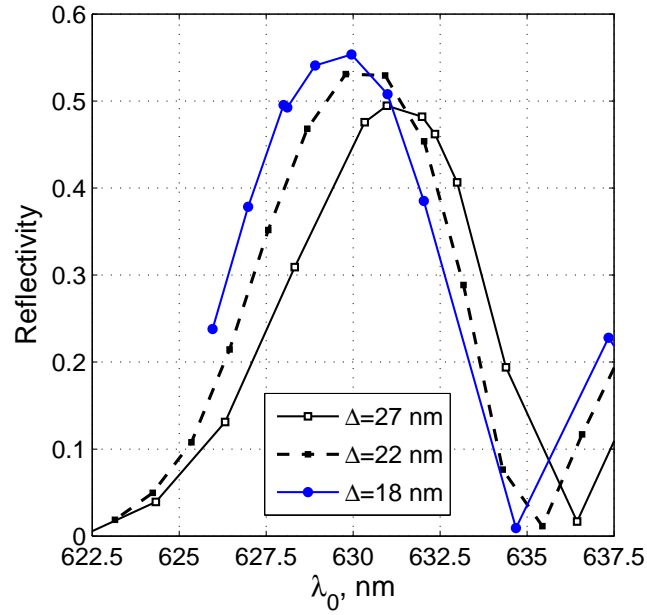


Figure A.3: Reflectance spectrum of alumina-coated silica opal photonic crystal as a function of mesh spacings  $\Delta$  used in transfer-matrix method numerical simulation. Coating thickness: 16.1 nm. Photonic crystal geometry described in Fig. A.1.

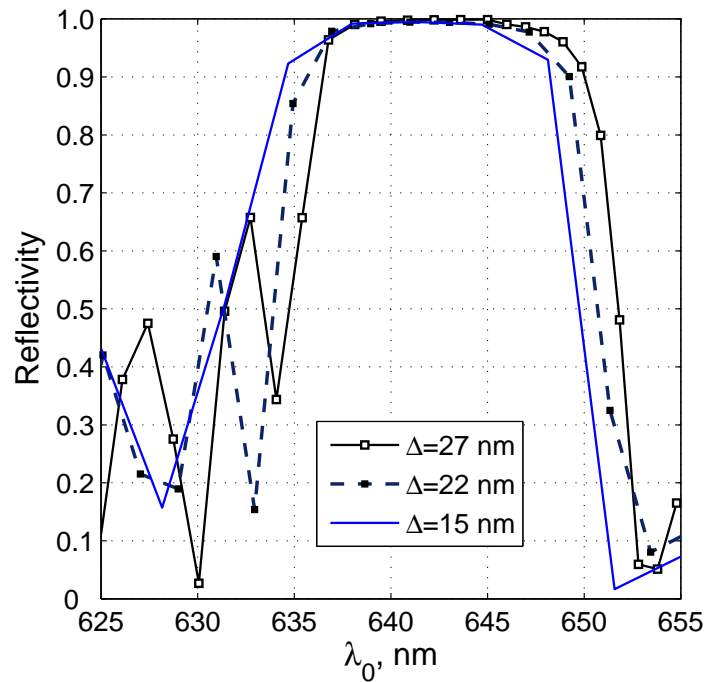


Figure A.4: Band gap ( $\Gamma$ - $L$  direction) of alumina-coated silica opal photonic crystal ( $d_{111} = 216$  nm, 32 periods, 96 sphere planes) as a function of mesh spacings  $\Delta$  used in transfer-matrix method numerical simulation. Coating thickness: 33.3 nm. Photonic crystal geometry described in Fig. A.2.

## Appendix B

### Convergence of transfer-matrix method predictions of metal-coated opal cutoff frequencies

Figure B.1 shows how the cutoff frequency converges as a function of sampling density. Simulations of the  $2r=350$  nm opal has smallest mesh spacings  $\Delta$  compared to the  $t_c = 25$ -nm thick tungsten film (albeit  $\Delta > \frac{t_c}{2}$ ), its predictions of  $\lambda_c$  are closest to the true converged value. Because these values do not appear to converge, the larger opals cannot be considered to be doing so, either. The absence of a converging trend precludes estimating an upper limit for the cutoff frequency. Hence, for each size opal, the maximum values of the normalized cutoff frequency  $\frac{a}{\lambda_c}$  in Fig B.1 serve as lower bounds.

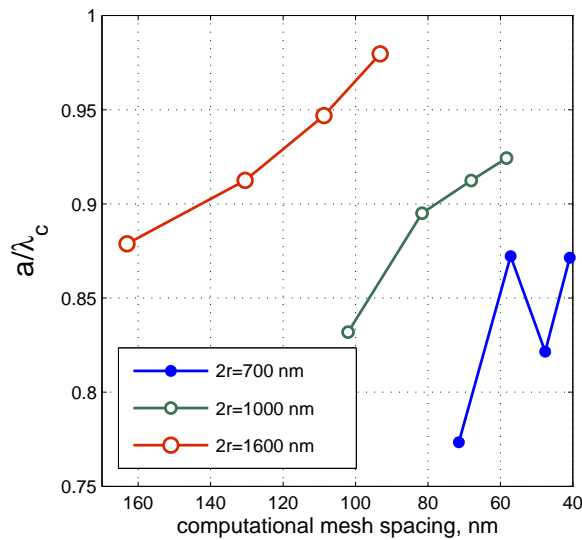


Figure B.1: Convergence of numerically calculated cutoff wavelength (3 dB) for opal photonic crystals as a function of mesh spacing in the unit cell.